




Chair of Materials Science and Testing of Polymers

Master's Thesis



Experimental and Numerical Investigation
of Mechanical Metamaterials Produced by
Selective Laser Sintering

Philipp Arno Franz Huber, BSc

September 2023



EIDESSTÄTLICHE ERKLÄRUNG

Ich erkläre an Eides statt, dass ich diese Arbeit selbständig verfasst, andere als die angegebenen Quellen und Hilfsmittel nicht benutzt, und mich auch sonst keiner unerlaubten Hilfsmittel bedient habe.

Ich erkläre, dass ich die Richtlinien des Senats der Montanuniversität Leoben zu "Gute wissenschaftliche Praxis" gelesen, verstanden und befolgt habe.

Weiters erkläre ich, dass die elektronische und gedruckte Version der eingereichten wissenschaftlichen Abschlussarbeit formal und inhaltlich identisch sind.

Datum 21.09.2023

Unterschrift Verfasser/in
Philipp Arno Franz Huber

ACKNOWLEDGEMENT

I want to thank the Montanuniversitaet Leoben, especially Univ.-Prof. Dr. mont. Gerald Pinter, for giving me the opportunity to write my master's thesis in the field of mechanical testing and simulations of polymers.

Beside the University, I have done my research at the Polymer Competence Center Leoben GmbH (PCCL) which was mainly responsible for the funding and support during my studies. Within this project, I was supervised by Mathias Fleisch, M.Sc. and Andreas Thalhammer, M.Sc.. I also want to address a great thank to the boss of the working group "Engineering Polymers" at the PCCL, Dr. mont. Michael Berer. Additionally, I have to thank my other colleagues in the working group. Striking out Gerald Maier and Bernd Haar which were an indispensable support during material testing.

The mechanical testing was done in the labs of the Chair of Materials Science and Testing of Polymers at the Montanuniversitaet Leoben. Therefore, I also want to thank Jürgen Grosser, Jürgen Föttinger who supported me during testing in the labs of the university.

This study was supported of the "Österreichische Forschungsförderungsgesellschaft" by funding this research within the CHEMITECTURE project.

Thanks to Peyton Michelle Foti form New Orleans (USA) who supported me as a native speaker while writing and correcting my master's thesis.

I also need to thank my parents and my grandmother who supported me throughout my studies at the university.

To my beloved Stefanie, who supported me emotionally through my long studies. I would not have been able to finish my studies without her!

ABSTRACT

Mechanical metamaterials captivate through the possibility to achieve mechanical properties which are not commonly found in nature. Variable stiffness mechanical metamaterials are a group of metamaterials which allows the designer to create structures with uniquely tuned stiffness behavior in all three spatial directions by changing the geometric parameters of its unit cell.

This study investigates the effect of tensile and three-point-bending based material modeling for finite element simulations of variable stiffness mechanical metamaterial structures. Furthermore, elastic-plastic material models were used to increase the simulation quality. Based on specimens produced by Selective Laser Sintering, different materials were investigated in this study: Polyamide 12, Polypropylene and TIGITAL® 3D-Set TPP. Dynamic mechanical analysis, Charpy impact tests, tensile and three-point-bending tests were performed with standard specimens. The variable stiffness structures were investigated by means of compression tests. Based on the tensile test and three-point-bending test data, a yield stress – plastic strain approach and Johnson-Cook strain hardening model was set up respectively. Additionally, the standard tests were performed based on horizontal and vertical printed specimens. The tunability of the compressive modulus of the variable stiffness structure was evaluated using three different structures with different geometric parameters. The temperature dependence was determined by testing the materials and structures at -30 °C, 0 °C and 23 °C.

The possibility of changing the compressive modulus by changing the geometric parameters of the metamaterial structures was shown by the investigation. Beyond that the simulation quality was significantly improved by using elastic-plastic when compared to pure linear elastic material models. Furthermore, it is shown that three-point-bending based material models based on test data of vertical printed specimens led to the best results.

KURZFASSUNG

Mechanische Metamaterialien besitzen Eigenschaften, welche in der Natur nicht üblich sind. Eine Gruppe der mechanischen Metamaterialien sind jene mit variabler Steifigkeit. Sie ermöglichen es Strukturen mit verschiedenen Steifigkeiten in alle drei Raumrichtungen zu erzeugen. Dies wird dadurch erzielt, dass die geometrischen Parameter der Einheitszellen individuell angepasst werden können.

Diese Studie untersucht den Einfluss von unterschiedlichen Materialmodellierungsansätzen auf die Qualität von Finite-Elemente-Simulationen von mechanischen Metamaterialstrukturen mit variabler Steifigkeit. Hierfür werden elastisch-plastische Materialmodelle auf Basis von Zug- und Drei-Punkt-Biege-Versuchen verwendet. Auf der Grundlage von Zug-Versuchen kommt ein Ansatz mittels Fließspannung – plastische Dehnung zur Anwendung. Um auf Basis von Drei-Punkt-Biege-Versuchen elastisch-plastische Materialmodelle zu generieren, wurde ein „Reverse-Engineering“ Ansatz unter Anwendung des Johnson-Cook Modell gewählt. Die untersuchten Prüfkörper wurden aus Polyamid 12, Polypropylen und TIGITAL® 3D-Set TPP mittels selektiven Lasersintern hergestellt. Mit diesen wurden dynamische mechanische Analysen, Charpy-Schlagversuche, Zug- und Dreipunkt-Biegeversuche durchgeführt. Um den Einfluss von unterschiedlichen Geometrieparametern auf die Drucksteifigkeit von mechanischen Metamaterialstrukturen zu untersuchen, wurden drei verschiedene Strukturen mit unterschiedlichen Dimensionen der Einheitszellen untersucht. Die Strukturen selbst wurden mittels Druckversuche geprüft. Zusätzlich wurden die Standardversuche an horizontal und vertikal gedruckten Prüfkörpern durchgeführt. Die Temperaturabhängigkeit wurde durch Prüfung der Materialien und Strukturen bei -30 °C, 0 °C und 23 °C ermittelt.

Die Untersuchung zeigte, dass die Drucksteifigkeit durch Änderung der geometrischen Parameter der Metamaterialstrukturen variiert werden kann. Des Weiteren konnte gezeigt werden, dass die Simulationsqualität durch die Verwendung elastisch-plastischer Modelle im Vergleich zu rein linear-elastischen Materialmodellen deutlich verbessert wurde. Darüber hinaus zeigt die Studie, dass durch auf vertikal gedruckten, Dreipunkt-Biegung basierenden Materialmodellen, die größte Übereinstimmung zwischen realen Druckversuchen und Simulation erreicht werden könnte.

TABLE OF CONTENT

ABBREVIATIONS	1
SYMBOLS	2
FIGURES	5
TABLES	12
1 INTRODUCTION	14
2 BACKGROUND	16
2.1 Mechanical metamaterials	16
2.2 Additive manufacturing	18
2.3 Mechanical testing	21
2.3.1 Impact testing.....	21
2.3.2 Quasi-static mechanical testing.....	23
2.3.2.1 Tensile testing.....	26
2.3.2.2 Three-point-bending testing	30
2.3.2.3 Compression testing.....	33
2.3.3 Dynamic Mechanical Analysis	34
2.4 FEM Simulations	37
2.4.1 Material modeling	39
2.4.1.1 Calculation of yield stress – plastic strain	42
2.4.1.2 Johnson-Cook strain hardening model.....	45
2.4.2 Element types	46
3 EXPERIMENTAL APPROACH	49
3.1 Materials.....	51
3.1.1 Specimen geometries	51
3.1.2 Variable Stiffness structures.....	53
3.1.2.1 Unit Cell of VS-structure	53
3.1.2.2 Full-size VS-structures	55
3.2 Specimen and sample preparation.....	58

Table of content

3.2.1	Drying of PA12	59
3.2.2	Unwarping of PP specimens	62
3.2.2.1	Differential Scanning Calorimetry	63
3.2.2.2	Milling	65
3.2.3	Unwarping of TPP	66
3.2.4	Unpacking TPP VS-structures	67
3.3	Dynamic Mechanic Analysis	68
3.4	Impact tests	69
3.5	Tensile tests	70
3.6	Three-point-bending tests	72
3.7	Compression tests	74
3.8	Finite Element simulations	76
3.8.1	Material modeling	76
3.8.1.1	Tensile based material modeling.....	77
3.8.1.2	3PB based material modeling.....	78
3.8.2	Compression simulations	80
3.8.3	Mesh test simulations	81
4	RESULTS AND DISCUSSION	84
4.1	Polyamide 12	84
4.1.1	DMA results	84
4.1.2	Mechanical testing	85
4.1.2.1	Charpy impact tests.....	85
4.1.2.2	Tensile tests	86
4.1.2.3	3PB tests	91
4.1.2.4	VS-structure compression tests.....	95
4.1.3	Material modeling	98
4.1.3.1	Tensile based yield stress – plastic strain model.....	98
4.1.3.2	3PB tests-based Johnson-Cook optimization	102
4.1.4	VS-structure simulations and comparison	105
4.2	Polypropylene.....	110
4.2.1	DMA results	110

Table of content

4.2.2	Mechanical testing	110
4.2.2.1	Charpy impact tests	111
4.2.2.2	Tensile tests	112
4.2.2.3	3PB tests	116
4.2.2.4	VS-structure compression tests.....	120
4.2.3	Material modeling	124
4.2.3.1	Tensile based yield stress – plastic strain model.....	124
4.2.3.2	3PB tests-based Johnson-Cook optimization	128
4.2.4	VS-structure simulations and comparison	131
5	SUMMARY, CONCLUSION AND OUTLOOK.....	134
6	LITERATURE	139
7	APPENDIX	145
7.1	Yield stress – plastic strain data PA12	145
7.2	Yield stress – plastic strain data PP	147

ABBREVIATIONS

1D	One-dimensional	Stdev	Standard deviation
2.5D	Two-and-a-half-dimensional	UC	Unit cell
2D	Two-dimensional	VS	Variable Stiffness
3D	Three-dimensional		
3PB	Three-point-bending		
4PB	Four-point-bending		
AM	Additive manufacturing		
CAD	Computer-aided design		
comp	Compressive		
Creo	Creo Parametric 2.0		
DIC	Digital Image Correlation		
DMA	Dynamic Mechanic Analysis		
DOF	Degree of freedom		
DSC	Differential Scanning Calorimetry		
Eq.	Equation		
FEA	Finite-Element-Analysis		
FEM	Finite-Element-Method		
JC	Johnson-Cook		
No.	Number		
PA 12	Polyamide 12		
PP	Polypropylene		
SLS	Selective laser sintering		

SYMBOLS

Symbol	Description	Unit		
L_{span}	Anvil span distance	mm	$\varepsilon_{eng,l,t}$	Engineering strain; longitudinal, transversal %
s	Bending deflection	mm	σ_{eng}	Engineering stress MPa
F_{3PB}	Bending force	N	E_{3PB}	Flexural modulus MPa
$M_b(x)$	Bending moment	Nm	F	Force (general) N
ε_{3PB}	Bending strain	%	$E_{c,loss}$	Friction loss energy J
σ_{3PB}	Bending stress	MPa	P	General mechanical parameter -
E^*	Complex modulus	MPa	I	Geometrical moment of inertia mm ⁴
F_{comp}	Compressive force	N	T_g	Glass transition temperature °C
E_{comp}	Compressive modulus	MPa	$L_{0,comp}$	Height of the compression specimen mm
E_c	Corrected impact energy	J	b_0	Initial thickness of reference volume mm
\hat{A}	Cross section (general)	mm ²	a_0	Initial width of reference volume mm
$A_{0,comp}$	Cross-section compression specimen	mm ²	A_0	Initial cross section of reference volume mm ²
A	Deformed cross section of reference volume	mm ²	S	Internal state of polymers -
$\varepsilon_{elastic}$	Elastic strain	%	A (JC)	Johnson-Cook parameter A MPa
$\Delta L_{0,comp}$	Elongation during compression test	mm		
ΔL_0	Elongation during tensile test	mm		
$f''(x)$	Elastic bend line	-		

B (JC)	Johnson-Cook parameter B	MPa	I_y	Smallest axial inertia moment	mm ⁴
C (JC)	Johnson-Cook parameter B	-	i	Smallest radius of inertia	mm
m	Johnson-Cook parameter m	-	G	Specimen geometry	-
n	Johnson-Cook parameter n	-	h	Specimen thickness	mm
E''	Loss modulus	MPa	b	Specimen width	mm
M	Material properties	-	L_0	Starting test length	mm
$E_{c,meas}$	Measured impact energy	J	E'	Storage modulus	MPa
ε_{comp}	Nominal compressive strain	%	ε_A	Strain amplitude	%
$\hat{\theta}$	Nondimensional temperature	-	$\dot{\varepsilon}_{plastic}$	Strain rate	%/s
δ	Phase shift	-	σ	Stress (general)	MPa
$\varepsilon_{plastic}$	Plastic strain	%	σ_A	Stress amplitude	MPa
ν_{true}	Poisson's ratio	-	F_{tens}	Tensile force	N
$\nu_{true,zx}$	Poisson's ratio in x-z plane	-	T	Test conditions	-
$\nu_{true,zy}$	Poisson's ratio in y-z plane	-	h_{struc}	Thickness of the VS-structure	mm
$\dot{\varepsilon}_0$	Reference strain rate	%/s	ε_{total}	Total strain	%
λ	Slenderness ratio	-	$\varepsilon_{ture,l,t}$	True strain; longitudinal, transversal	%
			σ_{true}	True stress	MPa
			E_{true}	True Young's modulus	MPa
			a_{cU}	Valid flexural modulus	kJ/mm ²
			$E_{3PB,valid}$	Valid flexural modulus	MPa

ν_{valid}	Valid Poisson's ratio	-
<hr/>		
$E_{tens,valid}$	Valid Young's modulus	MPa
<hr/>		
b_{struc}	Width of the VS- structure	mm
<hr/>		
σ_{yield}	Yield stress	MPa
<hr/>		
$E_{eng} = E$	Young's modulus	MPa
<hr/>		

FIGURES

Figure 2.1:	Classification of mechanical metamaterial types with examples for different design approaches; taken from Yu et al. [3].	17
Figure 2.2:	Examples for unit cells based on a) beams, b) plates and c) minimum surface topology; taken from Lu et al. [8].....	18
Figure 2.3:	Classification of AM processes based on the type of feedstock and transition; taken from Godec [9].	19
Figure 2.4:	Main parts and machine layout of a typical SLS machine; taken from Kruth et al. [20].	21
Figure 2.5:	a) Charpy impact test setup; taken from Grellmann and Seidler [22] and b) edgewise and flatwise specimen orientation; taken from EN ISO 179-1:2010 [23] and translated.	22
Figure 2.6:	Polymer deformation phases in tensile tests; taken from Grellmann and Seidler [22].	25
Figure 2.7:	Young's modulus of Polystyrene (PS), Polyvinyl chloride (PVC), high impact Polystyrene (PS-HI), high density Polyethylene (PE-HD), low density Polyethylene (PE-LD) depending on a) time and b) temperature; taken from Grellmann and Seidler [22].	26
Figure 2.8:	a) Detailed view of tensile stress – strain curve and b) transversal – longitudinal strain curve; taken from Grellmann and Seidler [22].	28
Figure 2.9:	Tensile stress – strain curves of a) brittle polymers, b) and c) tough materials with yield point, d) tough polymers without yield point and e) polymers with high elasticity; taken from Grellmann and Seidler [22].....	29
Figure 2.10:	Tensile stress – strain curves of ductile polymers for a) increasing test speed and b) decreasing temperature; taken from Grellmann and Seidler [22].	29
Figure 2.11:	Bending setup with bending moment and force distribution for a) three-point-bending and b) four-point-bending test; taken from Grellmann and Seidler [22]. ..	30

Figure 2.12: a) 3PB specimen, b) bending stress and strain and c) shear stress distribution; taken from Grellmann and Seidler [22]..... 32

Figure 2.13: Simplified and true stress distribution in 3PB specimen; taken from Heine [32] and translated. 32

Figure 2.14: Dynamic stress – strain response of an elastic (left) and linear-viscoelastic material (right); taken from Ehrenstein [28] and translated. 35

Figure 2.15: Schematic of the complex modulus with the loss modulus, storage modulus and phase angle; taken from Grellmann and Seidler [22]..... 35

Figure 2.16: Characteristic DMA results for semicrystalline thermoplastic polymers; taken from Ehrenstein [28] and translated..... 37

Figure 2.17: Steps of FEM; taken from Steinke [34] and translated. 38

Figure 2.18: Input parameters for a possible test program to investigate material data; taken from Bergstrom [38]..... 40

Figure 2.19: Stress – strain curve with elastic and plastic strain regions and strain hardening; taken from Korte [37] and translated. 41

Figure 2.20: Converting a stress – strain curve to gather an elastic-plastic material model; taken from Korte [37] and translated. 42

Figure 2.21: Reference volume under uniaxial loading for a) unloaded and b) loaded state. 43

Figure 2.22: Frequently used elements in Abaqus; taken from ABAQUS Inc. [45]. 47

Figure 2.23: Three-dimensional continuum elements with Abaqus element label for a) linear hexahedral, b) quadratic hexahedral and c) modified second-order tetrahedral element; taken from ABAQUS Inc. [45]..... 47

Figure 2.24: Element labeling scheme of Abaqus; taken from ABAQUS Inc. [46]. 48

Figure 3.1: Flow chart of the experimental approach..... 50

Figure 3.2: Dimensions of a) tensile-, b) 3PB- and Charpy-, c) DMA specimens..... 52

Figure 3.3:	Horizontal and vertical print orientation in the SLS build volume. The build direction is along the z-axis.	53
Figure 3.4:	Geometric parameters of the VS-structure unit cell; taken from Fleisch et al. [7].	54
Figure 3.5:	Dimensions of VS-structures with detailed main differential unit cell parameter for a) VS-structure A, b) VS-structure B and c) VS-structure C. The assumed build direction is along the z-axis.	57
Figure 3.6:	3D printed VS-Structures. a) PP-VS-structure A, B) PP-VS-structure B and c) PP-VS-structure C.....	58
Figure 3.7:	a) Racked-up PA12 specimens and b) PA12-VS-structures in the vacuum dryer.	59
Figure 3.8:	a) Mean relative weight loss while drying and b) total relative weight loss after drying.	61
Figure 3.9:	Warped specimens after delivery of a PP.	62
Figure 3.10:	Temperature profile of the DSC measurements.	64
Figure 3.11:	DSC result of an untreated PP sample.....	64
Figure 3.12:	Positions of the characteristic peaks measured by DSC.....	65
Figure 3.13:	a) PP-VS-structure B and b) milling setup for machining the top and bottom faces.	66
Figure 3.14:	Warped specimens after delivery of a TPP.	66
Figure 3.15:	Air blow chamber to unpack the TPP-VS-structure from residual powder. a) Overview and b) detailed top view.	67
Figure 3.16:	TPP-VS-structures after unpacking from the residual powder.	68
Figure 3.17:	12 N DMA “DMA/SDTA861 ^{er} ” from Mettler Toledo, USA.....	69
Figure 3.18:	Charpy impact test setup.	70
Figure 3.19:	a) Universal testing machine with DIC system and b) detailed view of the mechanical clamps with specimen and spray pattern.	72

Figure 3.20: 3PB setup while testing. 74

Figure 3.21: a) Compression test setup and b) detailed view of the VS-structure before testing with reference spray pattern on the compression plates..... 75

Figure 3.22: 3PB-reverse engineering approach for material optimization..... 78

Figure 3.23: Simulation model for 3PB simulations (meshed parts)..... 80

Figure 3.24: VS-structure in Abaqus with partitioned struts. a) 3D view, b) x-y view and c) z-y view (green = global mesh settings, grey = finer mesh for the struts). 81

Figure 3.25: Mesh test simulation results with different seed sizes for PA12-VS-structure B with tensile based material models in horizontal and vertical direction at 23 °C. 83

Figure 4.1: Storage module and loss factor of PA12. 84

Figure 4.2: Mean Charpy impact strength and standard deviation of 10 specimens for each orientation and temperature of PA12. 86

Figure 4.3: Tensile stress – strain curves of PA12 for a) horizontal at 23 °C, b) vertical at 23 °C, c) horizontal at 0 °C, d) vertical at 0 °C, e) horizontal at -30 °C and f) vertical at -30 °C. 88

Figure 4.4: PA12 tensile test results. a) Mean tensile strength and b) mean strain at break. 89

Figure 4.5: PA12 tensile test results. a) Mean Young’s modulus and b) mean Poisson’s ratio. 90

Figure 4.6: Bending stress – strain curves of PA12 for a) horizontal at 23 °C, b) vertical at 23 °C, c) horizontal at 0 °C, d) vertical at 0 °C, e) horizontal at -30 °C and f) vertical at -30 °C. 92

Figure 4.7: PA12 bending test results. a) Mean flexural strength and b) mean strain at break. 93

Figure 4.8: Mean flexural modulus of PA12 for horizontal and vertical oriented specimens. 94

Figure 4.9: PA12 compressive stress – strain curves for all five repetitions for a) VS-structure A at 23 °C, b) VS-structure B at 23 °C, c) VS-structure B at 0 °C, d) VS-structure B at -30 °C and e) VS-structure C at 23 °C. 95

Figure 4.10: PA12 compression test results. a) Mean compressive strength and b) mean compressive strain at break. 97

Figure 4.11: Mean compressive modulus for PA12-VS-structures. 98

Figure 4.12: PA12 mean tensile stress – strain for a) horizontal and b) vertical print direction. 100

Figure 4.13: PA12 yield stress – plastic strain for a) horizontal and b) vertical print direction. 101

Figure 4.14: PA12 mean bending force – deflection of a) horizontal and b) vertical print direction. 103

Figure 4.15: Comparison of measured and optimized bending force – deflection curves for PA12 with a) horizontal and b) vertical print direction. 104

Figure 4.16: Optimization history of PA12-horizontal-23 °C. a) Parameter *A*, b) parameter *B* and c) parameter *n*. 105

Figure 4.17: Compressive stress – strain of the VS-structures of PA12 with mean test data and simulation results for tensile and 3PB based material model in horizontal and vertical print direction. a) Structure A at 23 °C, b) structure B at 23 °C, c) structure B at 0 °C, d) structure B at -30 °C and e) structure C at 23 °C. 106

Figure 4.18: Comparison of the simulated compressive modulus for PA12 with horizontal and vertical print direction using tensile and 3PB based material models and the real compression test data for a) VS-structure A, b) VS-structure B and c) VS-structure C. 109

Figure 4.19: Storage module and loss factor of PP. 110

Figure 4.20: Mean Charpy impact strength of 10 specimens each orientation and temperature of PP. 111

Figure 4.21: Tensile stress – strain curves of PP for a) horizontal at 23 °C, b) vertical at 23 °C, c) horizontal at 0 °C, d) vertical at 0 °C, e) horizontal at -30 °C and f) vertical at -30 °C. 112

Figure 4.22: PP tensile test results. a) Mean tensile strength and b) mean strain at break. 114

Figure 4.23: PP tensile test results. a) Mean Young’s modulus and b) mean Poisson’s ratio. 115

Figure 4.24: Bending stress – strain curves of PP for a) horizontal at 23 °C, b) vertical at 23 °C, c) horizontal at 0 °C, d) vertical at 0 °C, e) horizontal at -30 °C and f) vertical at -30 °C. 117

Figure 4.25: PP bending test results. a) Mean flexural strength and b) mean strain at break. 119

Figure 4.26: Mean flexural modulus of PP for horizontal and vertical oriented specimens. 120

Figure 4.27: PP compressive stress – strain curves for all five repetitions for a) VS-structure A at 23 °C, b) VS-structure B at 23 °C, c) VS-structure B at 0 °C, d) VS-structure B at -30 °C and e) VS-structure C at 23 °C. 121

Figure 4.28: PP compression test results. a) Mean compressive strength, b) mean compressive strain at break. 123

Figure 4.29: Mean compressive modulus for PP-VS-structures..... 124

Figure 4.30: PP mean tensile stress – strain for a) horizontal and b) vertical print direction. 126

Figure 4.31: PP yield stress – plastic strain for a) horizontal and b) vertical print direction. 127

Figure 4.32: PP mean bending force – deflection of a) horizontal and b) vertical print direction. 129

Figure 4.33: Comparison of measured and optimized bending force – deflection curves for PP with a) horizontal and b) vertical print direction..... 130

Figure 4.34: Compressive stress – strain of the VS-structures of PP with mean test data and simulation results for tensile and 3PB based material model in horizontal and vertical print direction. a) Structure A at 23 °C, b) structure B at 23 °C, c) structure B at 0 °C, d) structure B at -30 °C and e) structure C at 23 °C..... 132

Figure 4.35: Comparison of the simulated compressive modulus for PP with horizontal and vertical print direction using tensile and 3PB based material models and the real compression test data for a) VS-structure A, b) VS-structure B and c) VS-structure C..... 133

TABLES

Table 3.1: Description of the geometric parameters of the VS-structure unit cells; taken from Fleisch et al. [7].	54
Table 3.2: Description of the geometric parameters of the unit cells investigated in this study.	55
Table 3.3: Goal values for the geometric parameters of the VS-structure A to C, referring to Figure 3.4 with simplifications as described in Table 3.2.	56
Table 3.4: Mean values of real PA12-VS-structure geometry parameters.	58
Table 3.5: Mean values of real PP-VS-structure geometry parameters.	58
Table 3.6: Pretest parameters for the annealing of PP.	62
Table 3.7: DSC test parameters.	63
Table 3.8: DMA test parameters.	69
Table 3.9: Test settings of the tensile measurements.	72
Table 3.10: Test settings of the 3PB measurements.	73
Table 3.11: Test parameters for the compression tests.	76
Table 3.12: Generated material models for each material.	77
Table 3.13: Element parameters for the struts in the VS-structure for the mesh test simulations.	82
Table 3.14: Abaqus element type reference descriptions [58].	82
Table 4.1: Mean tensile test results for PA12.	91
Table 4.2: Mean 3PB test results for PA12.	94
Table 4.3: Mean compression test results for PA12-VS-structures.	96
Table 4.4: PA12 input data for elastic material models, based on tensile tests, in Abaqus.	99

Table 4.5: PA12 input data for elastic-plastic material models, based on 3PB tests, in Abaqus.	102
Table 4.6: Mean values and standard deviations of the moduli for the comparison of the error simulations.	107
Table 4.7: Mean tensile test results for PP.	116
Table 4.8: Mean 3PB test results for PP.	118
Table 4.9: Mean compression test results for PP-VS-structures.	122
Table 4.10: PP input data for elastic material models, based on tensile tests, in Abaqus.	125
Table 4.11: PP input data for elastic-plastic material models, based on 3PB tests, in Abaqus.	128
Table 7.1: Tensile based yield stress – plastic strain data for PA12 with horizontal print orientation.	145
Table 7.2: Tensile based yield stress – plastic strain data for PA12 with vertical print orientation.	146
Table 7.3: Tensile based yield stress – plastic strain data for PP with horizontal print orientation.	147
Table 7.4: Tensile based yield stress – plastic strain data for PP with vertical print orientation.	148

1 INTRODUCTION

Metamaterials are uniquely designed structures with the ability to react to external stimuli in a way that is usually not found in naturally occurring materials [1, 2]. Among other different types of metamaterials, mechanical metamaterials are a group of structures with the ability to utilize tunable mechanical properties like Young's modulus, shear/bulk modulus and Poisson's ratio by varying geometric parameters [3]. The design of those structures is based on unit cells. A unit cell is the smallest structural unit which forms the desired geometry by assembling them in all three spatial directions [3]. Within this group of mechanical metamaterials unique properties include, but are not limited to, zero or negative Poisson's ratio [2, 4], lightweight structures [5], twist and shear deformation structures [6] and variable stiffness structures [7]. With the increasing availability of additive manufacturing processes, the development of metamaterials increased in the last years [3, 8 - 10]. A commonly used tool for developers are finite element simulations. Those simulations help designers to investigate the reaction of metamaterials to applied loads within a short period of time. This can either be done on unit cells or full-scale geometries [7].

Fleisch et al. [7] developed a variable stiffness mechanical metamaterial with a tunable lattice compression modulus by varying the geometric parameters of the unit cell in all three directions independently. The initial study was based on structures produced via Fused Filament Fabrication and Digital Light Processing.

Advancing from the research of Fleisch et al. [7], this study investigates the properties of mechanical metamaterials produced by Selective Laser Sintering. For this, standard specimens and structures produced by Selective Laser Sintering using Polyamide 12, Polypropylene and TIGITAL® 3D-Set TPP were investigated. In addition to full-scale compression tests, finite element simulations of the tested structures were performed to quantify the applicability of simulations during the design phase. To increase the simulation quality, elastic-plastic material models were generated based on both tensile and three-point-bending tests of standard specimens. For the tensile based material modeling, the yield stress – plastic strain data was calculated for the plastic part for the material model. The material models based on three-point-bending tests were generated using the

Johnson-Cook strain hardening model. Both material models were created with horizontally and vertically manufactured specimens to study the influence of the printing direction. To determine the tunability of the compressive modulus three structures with different geometric parameters were analyzed. Finally, the temperature dependency of the materials at -30 °C, 0 °C and 23 °C is discussed. For a deeper discussion of the temperature dependency additionally dynamic mechanical analysis were performed. Beyond that Charpy impact tests were done.

2 BACKGROUND

Based on the theme of this study, a brief discussion of mechanical metamaterials, additive manufacturing, mechanical testing of polymers and finite element simulations with material modeling and element types is given in the following sections.

2.1 Mechanical metamaterials

The term metamaterial (“meta” is Greek for beyond) was originally used for artificial materials that had the ability to manipulate waves in electromagnetics and photonics [1, 8]. Metamaterials are structures designed to achieve properties which are usually not found in nature [1, 2]. Nowadays, different kinds of metamaterials exist. Depending on their field of application they can be categorized as optical [11], acoustic [12], electromagnetic [13], thermal [14] or mechanical metamaterials [3, 10, 15].

Mechanical metamaterials are a group of metamaterials which provide unique mechanical properties based on the design of their geometric structure [3]. These unique properties include, but are not limited to, zero or negative Poisson’s ratio [2, 4], lightweight structures [5], twist and shear deformation structures [6] and variable stiffness structures [7]. Figure 2.1 shows a general classification of mechanical metamaterials according to the mechanical parameter of interest (Young’s modulus, shear/bulk modulus and Poisson’s ratio) with example structures [3].

Mechanical metamaterials are usually built from unit cells. A unit cell is the smallest structural unit which is assembled to form the geometry of interest [3]. Unit cells for mechanical metamaterials can be classified in beam-based, plate-based and unit cells with minimum surface topologies [8]. Figure 2.2 shows some examples of possible unit cell geometries [8]. Beam-based mechanical metamaterials are the most widely used type. They consist of rods which are connected at shared nodal points. Plate-based metamaterials consists of thin plates which are connected at their edges to each other. Minimum surface topologies are structures designed of thin, double curved, continuous, and smooth shells. In contrast to beam- and plate-based metamaterials, minimum topology structures do not share nodal points or edges [8].

In this study, a plate-based mechanical metamaterial with tunable compressive modulus was investigated. For this, a variable stiffness (VS) structure developed by Fleisch et al. [7] was used. A detailed description of the unit cell geometry and the full-size structure is given in section 3.1.2.

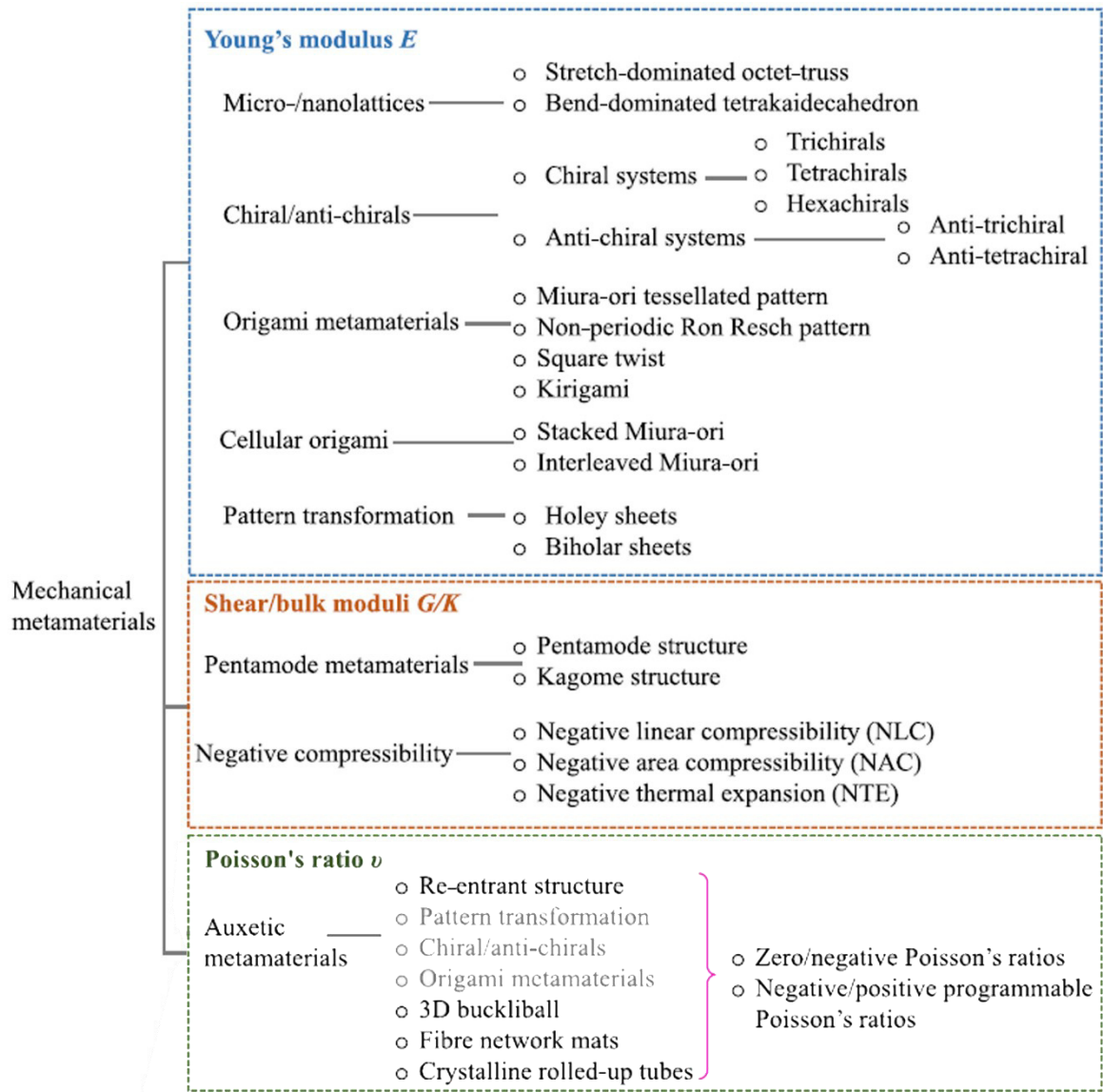


Figure 2.1: Classification of mechanical metamaterial types with examples for different design approaches; taken from Yu et al. [3].

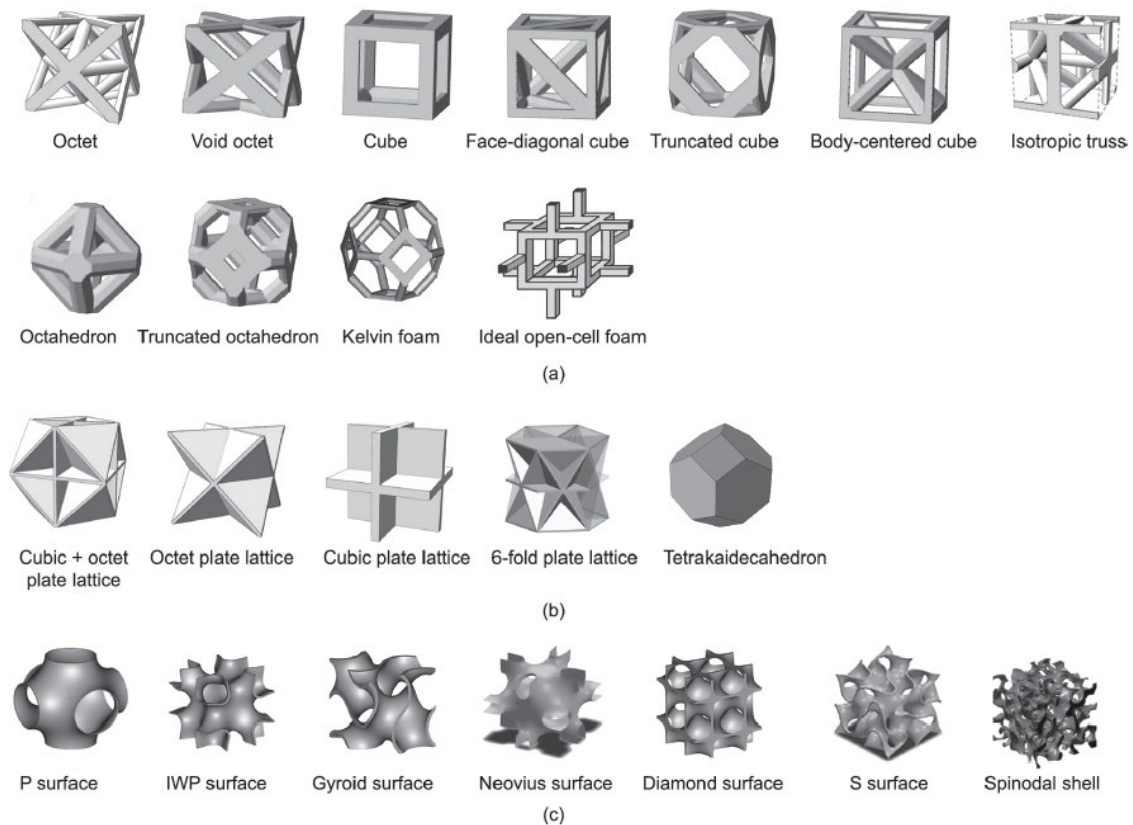


Figure 2.2: Examples for unit cells based on a) beams, b) plates and c) minimum surface topology; taken from Lu et al. [8].

2.2 Additive manufacturing

Additive manufacturing (AM) is defined as a manufacturing process that produces parts automatically by piling or joining together volume elements primarily in layers [16, 17]. Based on the build concept by individual layers, additive manufacturing is characterized by unique technical parameters and advantages:

- production directly using 3D computer aided design (CAD) data,
- no requirement of geometry specific tools,
- material properties of parts are established during production due to solidification or curing of the built materials,
- beside support structures required by the AM processes, parts can be produced in all direction without the necessity of external clamping devices,
- all modern available additive manufacturing machines can handle the same file type (.stl-files) [16].

Additive manufacturing processes can be classified by the physical state of the feedstock (liquid, solid and powder based raw materials [9]). Figure 2.3 shows the classification of AM processes by the state of feedstock and transition state (e.g., melting, binding, or polymerization).

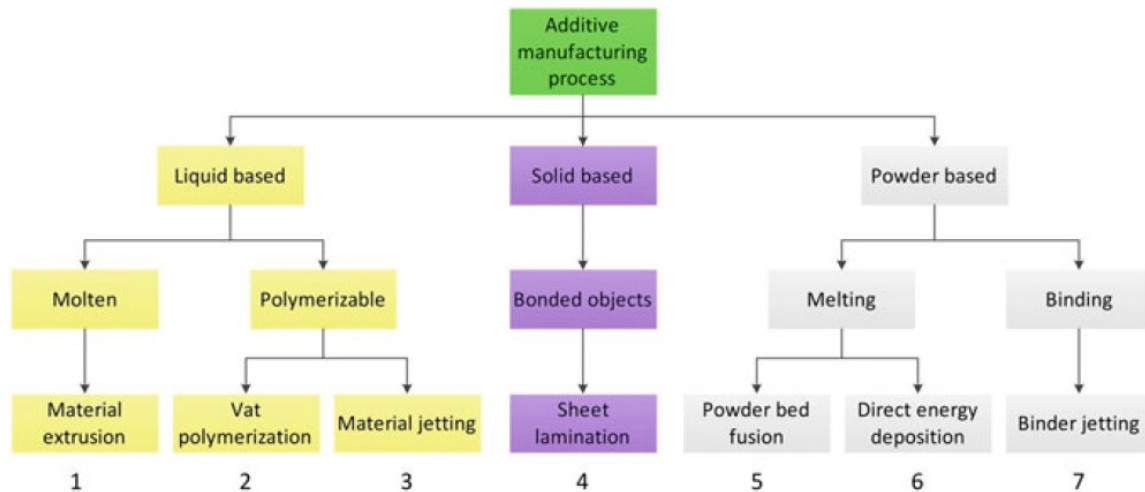


Figure 2.3: Classification of AM processes based on the type of feedstock and transition; taken from Godec [9].

The main processes shown in Figure 2.3 are [9]:

1. Material extrusion: Material is dispensed through a nozzle selectively, e.g., Fused Filament Fabrication or Fused Deposition modeling.
2. Vat (photo-) polymerization: A liquid photopolymer is cured by a reactive photo initiator, e.g., Stereolithography, Digital Light Processing or Continuous Liquid Interface Production.
3. Material jetting: Part production by selectively deposition of droplets of the build materials, e.g., PolyJet, Drop On Demand or NanoParticle Jetting.
4. Sheet lamination: Sheets of build material are cut and then bonded to each other to create a finished part, e.g., Laminated Object Manufacturing or Selective Laminate Composite Object Manufacturing.
5. Powder bed fusion: Section of a polymer powder bed are fused together by thermal energy, e.g., Selective Laser Sintering (SLS), Selective Laser Melting, Electron Beam Melting or Mulit Jet Fusion.

6. Directed energy deposition: An AM process which produces parts of materials that are deposited in molten form by using a focused thermal energy source (e.g., laser, electron beam or plasma arc) for melting and deposition, e.g., Laser Engineered Net Shaping, Aerosol Jet, or Laser Deposition Welding.
7. Binder jetting: Sections of a powder bed are bonded together by using a liquid bonding agent, e.g., 3D Printing or ColourJet Printing.

Within this study, specimens and mechanical metamaterial structures produced by Selective Laser Sintering (SLS) were investigated. Therefore, only this additive manufacturing process will be discussed in more detail.

Selective Laser Sintering was developed and patented by Deckard in the mid-1980s [18]. Since then, SLS developed into a widely used additive manufacturing technology [19]. During the part production, a condensed powder bed is solidified selectively by means of thermal energy [19]. The surface of the powder grains (typically 20-50 μm up to maximum 100 μm grain size) are slightly molten and afterwards cooled down to achieve a solid layer [19].

Figure 2.4 shows the principle setup of a SLS machine. For each layer the powder is first fed out of the feed container and placed in front of the roll [9]. The roller then moves the powder on top of the build cylinder. During the movement of the roll, the powder is compressed. Finally, the laser sinters the powder bed at the desired areas. For the next layer the build cylinder is moved downwards and the processes starts again [9]. The build area is typically filled with nitrogen and heated to 170 $^{\circ}\text{C}$ - 210 $^{\circ}\text{C}$ [19]. Due to the high temperatures, a uniform cooling is key for advanced part qualities.

After the initial sintering step, post-production steps are required to get the final parts [19]. First, the residual powder needs to be removed to separate the parts from the powder bed [19]. After removing the powder, typically a surface treatment such as sand blasting or sanding is done to increase the part quality [9, 19]. Additional steps like special heat treatments or machining with cutting tools can be performed afterwards [9, 16, 19].

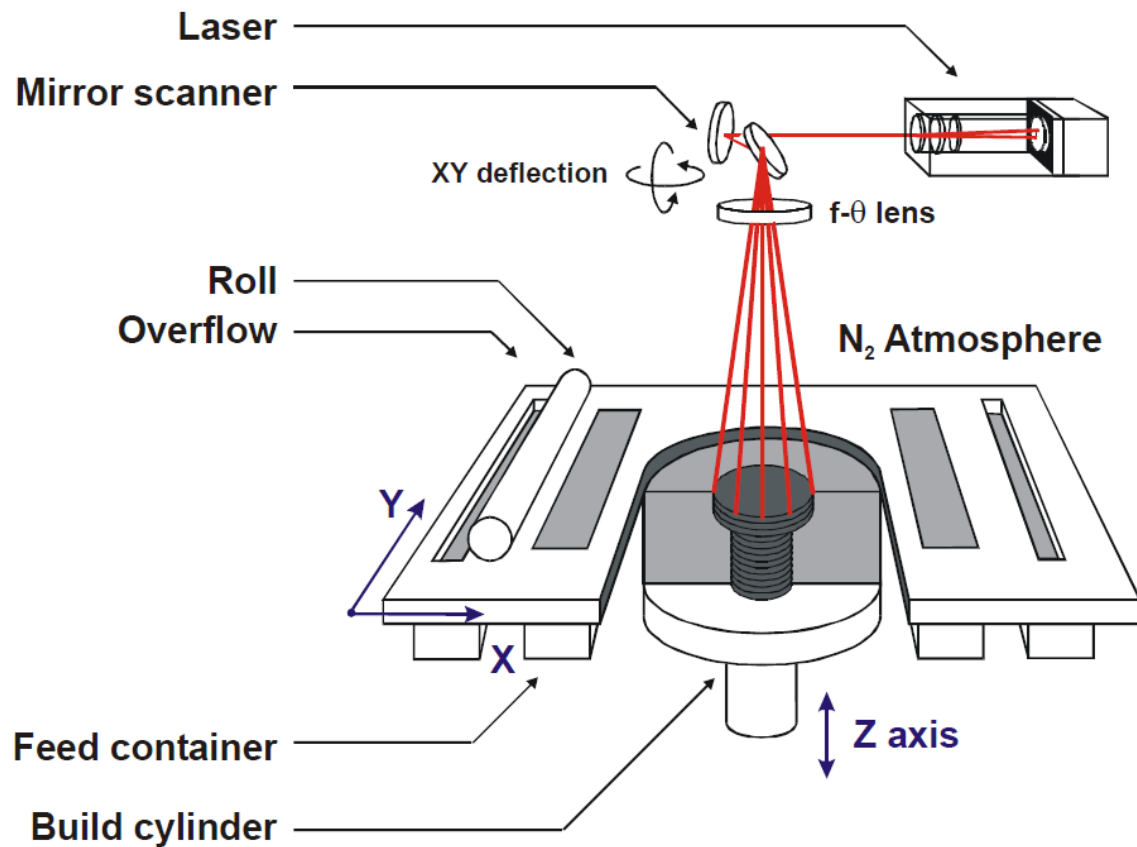


Figure 2.4: Main parts and machine layout of a typical SLS machine; taken from Kruth et al. [20].

2.3 Mechanical testing

The properties of solid polymers are essential for the purposeful usage of the final parts [21]. Compared to, for example steel, polymers offer a completely different material behavior which in addition can easily be varied by the production step as well [21]. This fact results in the necessity of a variety of different test methods like impact tests, quasi-static tests, dynamic or fatigue testing [21, 22]. For this study, impact tests, quasi-static tests (tensile, three-point-bending and compression) and dynamic mechanical analysis were performed and will be described in the following sections.

2.3.1 Impact testing

In applications, impact loads are occurring frequently. For example during demolding, traffic accidents or laying underground pipes [22]. During an impact, the strain rate increases drastically, resulting in a significant change of the mechanical response, especially

for the strength and break behavior [22]. The most utilized test to characterize the impact behavior of polymers is the Charpy-impact test. The test is standardized within the EN ISO 179-1:2010 [23]. The test setup is shown in Figure 2.5 a). The impact results in a multiaxial stress state within the specimen [22]. The tests can either be performed with notched or unnotched specimens in flatwise or edgewise orientation of the specimen with respect to the test rig (see Figure 2.5 b)) [23]. For this study, unnotched specimens flatwise orientation were tested.

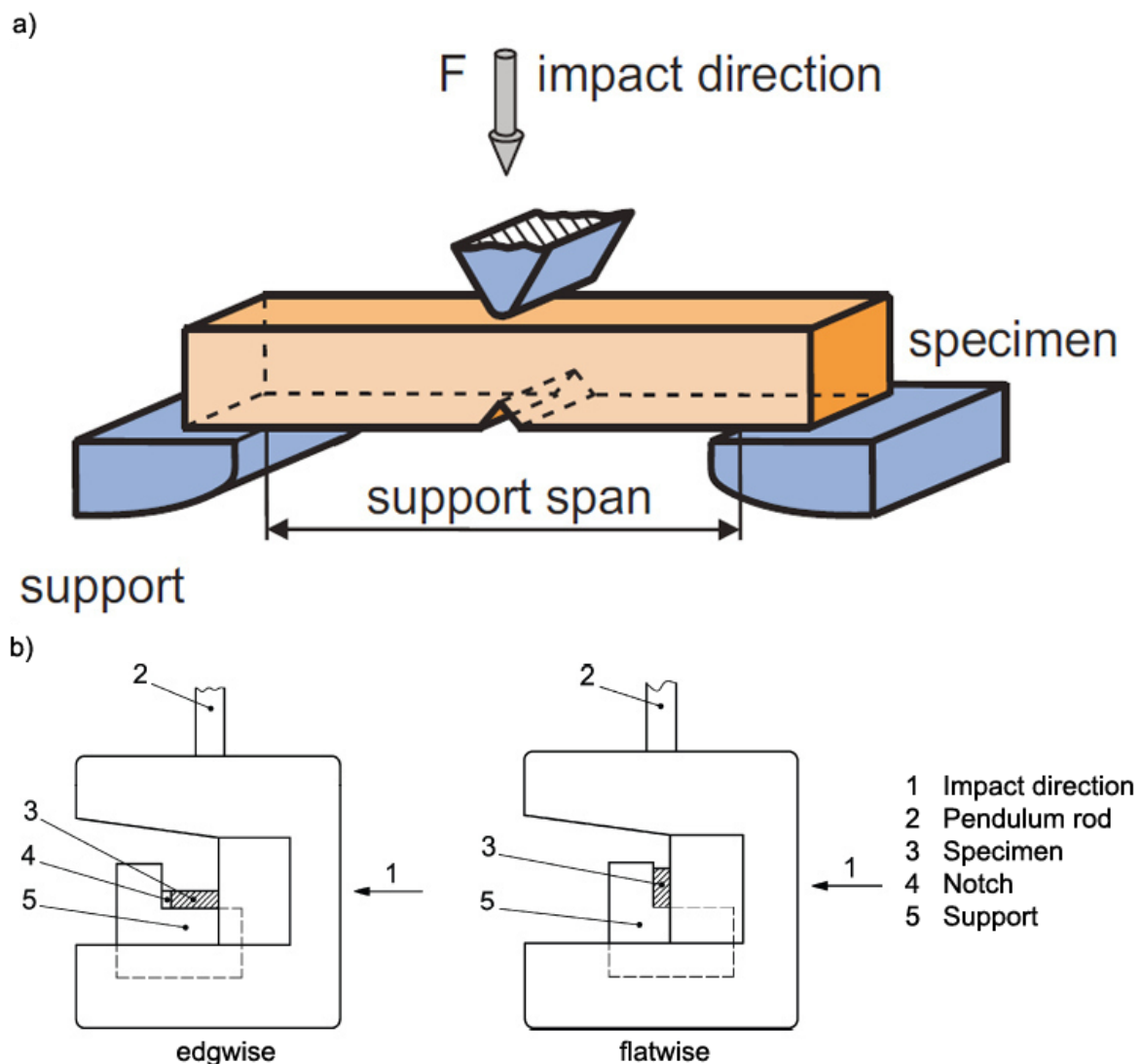


Figure 2.5: a) Charpy impact test setup; taken from Grellmann and Seidler [22] and b) edgewise and flatwise specimen orientation; taken from EN ISO 179-1:2010 [23] and translated.

The measurements were performed and evaluated according to EN ISO 179-1:2010 [23]. First, the friction loss energy, $E_{c,loss}$, was measured by releasing the pendulum three times

without a specimen to calculate the mean friction loss energy, $E_{c,loss}$. To obtain the corrected impact energy, E_c in J, the loss energy was subtracted from the measured impact energy $E_{c,meas}$ in J according to Eq. 2.1.

$$E_c = E_{c,meas} - E_{c,loss} \quad (2.1)$$

The unnotched Charpy impact strength a_{cU} in kJ/mm² was then calculated according to Eq. 2.2

$$a_{cU} = \frac{E_c}{h \cdot b} \cdot 10^3 \quad (2.2)$$

using the thickness h and the width b of the specimen in mm.

2.3.2 Quasi-static mechanical testing

Quasi-static tests are widely used methods to characterize materials. They are conducted within a strain rate range of approximately 10^{-5} to 10^{-1} s^{-1} until break or a predetermined load is reached. Beyond that, the load is applied slowly, impact-free and continuously increasing [22]. Quasi-static substitute characteristic values are widely used for dimensioning polymer parts [24]. Dimensioning parameters, determined by quasi-static tests include, but are not limited to:

- stiffness parameters (e.g. Young's modulus, flexural modulus, compressive modulus),
- Poisson's ratio,
- allowable stresses and strains [24].

The parameters strongly depend on the load situation and must be considered accordingly for an application [24]. Commonly utilized test methods are tensile, three-point-bending (3PB) and compression tests [22, 24]. In addition, those tests are performed to investigate characteristic material parameters for quality control, failure analysis and to perform pre-selections of polymers [25]. Depending on the loading time and the application temperature, quasi-static tests are performed to investigate the different deformation regimes of polymers:

- elastic deformation,
- linear-viscoelastic deformation,
- non-linear viscoelastic deformation and
- plastic deformation [22].

Especially for non-reinforced polymers, elastic deformation can only be observed in a very small strain region [22]. The elastic deformation is characterized by a reversible strain and is described by Hook's law [22, 26]. Hook's law becomes obvious when an applied load results in an straight line of a reversible strain [26]. For polymers, this straight line is defined by the secant modulus [27]. In contrast to metals, the mechanical response of polymers is time dependent [22]. Due to characteristic relaxation times, defined by the viscous behavior of polymers, a viscoelastic material behavior must be considered [22]. Additionally, the load level plays a role in the mechanical response of a polymer material. Therefore, a distinction between linear-viscoelastic and non-linear viscoelastic deformation must be considered. The plastic deformation is characterized by an irreversible deformation due to external loading [24]. Figure 2.6 highlights the different phases a polymeric material can undergo in a tensile test [22]. Figure 2.6 a) shows a stress strain curve of an unfilled polymer divided in the main deformation regions. Figure 2.6 b) shows the strain rate and defect density in the tensile specimen while testing.

The deformation characteristics of a polymer show a strong dependence of internal and external parameters for any mechanical test. Eq. 2.3 shows the different dependencies for each mechanical test result P [22].

$$P = f(M, S, G, T) \quad (2.3)$$

M denotes the state and properties of the tested material, such as chemical structure, molecular weight and its distribution, fillers etc.. S labels the internal state of polymers such as the crystallinity, residual stresses, orientation etc.. The specimen geometry G includes the shape, dimensions, notches as well as structural defects such as weld lines, voids, cavities, and agglomerations. Finally, T defines the test methods and strategies, such as tensile or 3PB tests, the test temperature, testing speed and environmental influences such as moisture or ultra violet radiation [22].

Figure 2.7 illustrated the influence of time and temperature for different polymers under tensile loading, highlighting the complexity of the behavior of different materials [22]. The figure shows the decrease of mechanical properties with prolonged time and increased temperature.

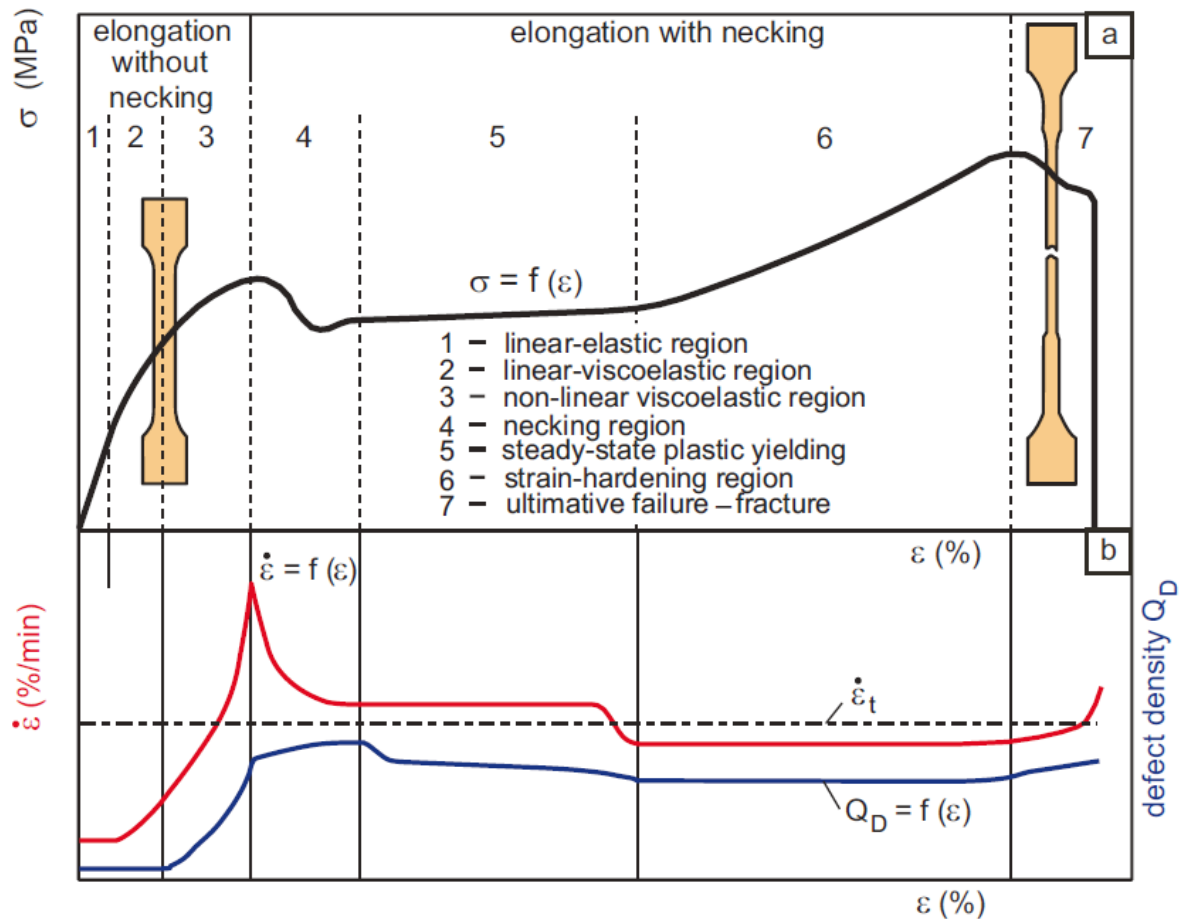


Figure 2.6: Polymer deformation phases in tensile tests; taken from Grellmann and Seidler [22].

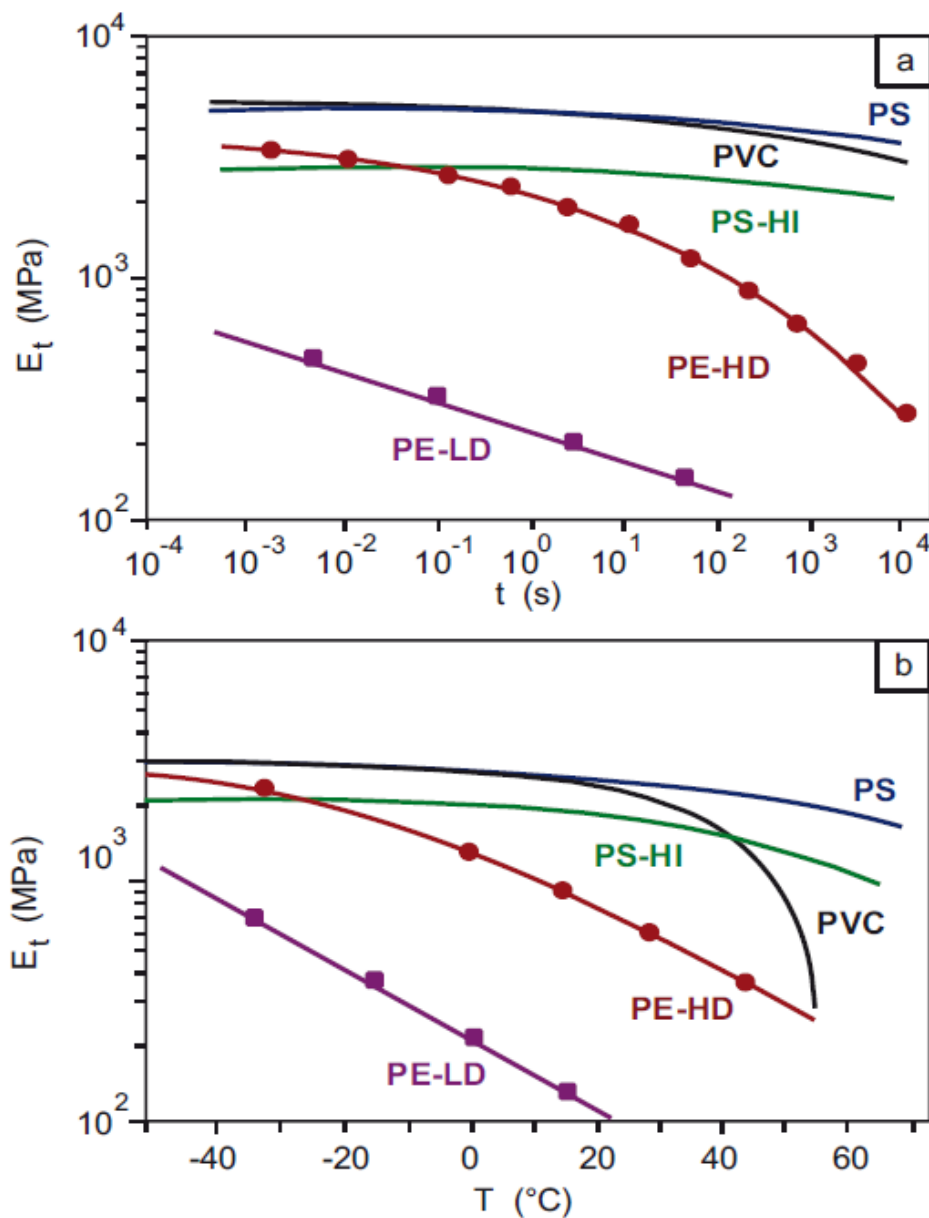


Figure 2.7: Young's modulus of Polystyrene (PS), Polyvinyl chloride (PVC), high impact Polystyrene (PS-HI), high density Polyethylene (PE-HD), low density Polyethylene (PE-LD) depending on a) time and b) temperature; taken from Grellmann and Seidler [22].

2.3.2.1 Tensile testing

Tensile tests are considered as the fundamental mechanical testing method for quasi-static testing [22]. Although pure tensile loads are relatively rare in modern parts, tensile tests have a unique standing in science because of their uniaxial stress applied during testing [22, 28]. The evaluation of a tensile test is standardized within the EN ISO 527-2:1996 [27]. The engineering tensile strain $\varepsilon_{eng,l,t}$ in longitudinal and transversal direction is calculated using

the starting test length L_0 in mm and the elongation during measurement ΔL_0 in mm according to Eq. 2.4.

$$\varepsilon_{eng,t} = \frac{\Delta L_0}{L_0} \cdot 100 \% \quad (2.4)$$

The engineering stress σ_{eng} is calculated using Eq. 2.5

$$\sigma_{eng} = \frac{F_{tens}}{h \cdot b} \quad (2.5)$$

Where, F_{tens} in N, is the measured tensile force and b and h are the width and thickness of the specimen in mm, respectively. In contrast to metals, polymers show no pronounced linearity in the elastic region [22, 29]. The non-linearity is depicted in Figure 2.8. Figure 2.8 a) and b) show exemplarily a stress – strain and transversal – longitudinal curve for a ductile polymer, respectively. The Young's modulus, E_{eng} in MPa, is defined as the gradient of the stress – strain curve between 0.05 % – 0.25 % of tensile strain [22, 27, 29] (see Eq. 2.6).

$$E_{eng} = E = \left. \frac{\Delta \sigma_{eng}}{\Delta \varepsilon_{eng}} \right|_{\varepsilon_{eng}=0.05 \%}^{\varepsilon_{eng}=0.25 \%} \quad (2.6)$$

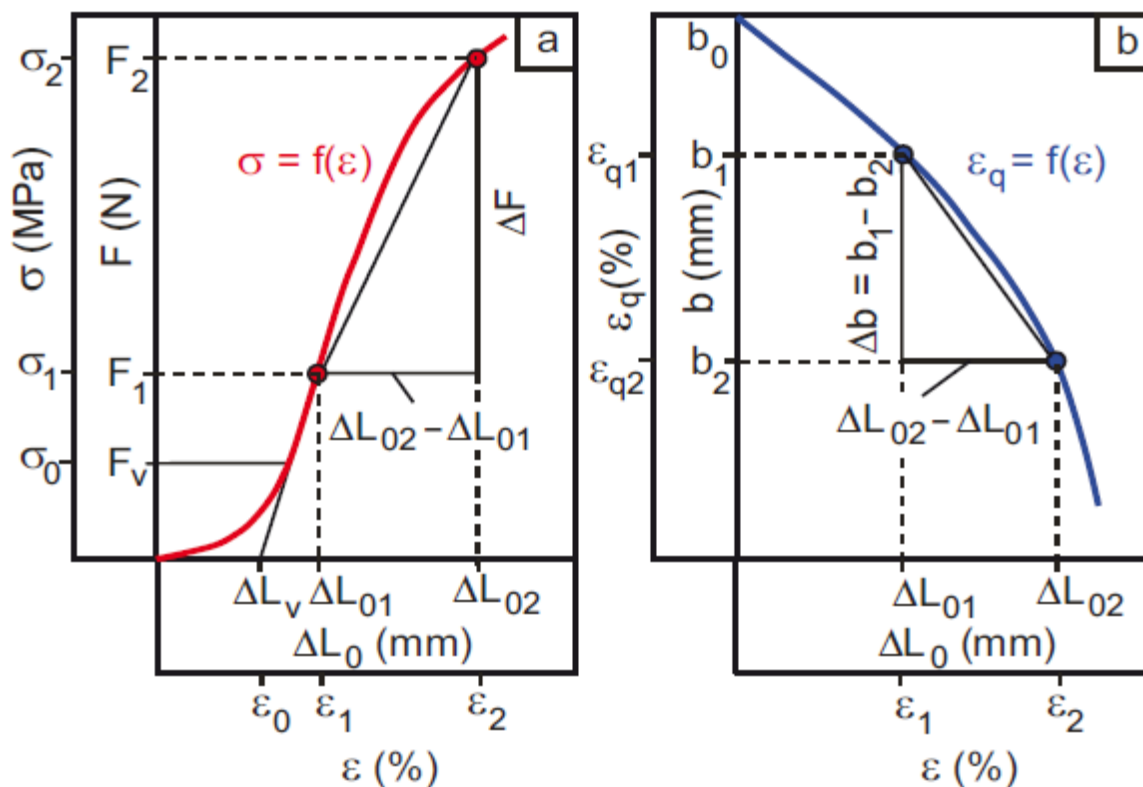


Figure 2.8: a) Detailed view of tensile stress – strain curve and b) transversal – longitudinal strain curve; taken from Grellmann and Seidler [22].

Figure 2.9 summarizes the stress – strain behavior of different polymer types under tensile loading [22]. The figure shows the typical appearance of polymers under mechanical loading. Brittle polymers are characterized by their high tensile strength and low strain at break, ductile polymers have a lower tensile strength but higher strain at break values, even necking can be observed and elastomers show a small tensile strength but a very high strain at break [22, 26].

Additionally, the behavior of polymers can be influenced by the test conditions [22]. By increasing the test speed or decreasing the temperature, the tensile strength increases and the strain at break decreases for ductile polymers [22, 24, 26, 30]. This behavior is depicted in Figure 2.10.

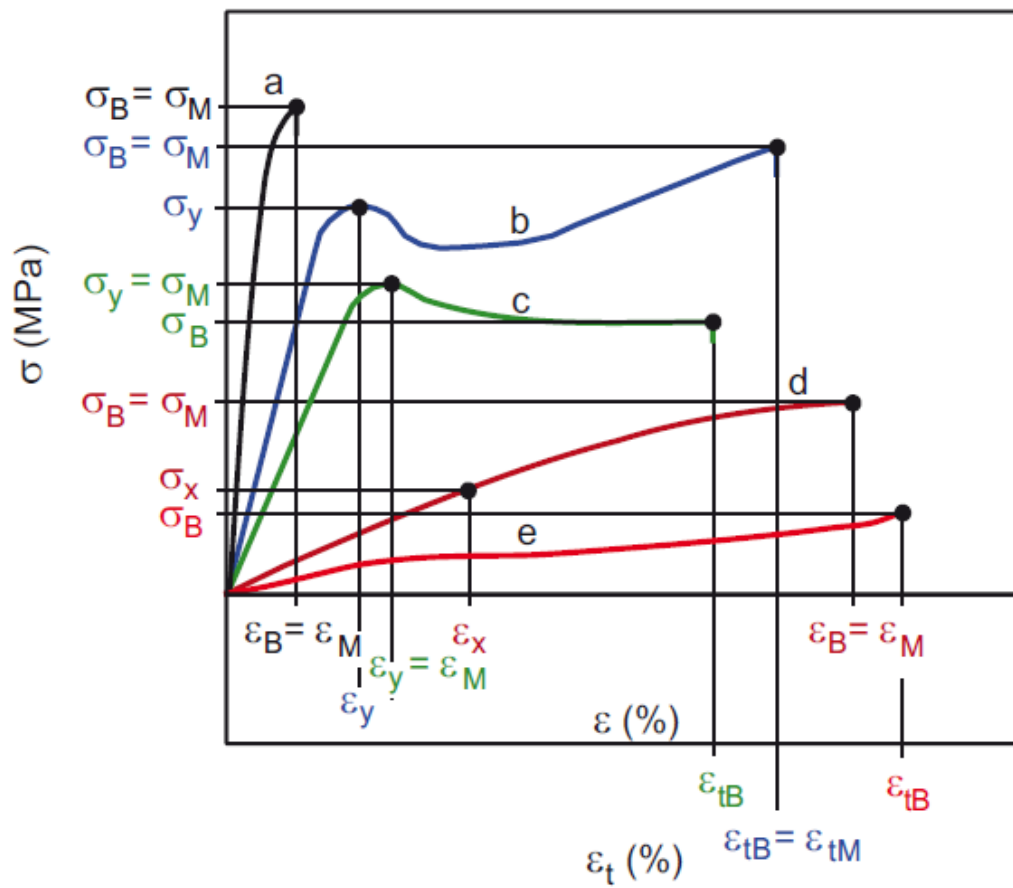


Figure 2.9: Tensile stress – strain curves of a) brittle polymers, b) and c) tough materials with yield point, d) tough polymers without yield point and e) polymers with high elasticity; taken from Grellmann and Seidler [22].

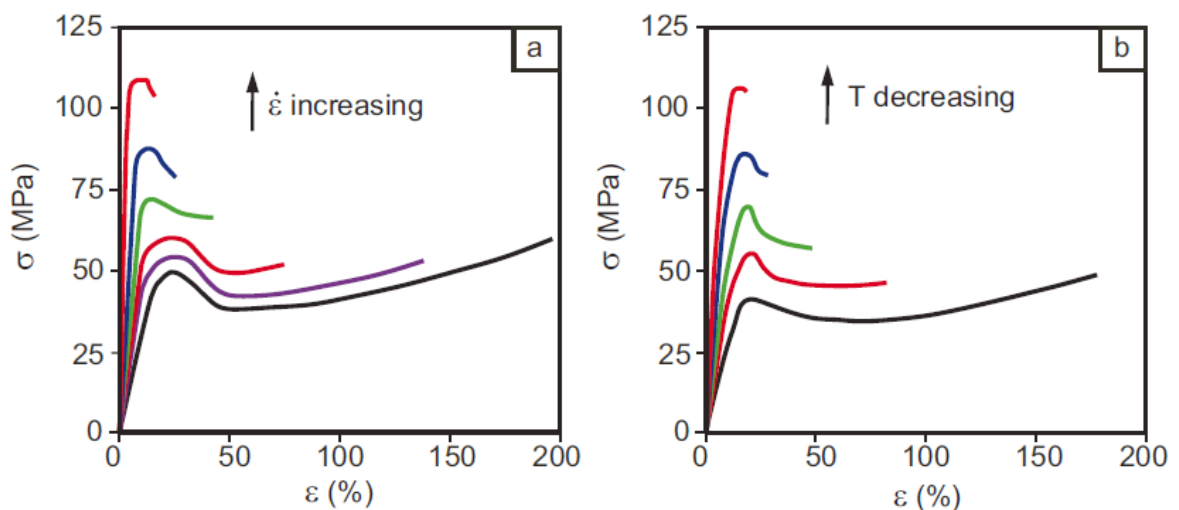


Figure 2.10: Tensile stress – strain curves of ductile polymers for a) increasing test speed and b) decreasing temperature; taken from Grellmann and Seidler [22].

2.3.2.2 Three-point-bending testing

Bending loads are very common loads in engineering parts, resulting in the necessity of special tests to characterize materials with three-point- (3PB) or four-point-bending (4PB) [22]. The two setups are shown in Figure 2.11. Besides testing close to application loads, quasi-static bending tests are used for brittle polymers which could cause problems during tensile testing [22]. Similar to the tensile tests (see section 2.3.2) the load rate, temperature and time dependence must be considered before testing [22].

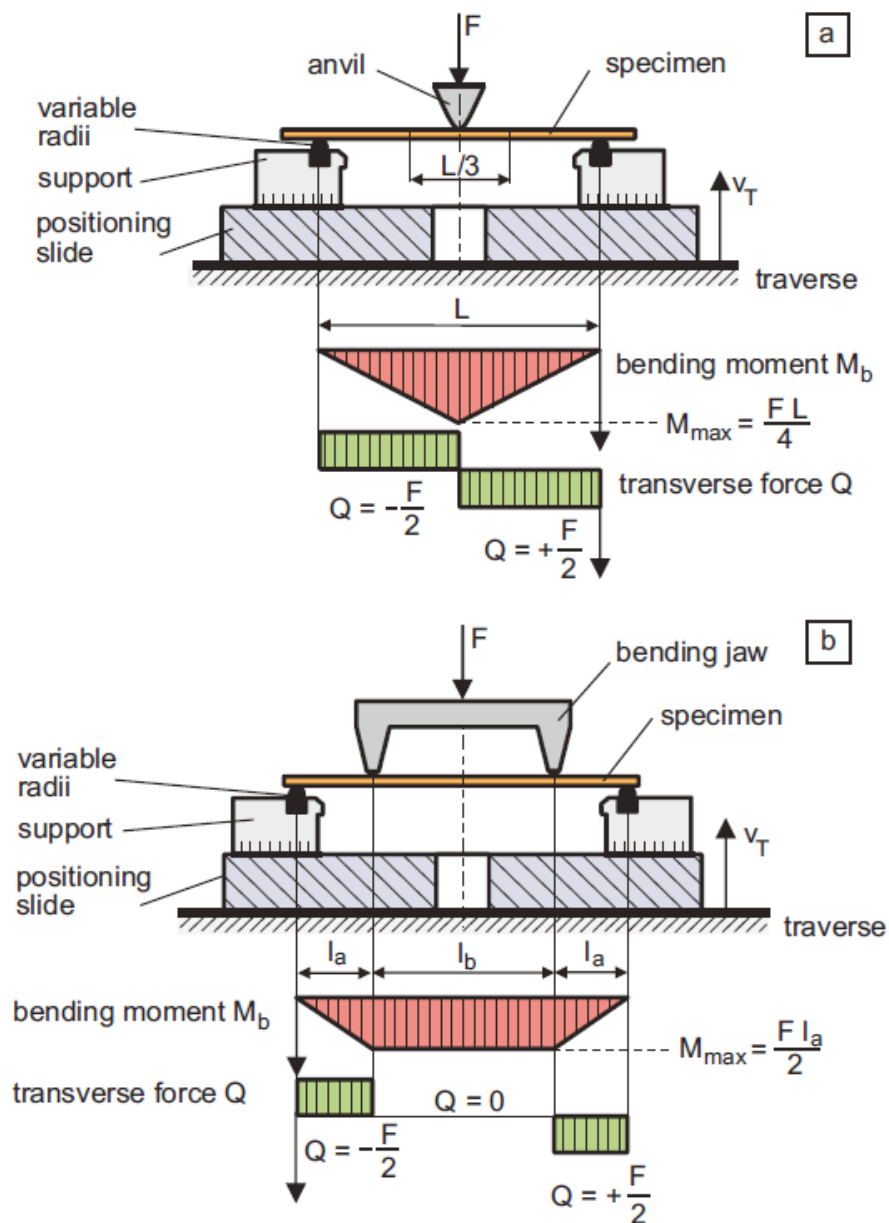


Figure 2.11: Bending setup with bending moment and force distribution for a) three-point-bending and b) four-point-bending test; taken from Grellmann and Seidler [22].

3PB has an increasing bending moment until half the span distance of the support anvil. Contrary, 4PB has a constant bending load within the span distance of the bending jaws [22]. In this study only 3PB was used. Therefore, only this type of bending tests will be covered in more detail.

Eq. 2.7 shows the equation of the elastic bend line for small deflections $f''(x)$ with the bending moment $M_b(x)$, the Young's modulus E and the geometrical moment of inertia I [22].

$$f''(x) = -\frac{M_b(x)}{E \cdot I} \quad (2.7)$$

Solving this differential equation, Eq. 2.8 shows the deflection $f(x)$ with the bending force F_{3PB} and the span distance L_{span} [22].

$$f(x) = \frac{1}{E \cdot I} \cdot \left(\frac{F_{3PB}}{16} \cdot L_{span}^2 \cdot x - \frac{F_{3PB}}{12} \cdot x^3 \right) \quad (2.8)$$

Solving this equation for rectangular specimens, the bending strain ε_{3PB} can be calculated using the specimen thickness h in mm, the measured deflection s in mm and the anvil span L_{span} in mm (see Eq. 2.9) [31].

$$\varepsilon_{3PB} = \frac{600 \cdot s \cdot h}{L_{span}^2} \quad (2.9)$$

The bending stress σ_{3PB} in MPa is calculated using Eq. 2.10

$$\sigma_{3PB} = \frac{3 \cdot F_{3PB} \cdot L_{span}}{2 \cdot b \cdot h^2} \quad (2.10)$$

where F_{3PB} in N, is the measured bending force and b is the width of the specimen [31]. The flexural modulus, E_{3PB} in MPa, was calculated according to standard in the strain range of 0.05 % – 0.25 % using the bending stress σ_{3PB} and strain ε_{3PB} (see Eq. 2.11) [31].

$$E_{3PB} = \frac{\Delta \sigma_{3PB}}{\Delta \varepsilon_{3PB}} \Bigg|_{\varepsilon_{3PB}=0.05\%}^{\varepsilon_{3PB}=0.25\%} \quad (2.11)$$

Figure 2.12 shows the normal bending stress, strain and shear stress distribution for pure elastic deformation [22]. It becomes obvious that the normal stress shows a linear stress

distribution across the thickness of the specimen. Resulting in an linear strain distribution while applying Hook's law [22].

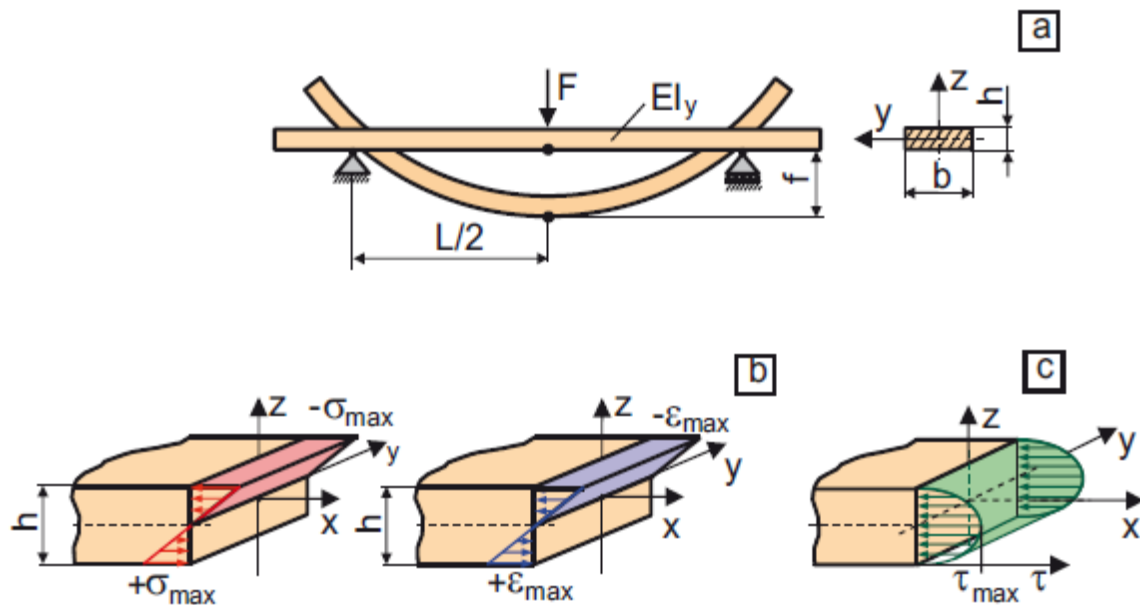


Figure 2.12: a) 3PB specimen, b) bending stress and strain and c) shear stress distribution; taken from Grellmann and Seidler [22].

For plastic materials, such as polymers, with a complex deformation behavior (see section 2.3.2) this simplification is not feasible [32], resulting in a non-linear stress distribution across the specimen thickness. Figure 2.13 shows the idealized and the true stress distribution for a 3PB specimen.

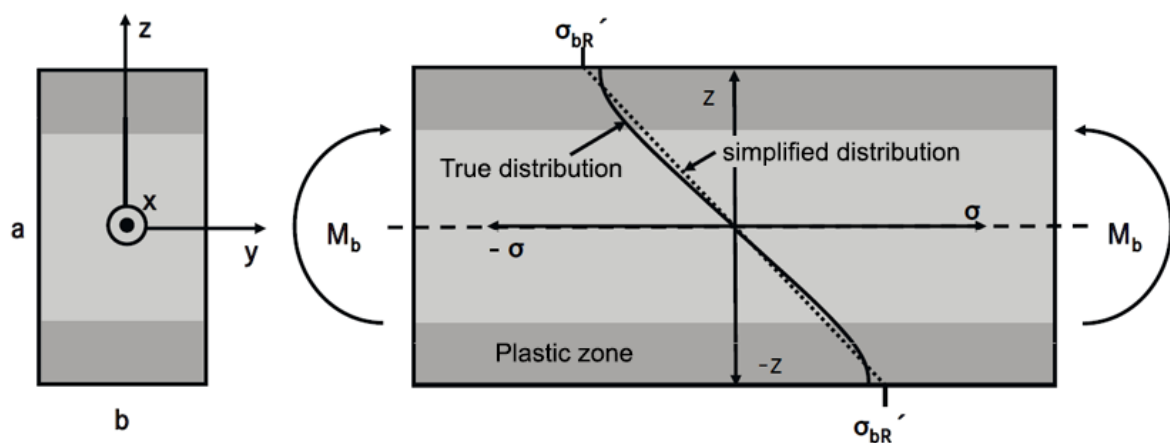


Figure 2.13: Simplified and true stress distribution in 3PB specimen; taken from Heine [32] and translated.

Eq. 2.8 shows that the general equation for the deflection depends on the span distance the specimen dimensions and the Young's modulus. Especially during plastic deformation, these parameters vary during the 3PB test resulting in a strong nonlinearity of the test results [22]. This characteristic becomes even more pronounced for higher deflections [22]. Therefore, 3PB tests are usually stopped after the deflection reached 1.5 times the specimen thickness (= 6 mm deflection or 3.5 % bending strain for a standard 4 mm specimen) [31]. However, these influences can partially be compensated by a reverse engineering approach to generate the material model (see section 3.8.1.2). Therefore, the 3PB tests were extended to 15 % bending strain.

2.3.2.3 Compression testing

Based on the limited field of applications, compression tests are not as commonly used as tensile or 3PB tests [22]. However, compression tests are required for construction materials (e.g., concrete, polymer concrete, wood, and insulating materials), materials used for dampers, plain bearings, sealing materials (e.g., copper alloys, Polyamide, Polyethylene or rubbers) or packaging materials such as paper or foams [22]. In compression tests with constant test speed, similar boundary conditions as tensile tests are applied (impact free, constant increasing load until break or a certain force is reached) [22]. As a result, the general equations are similar when compared to equations of tensile tests (see section 2.3.2.1) [22, 33]. The nominal compressive strain, ε_{comp} was calculated with Eq. 2.12 [33].

$$\varepsilon_{comp} = \frac{\Delta L_{0,comp}}{L_{0,comp}} \cdot 100 \% \quad (2.12)$$

Where $L_{0,comp}$ in mm, is the total specimen height and $\Delta L_{0,comp}$ in mm, is the elongation (or compression) during the measurement [33]. The compressive stress σ_{comp} in MPa was calculated using Eq. 2.13

$$\sigma_{comp} = \frac{F_{comp}}{h_{struc} \cdot b_{struc}} \quad (2.13)$$

with the compression force F_{comp} in N, the total thickness h_{struc} in mm and the total width b_{struc} in mm [33]. The nominal compressive modulus was calculated in the strain

range of 0.05 % – 0.25 % using the compressive stress σ_{comp} and strain ε_{comp} and Eq. 2.14 [33].

$$E_{comp} = \frac{\Delta\sigma_{comp}}{\Delta\varepsilon_{comp}} \bigg|_{\varepsilon_{comp}=0.05\%}^{\varepsilon_{comp}=0.25\%} \quad (2.14)$$

Due to friction at the contact areas of the specimen and the compression plates, a homogeneous stress – strain distribution is achieved only at sufficient distance to the contact area between specimen and test setup [33]. The friction hinders the deformation and leads to conical deformed elastic zones in the specimens [22]. Especially for ductile material this leads to plastic deformation in the middle of the specimen resulting in bulging and failure caused by shear fracture. To either reduce or increase the friction, lubrication or fine sandpaper is applied to the contact zone between specimen and test setup.

2.3.3 Dynamic Mechanical Analysis

To characterize the temperature dependency of the mechanical behavior of polymers, dynamic tests with sinus shaped loadings are commonly performed [28]. In addition, by varying the frequency of the input signal, the time dependency can be measured using the same test setup [22]. With such dynamic mechanical analysis (DMA), the viscoelastic properties of polymers can be investigated within a short period of test time [22]. An important criteria for a DMA measurement is that the load (either stress or strain) is way below the typical mechanical loads in quasi-static tests or the application of a parts itself [28]. Based on a small sinusoidal load, the response (amplitude and phase shift) of the material is measured [28]. Figure 2.14 shows the stress response for a sinus shaped input strain for a pure elastic material and a polymer within the linear-viscoelastic deformation region [28].

For a perfectly elastic material, no phase shift is observed. Whereas for polymers, a pronounced phase shift can be detected. Within the linear-viscoelastic region, Boltzmann's superposition principle (meaning that if strain 1 results in stress 1 and strain 2 results in stress 2 the sum of strain 1 and 2 equals to the sum of stress 1 and 2 and vis versa) can be applied [28]. Beyond the linear viscoelastic region, this principle cannot be applied anymore (non-linear viscoelastic region). For DMA measurements, the effect of non-linear

viscoelastic deformation can be seen in an additional load dependency of the materials response [28].

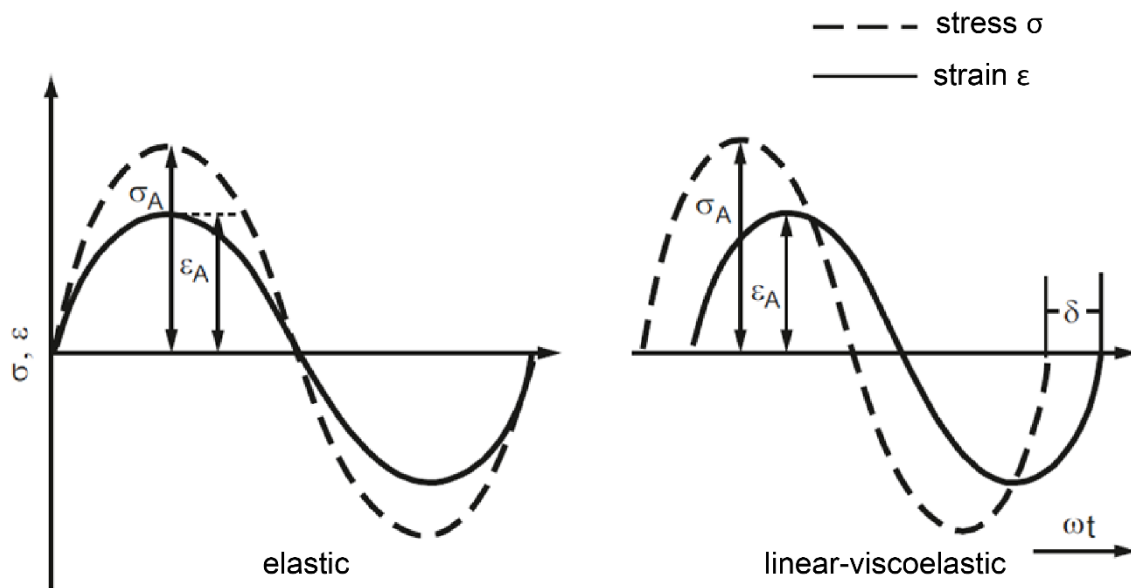


Figure 2.14: Dynamic stress – strain response of an elastic (left) and linear-viscoelastic material (right); taken from Ehrenstein [28] and translated.

Transferring the sinus shaped test data into the complex number space, Figure 2.15 shows the resulting complex modulus E^* based on storage modulus E' and the loss modulus E'' which are coupled by the phase shift δ [22].

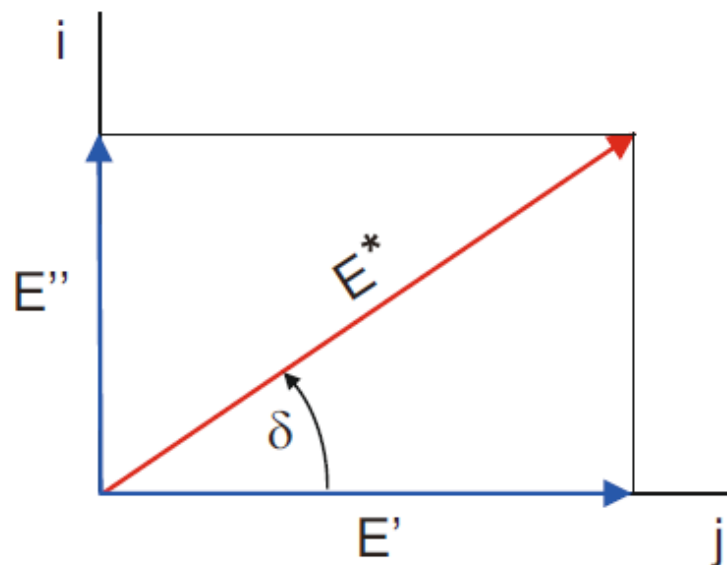


Figure 2.15: Schematic of the complex modulus with the loss modulus, storage modulus and; taken from Grellmann and Seidler [22].

The calculation of the complex modulus E^* is shown in Eq. 2.15 [22]. Based on the phase shift δ and the stress and strain amplitude values σ_A and ε_A , the main DMA results (storage modulus E' (see Eq. 2.16) and loss modulus E'' (see Eq. 2.17)) can be calculated.

$$E^* = E' + i \cdot E'' \quad (2.15)$$

$$E' = E^* \cdot \cos(\delta) = \frac{\sigma_A}{\varepsilon_A} \cdot \cos(\delta) \quad (2.16)$$

$$E'' = E^* \cdot \sin(\delta) = \frac{\sigma_A}{\varepsilon_A} \cdot \sin(\delta) \quad (2.17)$$

Within this thesis, only thermoplastic polymers are investigated and therefore only this type will be covered in more detail in this section. Thermoplastics are non-crosslinked polymers which are hard-elastic, rigid and melt at higher temperatures [28]. Furthermore, thermoplastics can be divided in amorphous and semicrystalline thermoplastics [28]. Figure 2.16 shows a characteristic temperature dependency curve for a semicrystalline thermoplastic polymer (for example Polyamide 6) [28]. The figure shows the storage modulus G' and the loss modulus G'' (shear tests based), and the mechanical loss factor $\tan(\delta)$ based on DMA measurements for each temperature. For semicrystalline thermoplastics, the area of application spans up to the melting temperature [28]. The glass transition temperature T_g separates the energy elastic and the entropy elastic state [28]. Within the energy elastic state, deformations under load are generally caused by reversible changes in atomic distances and changes of valence angles of chemical bonds of the polymer chains. In the entropy elastic temperature range, the molecules are allowed to form a stretched state due to an increase of rotation and rearrangement possibilities of chain segments and side chains (the micro-Brownian movements) [28]. The stretching of molecules leads to an unlikely shape which results in decreasing entropy [28]. For DMA measurements, the evaluation of the peak positions for the loss modulus and especially the mechanical loss factor is key for determining the different temperature ranges [22, 28].

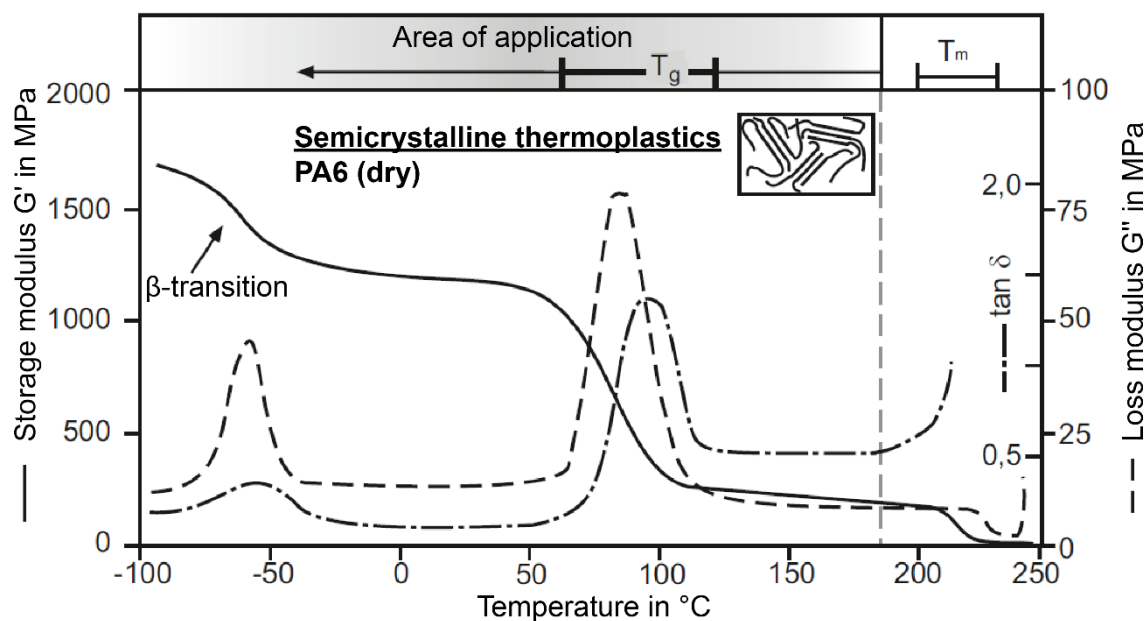


Figure 2.16: Characteristic DMA results for semicrystalline thermoplastic polymers; taken from Ehrenstein [28] and translated.

2.4 FEM Simulations

With the evolution of digital systems in the past decades the Finite-Element-Method (FEM) found its way into multiple engineering applications [34, 35]. The essence of FEM simulations is the discretization of a continuous problem with a set of equations which can be solved using numerical methods [35]. With the increase of computational performance over the past decades, FEM gained in importance [35 - 37] too. Nowadays, FEM simulations are widely used in engineering to solve physical problems and can be found in almost every field of engineering [35]. In structural engineering, parts often have complex shapes, material compositions and multiple static and dynamic boundary conditions [36]. Such continuous systems require differential equations with numerous state variables which in general have no closed-form solution [36]. To solve this issue, FEM was developed [36]. The main steps for performing a FEM analysis are shown in Figure 2.17 [34].

First, in the modeling step, the real physical problem needs to be discretized and the appropriate boundary conditions must be applied to the model [34]. In the second step, the system of equations are set up by assembling the global stiffness matrix and load vectors from all the individual element matrices and vectors [34]. The model size is generally defined by the size of the discretization, which determines the amount of

elements and the number of equations which need to be solved [35]. Finally, all equations are solved resulting in the deformation vector, the stress tensor and the reaction force vector [34].

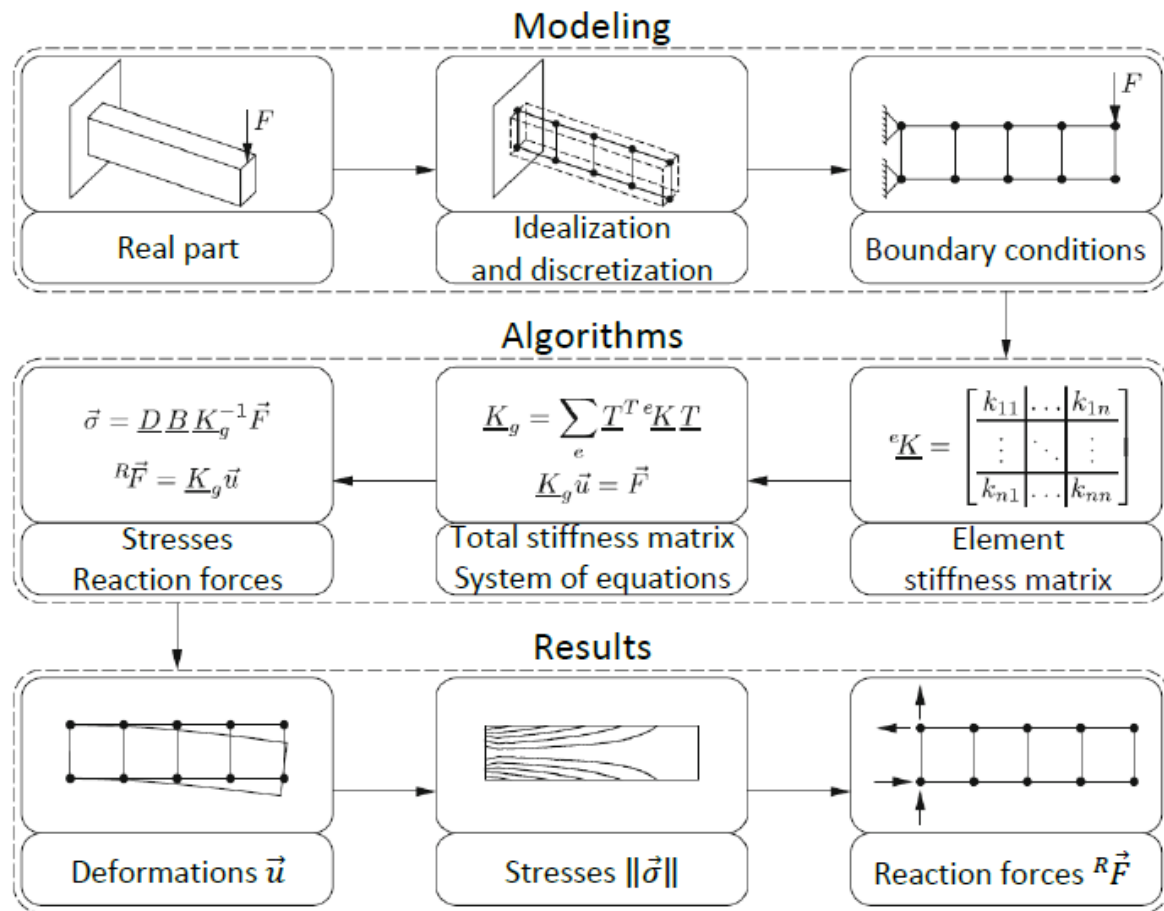


Figure 2.17: Steps of FEM; taken from Steinke [34] and translated.

The accuracy of FEM simulations is defined by [36]:

- mesh size,
- element type,
- material behavior and material data,
- numerical accuracy of the calculation and
- the model adequacy.

The mesh size and element type are important parameters when it comes to numerical accuracy [36]. Gathering adequate material data and choosing a suitable material model is key to achieve good simulation results, especially for polymers as they often show complex

deformation behaviors (see section 2.3.2) [37, 38]. Another influence on the numerical accuracy of the calculation is given by the chosen solver [36]. Finally, an adequate mesh size depends on the simulation type (dynamic mesh can be coarser than static and coarser than lifetime simulations), the available computational resources (storage and CPU power) and the dimensions of the part [36].

2.4.1 Material modeling

The mechanical behavior of polymers is described by mathematic formulations which are known as material models [37]. Due to the complexity of polymer deformation (as described in section 2.3.2) typically different material modeling approaches are required based on the goal of a FEM simulation. The mathematic formulations describe the stress and strain depending on time, temperature and model specific material parameters [37]. Beyond that, there are also material models available to describe environmental effects like moisture, UV-radiation, or chemical degradation. Additionally, special models for static, monotonic or cyclic loads were established [38]. Figure 2.18 shows a schematic diagram of a possible test program to investigate input parameters for a FEM simulation [38].

Depending on the requirements of the simulation project, mechanical characterization (e.g. uniaxial tensile, 3PB, impact, hardness, compression or shear tests), surface characterization (e.g. optical microscopy, scanning electron microscopy or atomic force microscopy), thermal characterization (e.g. differential scanning calorimetry or pvt-measurements) or chemical characterization (e.g. Fourier transform infrared spectroscopy, energy dispersive spectroscopy or thermogravimetric analysis) might become necessary [38].

Depending on the timescale, different material models are better suited for impact, short-term, long-term or periodic loads [37]. Within this study, only short-term mechanical loads will be analyzed and therefore only this case will be discussed in more detail. Polymers show a strong nonlinearity in their deformation behavior (see section 2.3.2) and therefore the assumption of linear elasticity might only be adequate for simple static FEM simulation of brittle materials with small strain. The simplest material model for unreinforced thermoplastic polymers is the linear elastic isotropic material model [37]. Based on Hook's

law for isotropic materials, only the Young's modulus (see Eq. 2.6) and the Poisson's ratio (see Eq. 2.21) are required as input parameters for the material model [37].

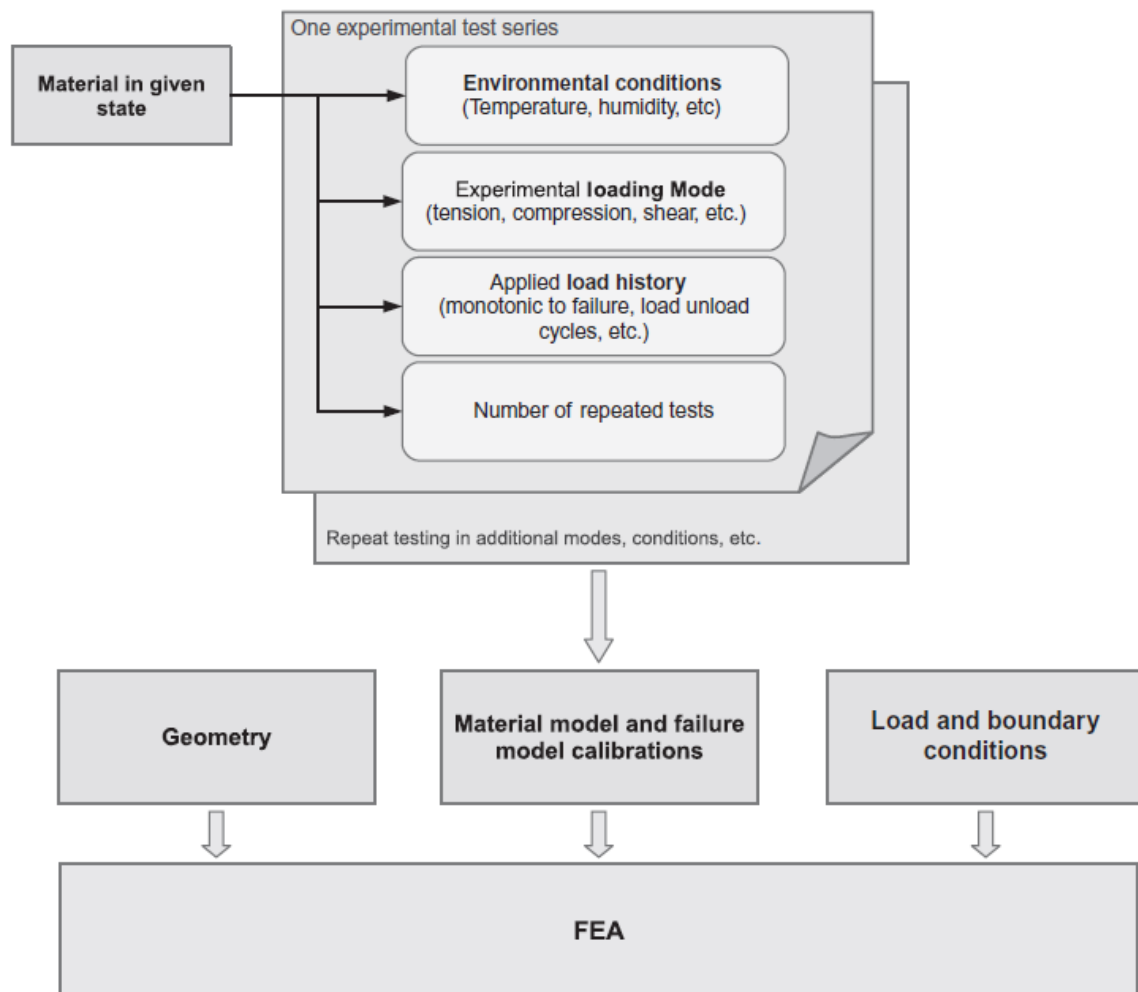


Figure 2.18: Input parameters for a possible test program to investigate material data; taken from Bergstrom [38].

Due to the already mention non-linear behavior of polymers, elastic-plastic material models increase the quality of simulations with higher strains significantly [37]. Figure 2.19 shows a simple stress – strain curve to illustrate the linear elastic and the elastic-plastic region during deformation. The figure shows that for deformations below the yield strength, a linear elastic material model is sufficient, but beyond the yield strength an elastic-plastic model is beneficial[37].

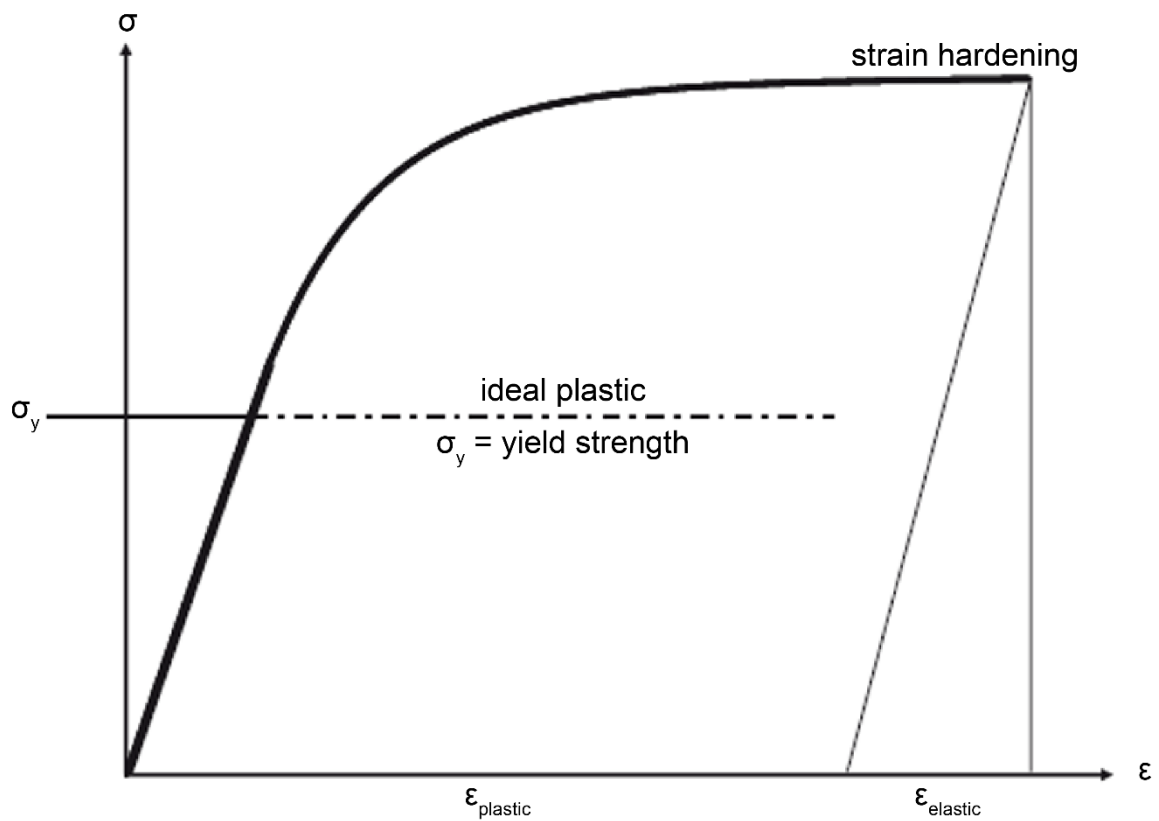


Figure 2.19: Stress – strain curve with elastic and plastic strain regions and strain hardening; taken from Korte [37] and translated.

The strain calculation for an elastic-plastic material model in “Abaqus FEA 2019” (Abaqus) (Dassault Systèmes Simulia, France) is based on Eq. 2.18 [39].

$$\epsilon_{total} = \epsilon_{elastic} + \epsilon_{plastic} \quad (2.18)$$

The equation shows that the total strain ϵ_{total} is the sum of the elastic strain $\epsilon_{elastic}$ and plastic strain $\epsilon_{plastic}$ [39]. In this study, the elastic strain $\epsilon_{elastic}$ was calculated using a linear elastic material model with Young’s or flexural modulus and Poisson’s ratio [40]. The plastic strain $\epsilon_{plastic}$ is based on yield stress – plastic strain data. In Abaqus various ways to define yield stress – plastic strain data are implemented [39], the two covered in this study are:

1. Predefined unidirectional yield stress – plastic strain curves [41]
2. Johnson-Cook strain hardening model [42]

2.4.1.1 Calculation of yield stress – plastic strain

Figure 2.20 illustrates (based on an uniaxial tensile test) how the test data must be treated to gain the necessary data for an elastic-plastic material model [37]. First the part up to the yield strength σ_{yield} is used to calculate the elastic part (characterized by the Young's modulus and Poisson's ratio). Beyond the yield strength, the yield stress – plastic strain data is calculated to create the data for the plastic part of the material model.

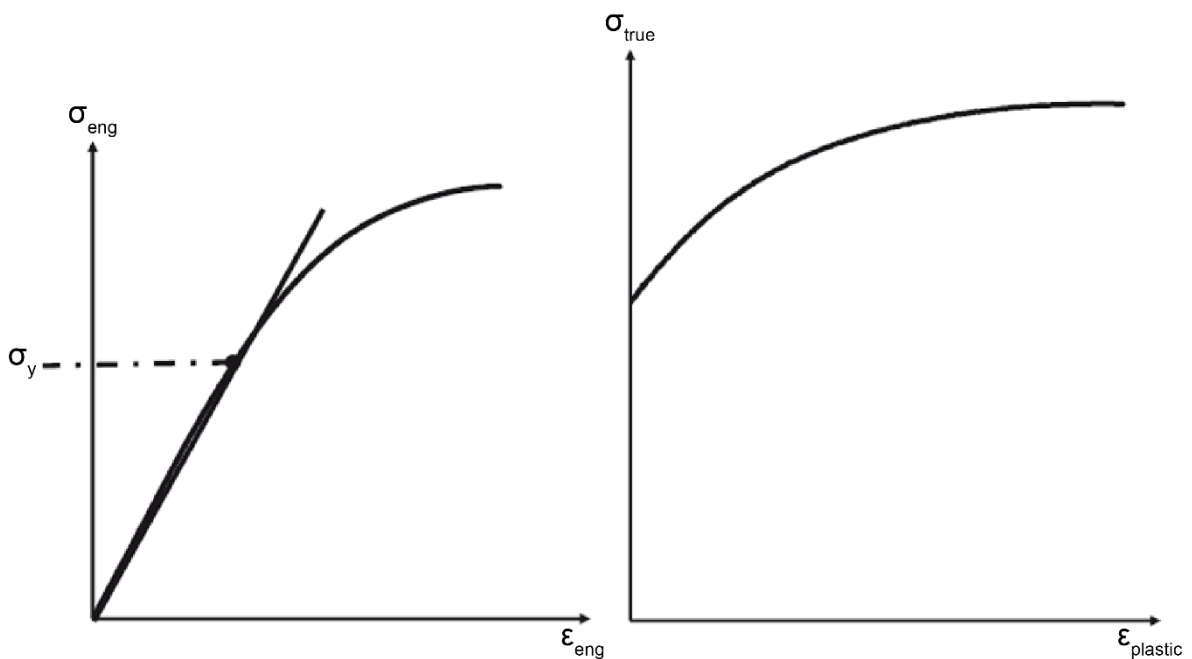


Figure 2.20: Converting a stress – strain curve to gather an elastic-plastic material model; taken from Korte [37] and translated.

The yield stress – plastic strain data can directly be calculated from tensile test data [37, 38]. Figure 2.21 shows a reference volume under uniaxial tension for a) unloaded and b) loaded state to illustrate the calculation steps necessary [43].

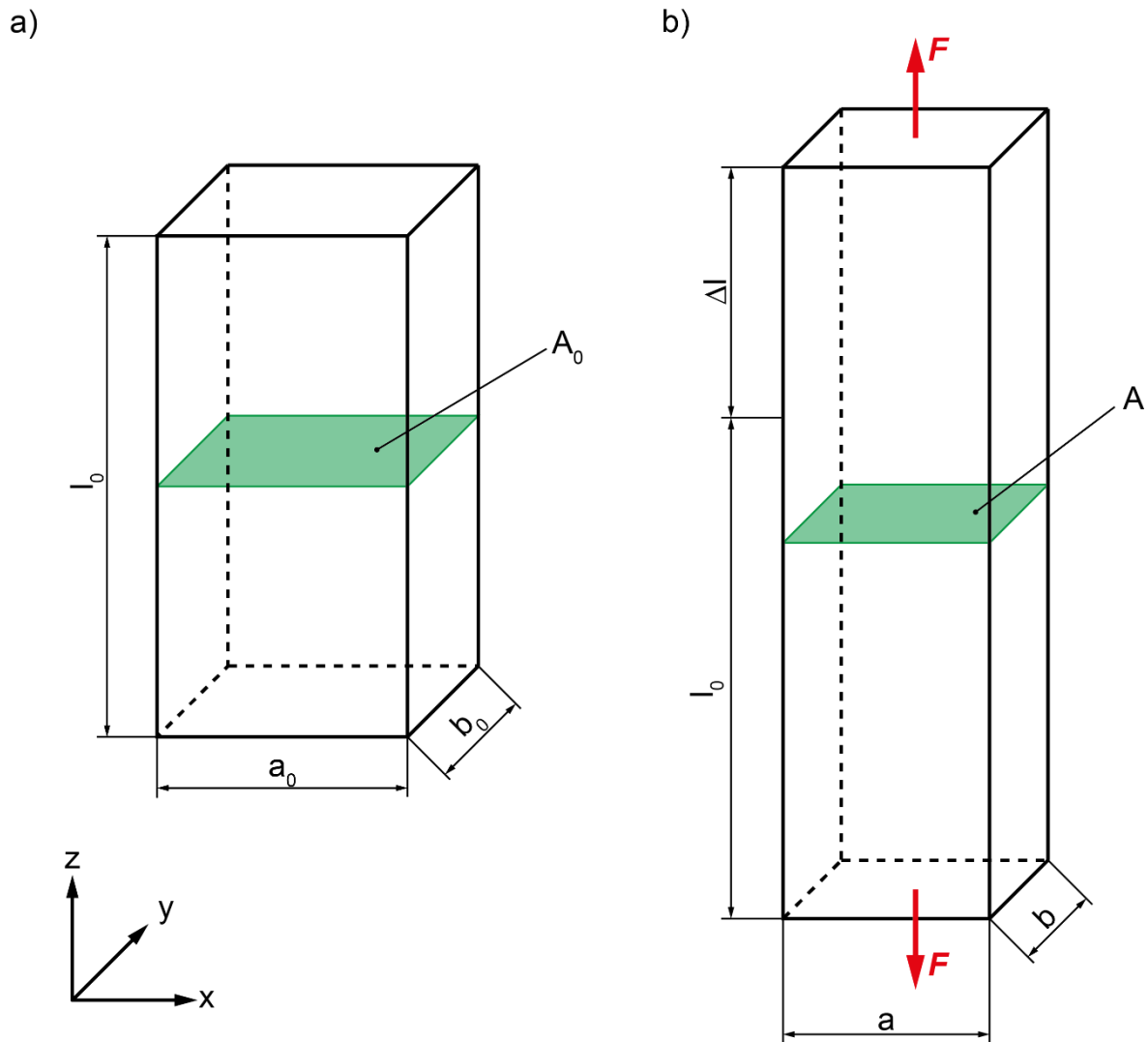


Figure 2.21: Reference volume under uniaxial loading for a) unloaded and b) loaded state.

The engineering strain, obtained from the tests, is based on the initial length l_0 and must be converted to true strain using the integral of the reciprocal of the length \hat{l} and the relationship in Eq. 2.4. Resulting in the formula for the true strain ε_{true} shown in Eq. 2.19.

$$\varepsilon_{true,l,t} = \int_{l_0}^l \frac{1}{\hat{l}} d\hat{l} = \dots = \ln(1 + \varepsilon_{eng,l,t}) \quad (2.19)$$

The initial cross section A_0 is calculated using Eq. 2.20

$$A_0 = a_0 \cdot b_0 \quad (2.20)$$

were a_0 and b_0 are the width and thickness of the reference volume, respectively. The definition of the Poisson's ratio (as shown in Eq. 2.21) with the true transversal strain $\varepsilon_{true,t}$ and the true longitudinal strain $\varepsilon_{true,l}$ is used to calculate the transversal strain according to Eq. 2.22.

$$\nu_{true} = -\frac{\varepsilon_{true,t}}{\varepsilon_{true,l}} \quad (2.21)$$

$$\varepsilon_{true,t} = -\nu_{true} \cdot \varepsilon_{true,l} \quad (2.22)$$

The true cross section A is defined using Eq. 2.23

$$A = a_0 \cdot (1 + \varepsilon_{true,t,x}) \cdot b_0 \cdot (1 + \varepsilon_{true,t,y}) \quad (2.23)$$

where $\varepsilon_{true,t,x}$ and $\varepsilon_{true,t,y}$ are the transversal strain in x- and y-direction, respectively [43]. Assuming that the Poisson's ratio in z-x direction $\nu_{true,zx}$ is equal to the Poisson's ration in z-y direction $\nu_{true,zy}$ (see Eq. 2.24) and inserting Eq. 2.20 and Eq. 2.22 into Eq. 2.23, the true cross section can be calculated as Eq. 2.25.

$$\nu_{true,zx} = \nu_{true,zy} = \nu_{true} \quad (2.24)$$

$$\begin{aligned} A &= a_0 \cdot (1 - \nu_{true} \cdot \varepsilon_{true,l}) \cdot b_0 \cdot (1 - \nu_{true} \cdot \varepsilon_{true,l}) \\ &= A_0 \cdot (1 - \nu_{true} \cdot \varepsilon_{true,l})^2 \end{aligned} \quad (2.25)$$

Using the simple relationship for the stress σ , Force F and cross section \bar{A} in Eq. 2.26, the Force equilibrium can be written as shown in Eq. 2.27.

$$\sigma = \frac{F}{\bar{A}} \quad (2.26)$$

$$\sigma_{true} \cdot A = \sigma_{eng} \cdot A_0 \quad (2.27)$$

Using Eq. 2.27 with Eq. 2.25 and Eq. 2.21 leads to the relationship for the true stress σ_{true} as stated in Eq. 2.28.

$$\sigma_{true} = \frac{\sigma_{eng}}{(1 - \nu_{true} \cdot \varepsilon_{true,l})^2} = \frac{\sigma_{eng}}{(1 + \varepsilon_{true,t})^2} \quad (2.28)$$

With the true stress and true strain data the true Young's modulus E_{true} and the plastic strain $\varepsilon_{plastic}$ can be calculated with Eq. 2.29 and Eq. 2.30, respectively [43, 44].

$$E_{true} = \frac{\Delta\sigma_{true}}{\Delta\varepsilon_{true}} \Big|_{\varepsilon_{true}=0.05}^{\varepsilon_{true}=0.25} \quad (2.29)$$

$$\varepsilon_{plastic} = \varepsilon_{true,l} - \frac{\sigma_{true}}{E_{true}} \quad (2.30)$$

Only positive values of the plastic strain $\varepsilon_{plastic}$ are then considered for the calculation of the yield stress σ_{yield} with Eq. 2.31 [43, 44].

$$\sigma_{yield} = \sigma_{true} \Big|_{\varepsilon_{plastic}=0}^{\max(\varepsilon_{plastic})} \quad (2.31)$$

2.4.1.2 Johnson-Cook strain hardening model

Based on the von Mises plasticity, the Johnson-Cook plasticity model gives an analytic relationship between strain hardening, temperature and strain rate [36, 38]. The model calculates the yield stress σ_{yield} according to Eq. 2.32

$$\sigma_{yield} = [A + B \cdot \varepsilon_{plastic}^n] \cdot \left[1 + C \cdot \ln \left(\frac{\dot{\varepsilon}_{plastic}}{\dot{\varepsilon}_0} \right) \right] \cdot (1 - \hat{\theta}^m) \quad (2.32)$$

with strain rate and temperature dependency [36, 38].

The parameters A , B , n , C , m are material parameters that can be fitted based on experimental data [36, 38]. The first term (with A , B and n) describes the strain hardening for a reference strain rate $\dot{\varepsilon}_0$ [37]. The second term (with C , $\dot{\varepsilon}_{plastic}$ and $\dot{\varepsilon}_0$) describes the strain-rate dependency of the yield stress [37]. The third term (with $\hat{\theta}$ and m) describes the temperature dependency [37]. For this, the nondimensional temperature $\hat{\theta}$ is calculated using Eq. 2.33 with the glass transition temperature $\theta_{transition}$ and the melting temperature θ_{melt} [37].

$$\hat{\theta} \equiv \begin{cases} 0 & \text{for } \theta < \theta_{transition} \\ \frac{\theta - \theta_{transition}}{\theta_{melt} - \theta_{transition}} & \text{for } \theta_{transition} \leq \theta \leq \theta_{melt} \\ 1 & \text{for } \theta > \theta_{melt} \end{cases} \quad (2.33)$$

2.4.2 Element types

Besides the material model, the element type has a major influence on the quality of the simulation results [37]. Within this study, a few common element types were investigated. As previously described, the choice of the correct element type for the discretization of the real physical problem is key for achieving satisfying simulation results [36]. Referring to Korte [37], different element types can be distinguished by their:

- general shape,
- number of nodes,
- connectivity of the nodes,
- surface normal,
- element coordinate system,
- shape functions of the deformation and
- degree of freedom.

FEM software often offers elements with different shapes [37]. In general, they can be divided into one-dimensional (1D) (rod, beam), two-dimensional (2D) (triangular and quadrilateral) and three-dimensional (3D) (e.g., pentahedral, hexahedral or tetrahedral) elements [37]. Figure 2.22 shows commonly used element families available within Abaqus[45].

In addition, the number of nodes of each single element is an important factor for the characteristics of finite elements [37]. The total number of nodes of the system results from the number of nodes per element and the total number of elements which leads to the overall number of equations that must be solved by the numeric solver [35]. The minimum number of nodes for a single element is given by the geometry, meaning that every corner or end of an element (for 1D elements) leads to one node [37]. Furthermore, the number of nodes along the edge of an element are given by the polynomial degree of the shape function [35, 37]. Figure 2.23 shows a linear hexahedral continuum element with eight nodes, a quadratic hexahedral element with 20 nodes and a modified tetrahedral element with 10 nodes [45].

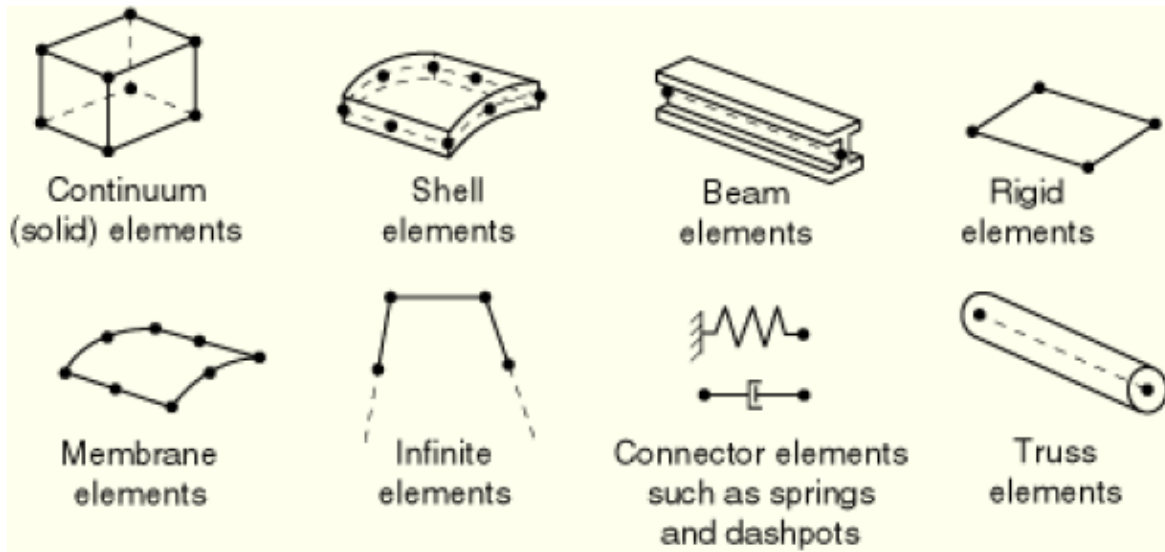


Figure 2.22: Frequently used elements in Abaqus; taken from ABAQUS Inc. [45].

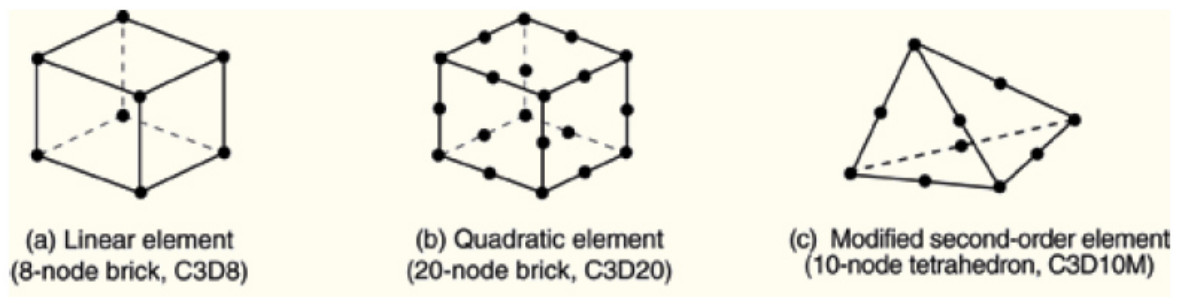


Figure 2.23: Three-dimensional continuum elements with Abaqus element label for a) linear hexahedral, b) quadratic hexahedral and c) modified second-order tetrahedral element; taken from ABAQUS Inc. [45].

In general, numerous different types of elements can be used within a FEM analysis. To create a consistent labeling of the different types, Abaqus uses the schematic shown in Figure 2.24 [34, 46]. The labeling illustrates the huge variety of different element types in modern FEM software.

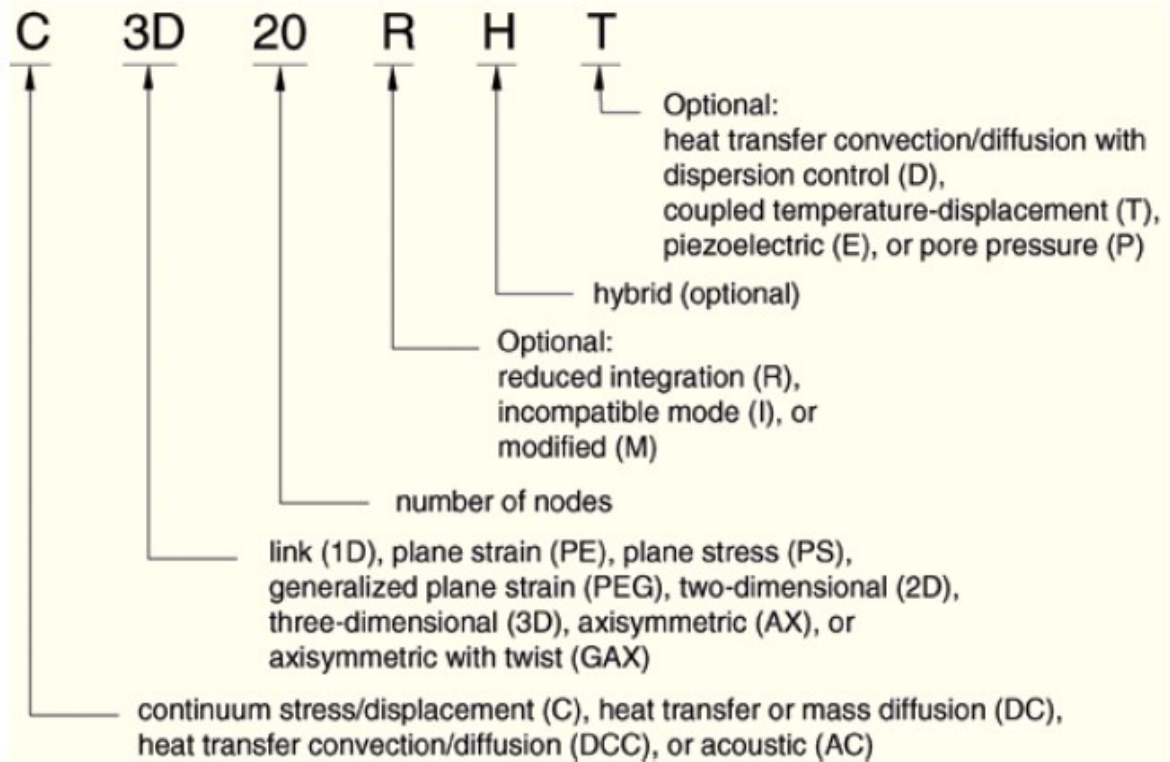


Figure 2.24: Element labeling scheme of Abaqus; taken from ABAQUS Inc. [46].

3 EXPERIMENTAL APPROACH

To determine the effect of the test- and material modeling methods on the simulation results of mechanical metamaterials, three different materials (PA12, PP, TPP) were mechanically tested at three different temperatures (-30 °C, 0 °C and 23 °C) each. Both tensile and three-point-bending (3PB) tests were performed for each combination of material and temperature. The results of these mechanical tests were used to create different material models to simulate the mechanical response of VS-structures when compressed. The simulations were then compared to compression tests of additively manufactured VS-structures. Three VS-structures with different geometric parameters were tested. In addition, impact tests, differential scanning calorimetry and dynamic mechanic analysis measurements were performed for further characterization of the materials. Figure 3.1 shows a flow chart with the experimental approach for this study.

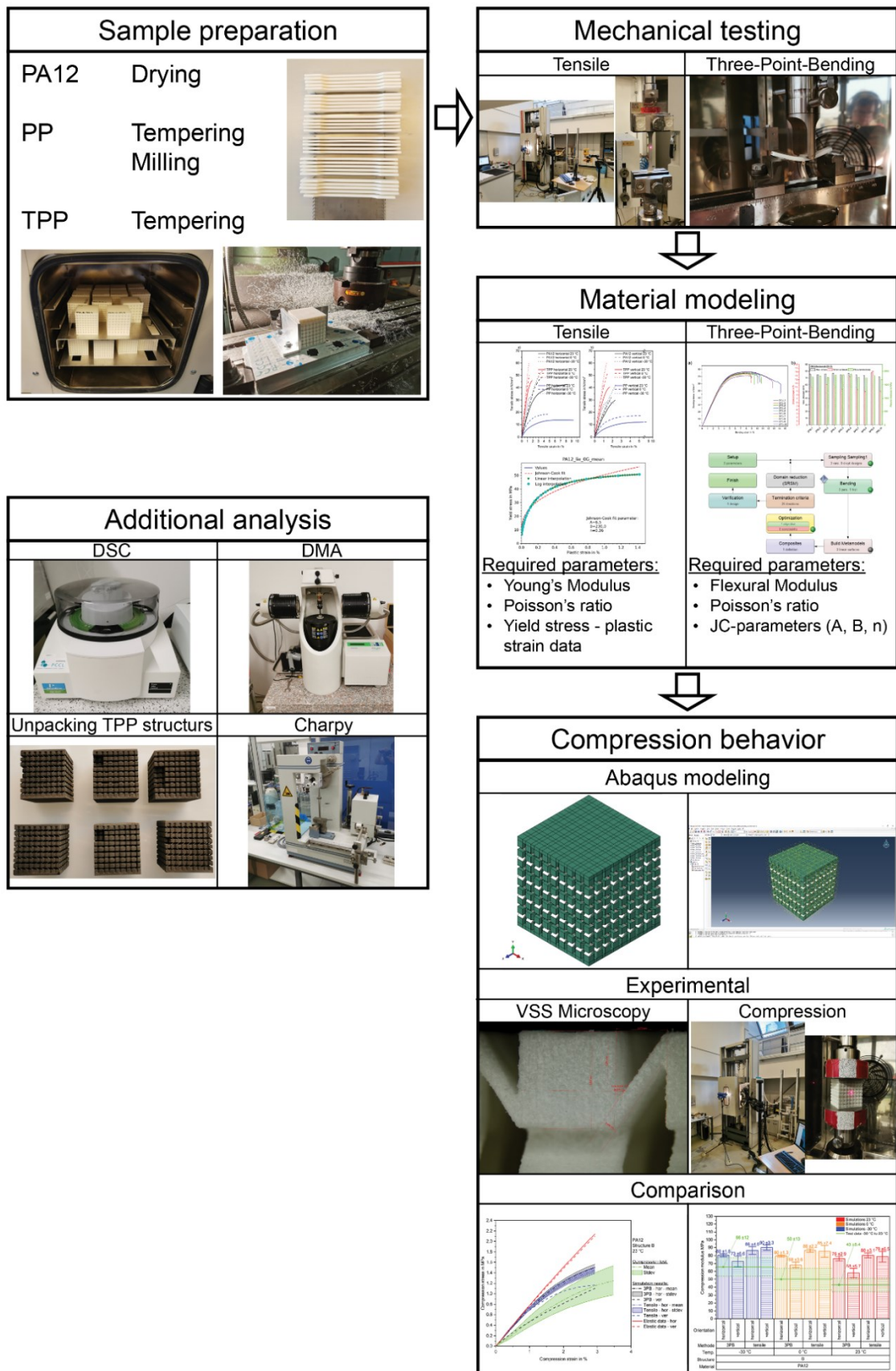


Figure 3.1: Flow chart of the experimental approach.

3.1 Materials

The following materials were used in this study:

- PA650 (PA12) – ALM-Advanced Laser Materials [47]
- LUVOSINT PP 9703 (PP) – Lehmann & Voss Co.KG [48]
- TIGITAL® 3D-Set TPP (TPP) – TIGER Coatings GmbH & Co KG [49]

The materials are special types for selective laser sintering and prepared according to the experience of the suppliers. For the upcoming discussion, the simplified names are used. The PA12 and PP specimens were manufactured by DISTECH Disruptive Technologies GmbH, Austria and the TPP specimens were produced by TIGER Coatings GmbH & Co KG, Austria.

TPP is a 3D printable thermoset in contrast to PA12 and PP, which are semi-crystalline thermoplastic polymers. For TPP, the part production is separated into two phases. First, the shaping step, where the powder is coarsely sintered to the final shape but with low mechanical properties (green part). In the second phase, the curing step, the parts are unpacked from the remaining polymer powder and repacked with temperature resistance salt and finally heat treated to achieve their final properties. During this final heat treatment, the material is cured to achieve its final cross-linked polymer network (brown part).

3.1.1 Specimen geometries

The tensile, 3PB and impact specimens were directly printed according to the dimensions specified in their respective standards. To increase the clamping area during the tensile tests, the shoulder length was increased by 25 mm on each side. Figure 3.2 shows the dimensions of the specimens. The tests were performed with both horizontal (parallel to the print direction) and vertical (perpendicular to the print direction) manufactured specimens. Figure 3.3 shows a tensile and a 3PB specimen in horizontal and vertical direction.

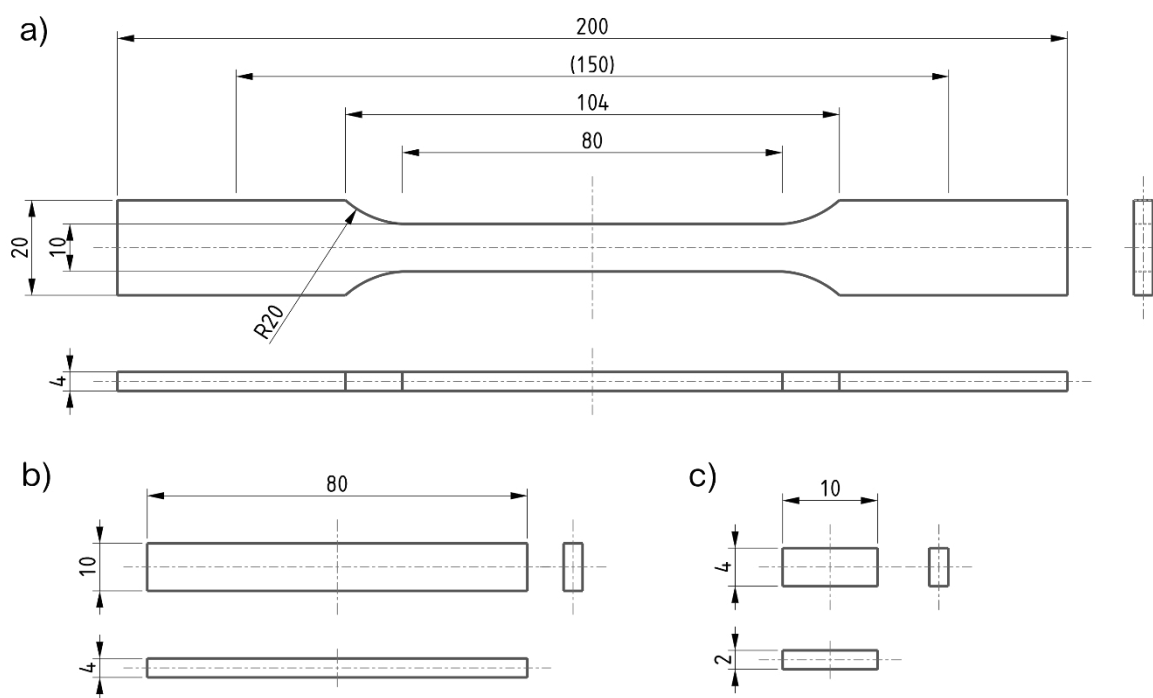


Figure 3.2: Dimensions of a) tensile-, b) 3PB- and Charpy-, c) DMA specimens.

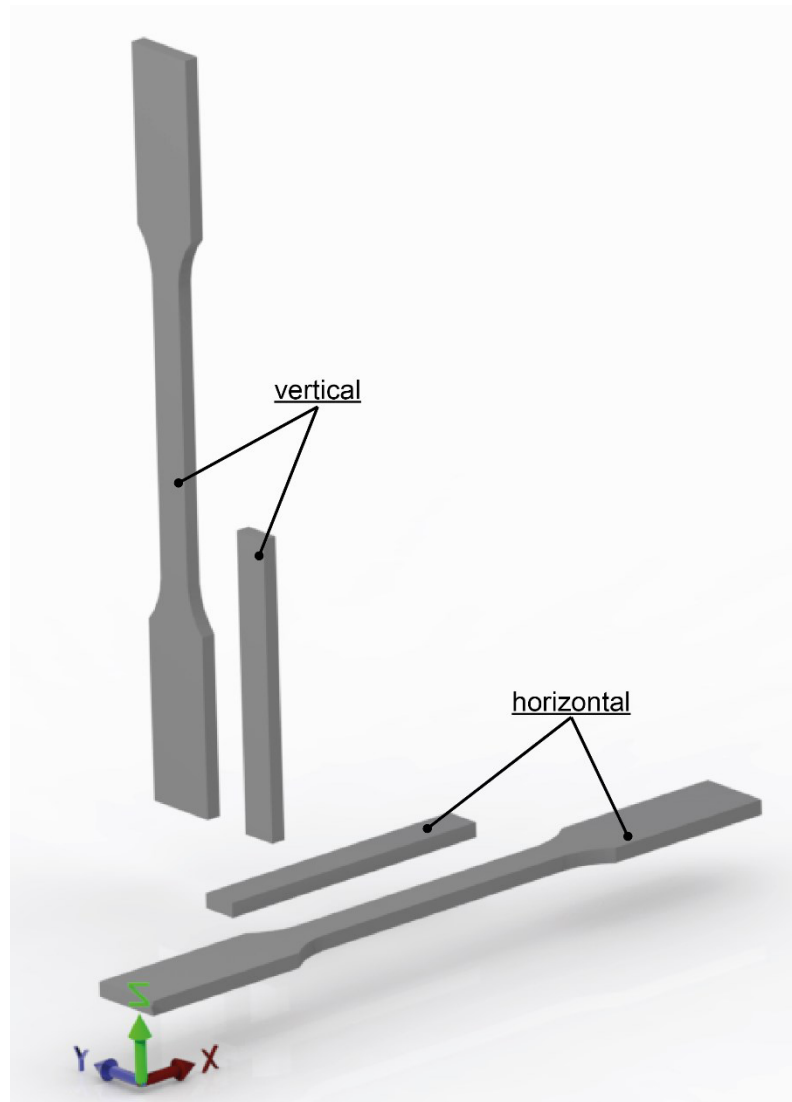


Figure 3.3: Horizontal and vertical print orientation in the SLS build volume. The build direction is along the z-axis.

3.1.2 Variable Stiffness structures

The stiffness of technical components plays a key role in the design of polymer parts. The ability of tuning the stiffness, especially in different directions, leads to multiple new fields of applications [7]. In this study, a mechanical metamaterial with variable stiffness was used [7].

3.1.2.1 Unit Cell of VS-structure

The stiffness of the whole structure can be adjusted by changing the geometric parameters of the unit cell (UC) [7]. Figure 3.4 show the design of the UC in detail. The UC consists of

cubes connected with alternately oriented struts. The arrangement of struts allows the structure to perform an in-plane movement with no out-of-plane deformation when a force is applied [7]. Table 3.1 lists the parameters of the UC and their description.

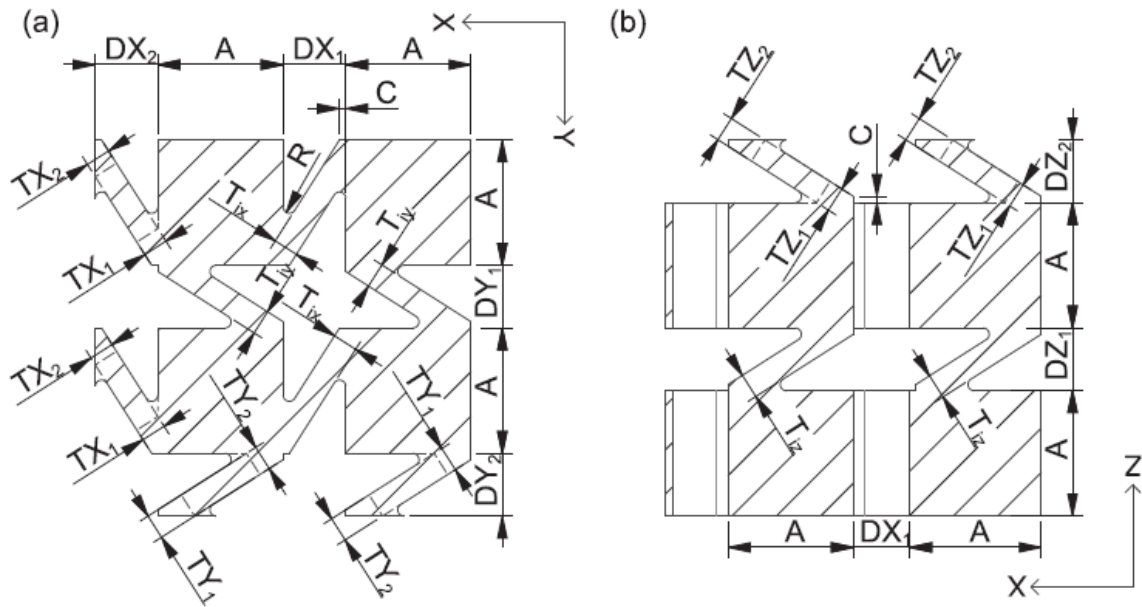


Figure 3.4: Geometric parameters of the VS-structure unit cell; taken from Fleisch et al. [7].

Table 3.1: Description of the geometric parameters of the VS-structure unit cells; taken from Fleisch et al. [7].

Name	Description
A	Side length of cubes
DX_1, DY_1, DZ_1	Distance between cubes (inside)
DX_2, DY_2, DZ_2	Distance between cubes (to next UC)
T_{ix}, T_{iy}, T_{iz}	Thickness of struts (inside)
TX_1, TY_1, TZ_1	Thickness of struts (to next UC, start)
TX_2, TY_2, TZ_2	Thickness of struts (to next UC, end)
R	Radius of fillets
C	Overhang of cubes

In addition, by stacking unit cells with different geometric parameters in all three directions a complex stiffness field can be created [7]. Different directional properties can be achieved with the following simplifications [7]:

1. Isotropic if: $D := DX_1 = DX_2 = DY_1 = DY_2 = DZ_1 = DZ_2$ and $T := T_{ix} = T_{iy} = T_{iz} = TX_1 = TX_2 = TY_1 = TY_2 = TZ_1 = TZ_2$
2. Transversal isotropic: e.g., if: $D_1 := DX_1 = DX_2 = DY_1 = DY_2$, $D_2 := DZ_1 = DZ_2$, $T_1 := T_{ix} = T_{iy} = TX_1 = TX_2 = TY_1 = TY_2$ and $T_2 := TZ_1 = TZ_2$
3. Orthotropic if: $D_x := DX_1 = DX_2$, $D_y := DY_1 = DY_2$, $D_z := DZ_1 = DZ_2$, $T_x := T_{ix} = TX_1 = TX_2$, $T_y := T_{iy} = TY_1 = TY_2$ and $T_z := T_{iz} = TZ_1 = TZ_2$

For this study isotropic VS-structures were investigated using the simplifications for parameter D and T . Therefore, a structure is defined by the set of geometric parameters listed in Table 3.2.

Table 3.2: Description of the geometric parameters of the unit cells investigated in this study.

Name	Description
D	Distance between cubes in three dimensions
A	Side length of cubes
T	Thickness of all struts
C	Overhang of cubes
R	Radius of fillets

3.1.2.2 Full-size VS-structures

Full-size structures are created by stacking unit cells in the three spatial directions. Additionally, a compression surface was added on top of the unit cells to ensure a good force transmission into the structure. Each compression surface had a thickness of 2 mm with outside dimensions of the structures. To investigate the effect on different stiffness levels, three structures (A, B and C) with different geometric parameters were manufactured and tested. Table 3.3 lists the goal values of the different parameters for structures A to C.

The overall dimensions of the structures were 50 x 50 x 54 mm³ (see Figure 3.5). Due to the lack of information regarding the orientation of the VS-structures, the print direction cannot be clearly determined. Due to the appearance of the structures, it is assumed that the build direction was along the z-axis. Figure 3.6 shows the three structures analyzed in this study.

Table 3.3: Goal values for the geometric parameters of the VS-structure A to C, referring to Figure 3.4 with simplifications as described in Table 3.2.

	Structure A	Structure B	Structure C
D in mm	2.5	2.2	2
A in mm	5	3.6	4.5
R in mm	0.2	0.2	0.2
C in mm	0.1	0.1	0.1
T in mm	0.8	0.8	0.8

To achieve a better quality of the Finite-Element-Method Simulations (FEM), the unit cell parameters were measured for each structure using a stereoscopic microscope (STEMI 2000, Carl Zeiss GmbH, Germany). The geometric parameters were measured on the two x-z surfaces at ten different positions of each VS-structure. To reduce the simulation effort (especially partitioning and meshing) the mean value of each parameter was calculated. Therefore, only one CAD-geometry for each geometry (structure A to C) and material (PA12 and PP) was generated. This led to, in total, six different structures (three for each material). During the microscopic analysis, magnifications of 10.4x (structure A) and 12.8x (structure B and C) were used.

Table 3.4 shows the final mean geometric parameters of PA12-VS-structures as measured. These values were used to create a 3D model which was then used for the FEM simulations. The 3D modeling of the structures was done using computer-aided design (CAD, "Creo Parametric 2.0", PTC Inc., USA). The radius of the fillets at the connection of the struts with the cubes (parameter R) could not be measured directly. Therefore, the length to the ground of the radius was measured and the true radius was modeled and measured using Creo. The parameter C couldn't be measured directly as well. In this case the goal parameter was used. Table 3.4 and Table 3.5 list the observed values and their respective standard deviation of the PA12 and PP structures, respectively. It has to be mentioned that it was only possible to determine the geometric parameters of the structure on the outside surface. Any dimensional changes inside of the structure could not be measured.

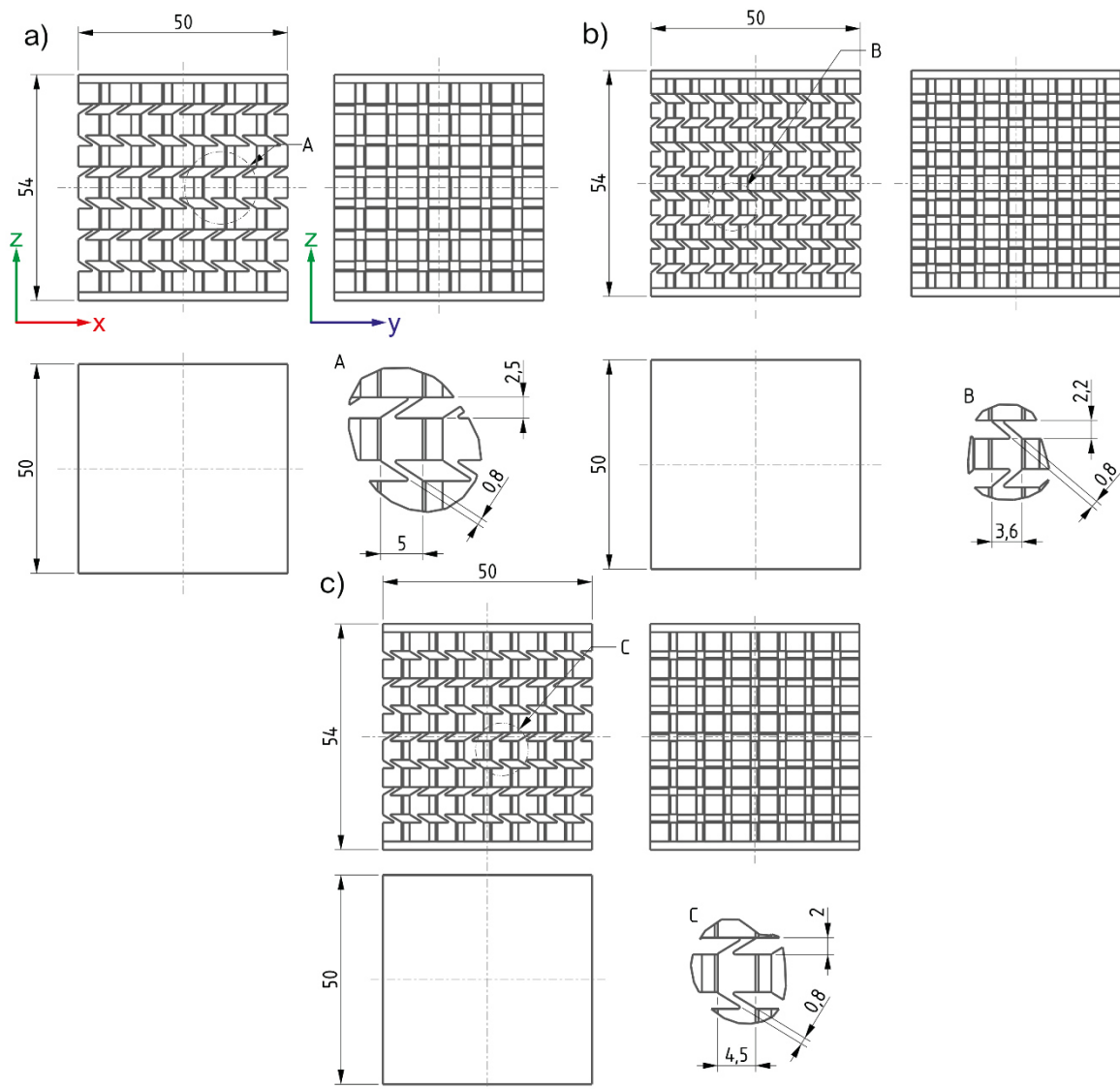


Figure 3.5: Dimensions of VS-structures with detailed main differential unit cell parameter for a) VS-structure A, b) VS-structure B and c) VS-structure C. The assumed build direction is along the z-axis.

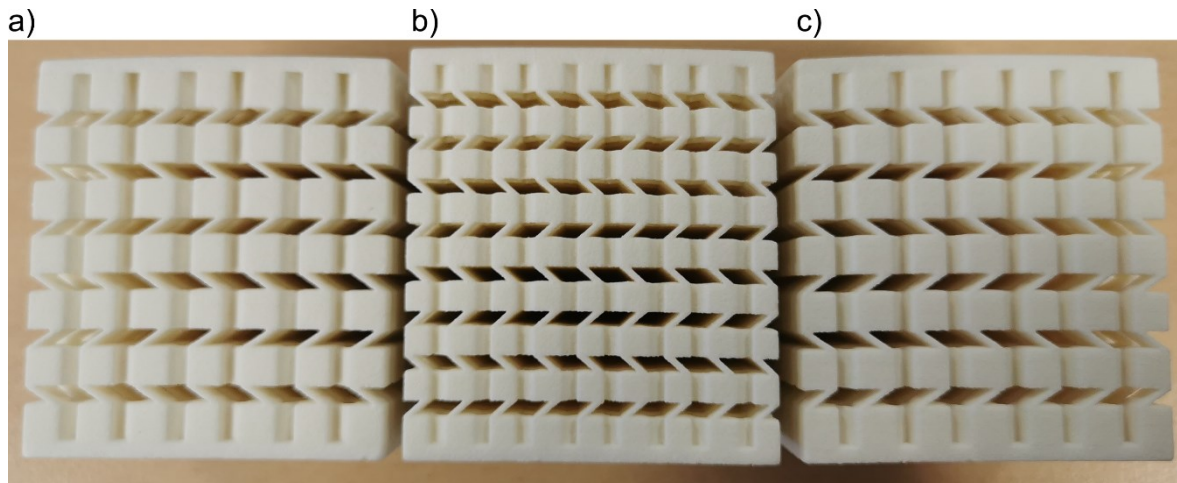


Figure 3.6: 3D printed VS-Structures. a) PP-VS-structure A, B) PP-VS-structure B and c) PP-VS-structure C.

Table 3.4: Mean values of real PA12-VS-structure geometry parameters.

	PA12		
	Structure A	Structure B	Structure C
D in mm	2.31 ± 0.10	2.18 ± 0.14	1.879 ± 0.088
A in mm	4.98 ± 0.09	3.69 ± 0.18	4.572 ± 0.066
R in mm	0.162 ± 0.032	0.225 ± 0.070	0.167 ± 0.030
C in mm	0.1	0.1	0.1
T in mm	0.886 ± 0.065	0.810 ± 0.065	0.860 ± 0.059

Table 3.5: Mean values of real PP-VS-structure geometry parameters.

	PP		
	Structure A	Structure B	Structure C
D in mm	2.31 ± 0.11	2.105 ± 0.096	1.879 ± 0.068
A in mm	4.774 ± 0.096	3.477 ± 0.071	4.428 ± 0.075
R in mm	0.157 ± 0.029	0.150 ± 0.030	0.160 ± 0.018
C in mm	0.1	0.1	0.1
T in mm	0.812 ± 0.041	0.835 ± 0.070	0.839 ± 0.047

3.2 Specimen and sample preparation

Depending on the type of material (PA12, PP or TPP), different preparation steps were necessary before the mechanical tests could be performed. Drying was required for PA12

and unwarping was needed for PP and TPP. In addition, unpacking tests were performed for the TPP VS-structures.

3.2.1 Drying of PA12

Due to its chemical structure, based on a polycondensation reaction for a carboxylic acid- and amine-group, PA12 is known to be hydrophilic [26]. Therefore, PA12 is prone to absorb moisture from the air [26]. The moisture content has a significant influence on the mechanical properties [30, 50]. To have a well-defined moisture content, both the standard specimens and VS-structures were dried at 80 °C in a vacuum drier. While drying, the weights of selected specimens and VS-structures were recorded. Drying was ended when no significant weight loss could be observed anymore. After drying, the specimens were kept under vacuum in the drier to avoid moisture absorption. Figure 3.7 shows the racked-up specimens and the structures in the dryer.

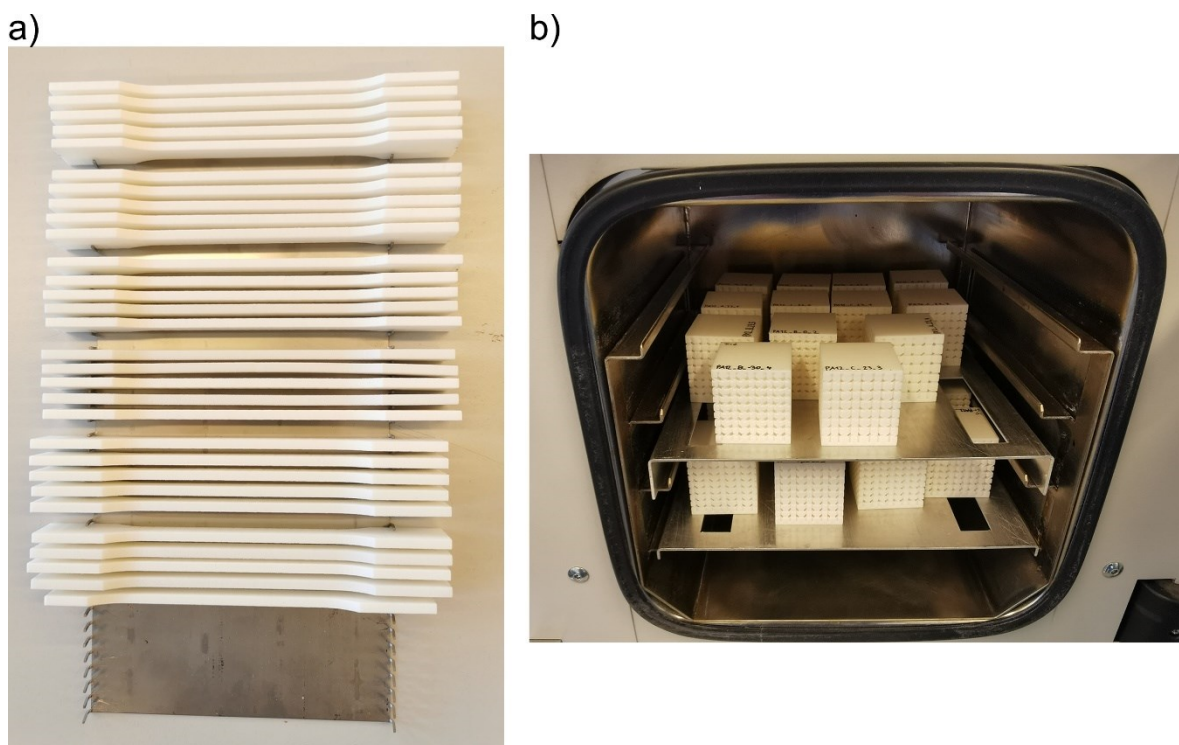


Figure 3.7: a) Racked-up PA12 specimens and b) PA12-VS-structures in the vacuum dryer.

Figure 3.8 a) and b) shows the mean relative weight loss of the reference specimens and the total relative weight loss after drying, respectively. Because the mechanical measurements were done in three steps, the drying times varied between the individual

measurements. It can be observed that the mean total weight loss of the vertical specimens is higher than the weight loss of the horizontal specimens. However, the deviation margins of the horizontal and vertical measurements are overlapping and therefore no significant trend can be observed. For the VS-structures A and C, only one structure was measured. No significant difference was observed in structures A and C when compared to structure B.

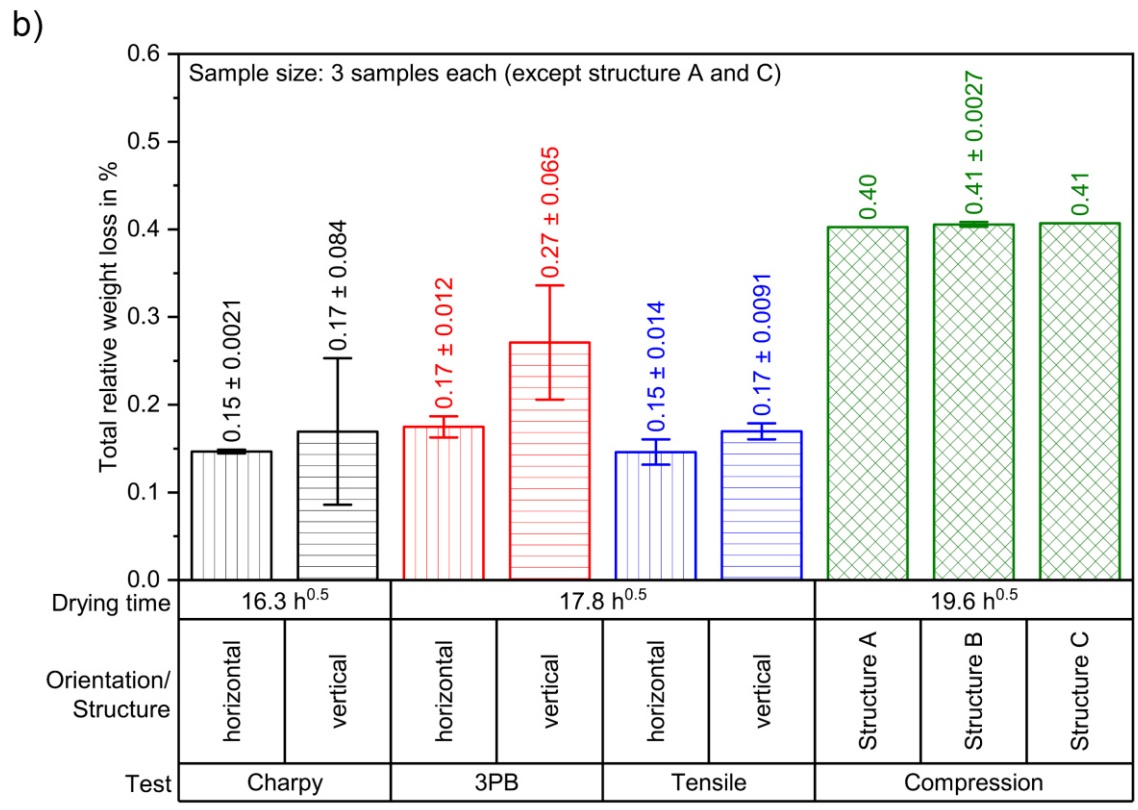
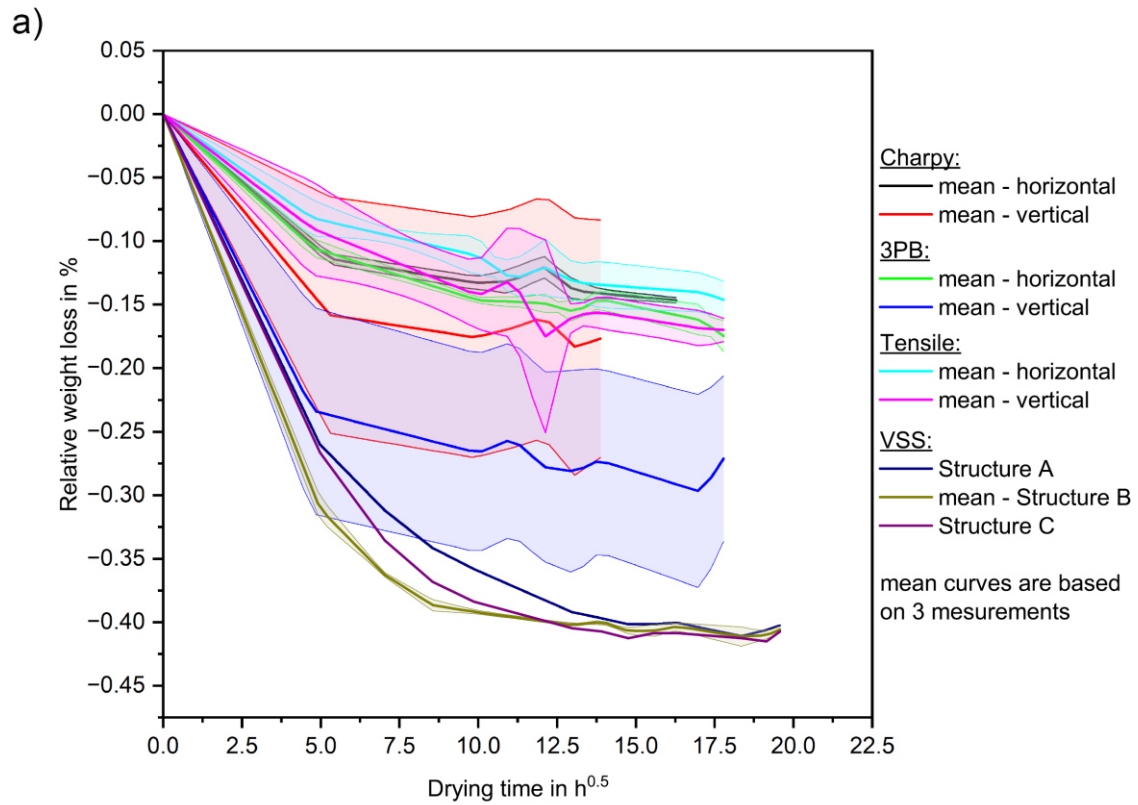


Figure 3.8: a) Mean relative weight loss while drying and b) total relative weight loss after drying.

3.2.2 Unwarping of PP specimens

Significant warpage of the PP specimens was observed after receiving them from the manufacturer. Figure 3.9 shows an example of a deformed PP specimen. To reshape and flatten the specimens, a heat treatment was necessary. In consultation with the manufacturer, different procedures were tested.

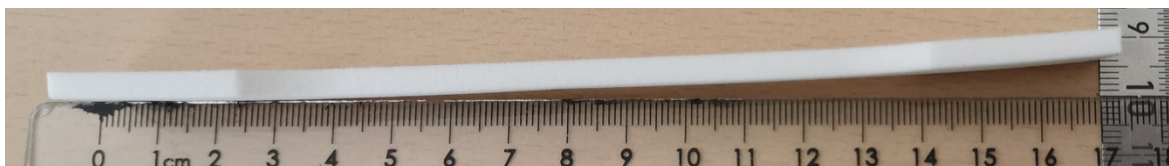


Figure 3.9: Warped specimens after delivery of a PP.

The PP specimens were placed between two steel plates in a cold oven with weights placed on top. Afterwards the oven was turned on and set to the target temperature. The heat rate was measured to be 6.5 K/min. Pretests with different target temperatures, holding times and loads per specimen were performed. The values of the pretests are listed in Table 3.6. Afterwards the oven was turned off and the specimens were cooled down in the closed oven chamber until room temperature was reached. Test No. 3 led to satisfactory results and was used for the subsequent annealing of all PP standard specimens (tensile, 3PB and Charpy).

Table 3.6: Pretest parameters for the annealing of PP.

Test	Target temperature	Holding time	Load / specimen
No. 1	80 °C	24 h	0 kg
No. 2	90 °C	7 h	3 kg
No. 3	90 °C	6 h	1 kg

For the VS-structures, no annealing procedure could be applied due to the risk of a deformation of the lattice structure itself. A heat treatment with an additional weight could have changed the geometric parameters of the unit cells. To be sure, that the annealing of the specimens did not change the crystallinity and consequently the mechanical properties of the PP, DSC measurements were performed with annealed and untreated specimens.

3.2.2.1 Differential Scanning Calorimetry

To investigate possible changes of the morphology of the PP while annealing, Differential Scanning Calorimetry (DSC) measurements for each heat treatment were performed. The measurements were performed on a “DSC 4000” (PerkinElmer Inc., USA). The samples were prepared by chipping of 0.01 g of material from annealed and untreated specimens using a knife. Five individual samples were tested each. Table 3.7 shows the test parameters and Figure 3.10 shows the temperature profile for 1st heating, cooling and 2nd heating. The start and final temperature for each heating cycle was set to -60 °C and 200 °C, respectively. A heating rate of +10 K/min was used. After a holding time of 3 minutes, cooling started with a temperature ramp of -10 K/min down to start temperature.

Table 3.7: DSC test parameters.

Repetitions	5 for each treatment (see Table 3.6)
Start temperature	-60 °C
Temperature ramp	± 10 K/min
Hold time	3 min
Final temperature	200 °C
Performed cycles	1 st heating, colling, 2 nd heating
Sample weight	≈0.01 g
Atmosphere	50 ml/min Nitrogen
Iridium check performed before first measurement	

Figure 3.11 shows the raw test data of an untreated PP sample. The overall shape of the curves for each test and annealing setting shows no change when compared to the reference measurement. Figure 3.12 shows the mean temperature positions of the characteristic peaks for the 1st heating, cooling and 2nd heating of the DSC measurements for the untreated samples and each tested annealing setting. The data shows that no significant change of the crystallinity can be observed, which leads to the conclusion that it is admissible that the VS-structures were not heat treated before testing.

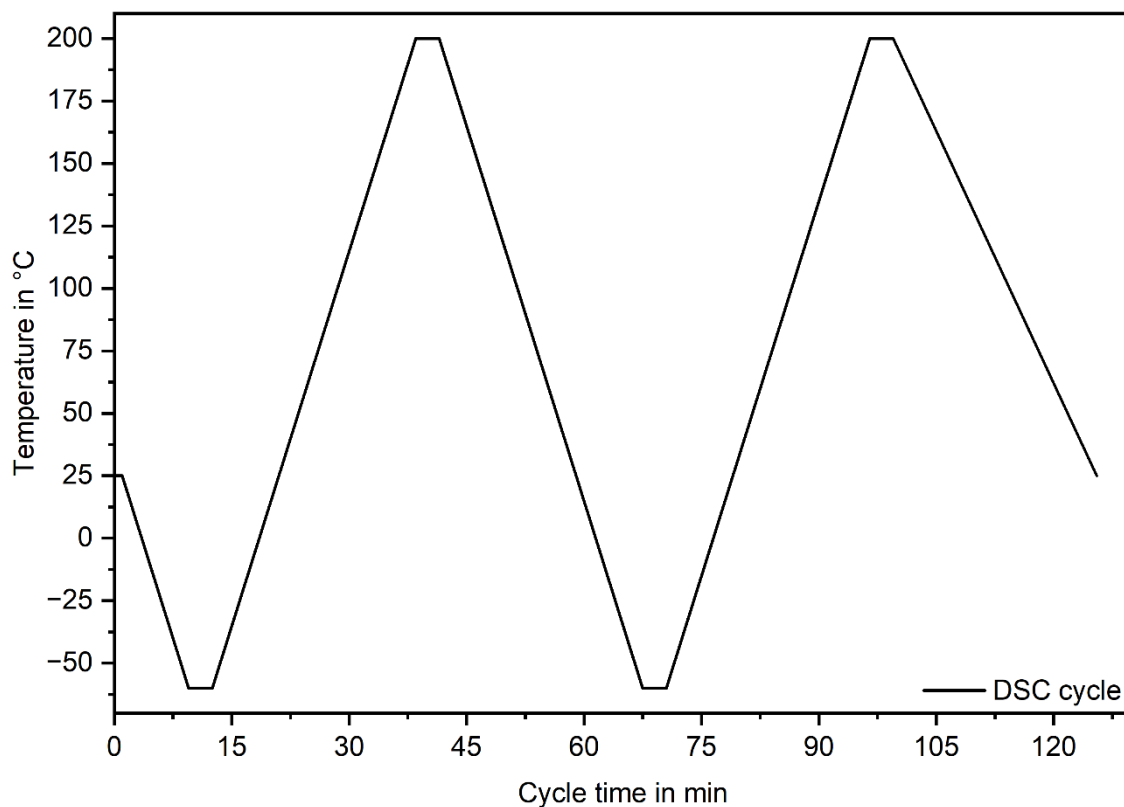


Figure 3.10: Temperature profile of the DSC measurements.

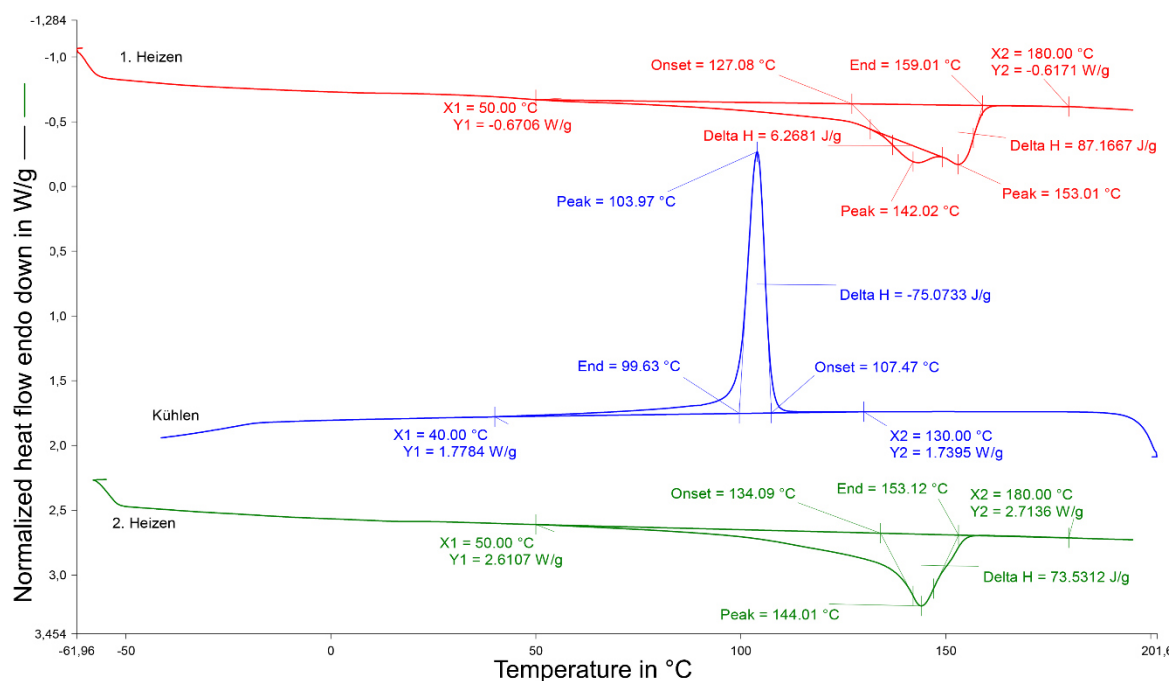


Figure 3.11: DSC result of an untreated PP sample.

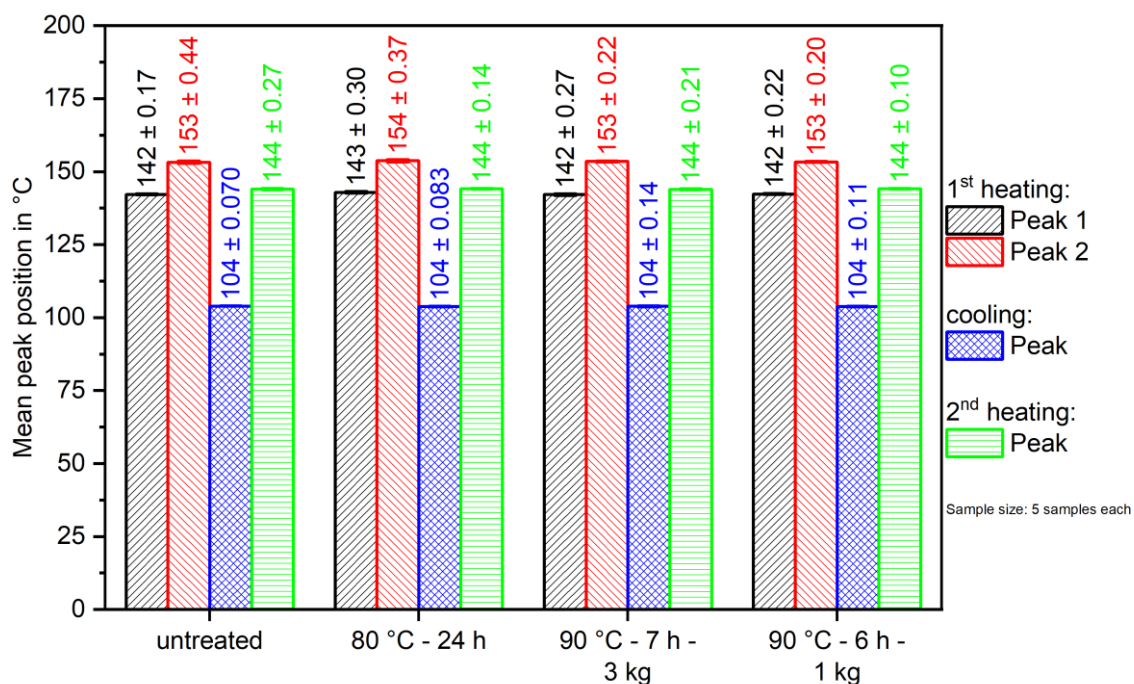


Figure 3.12: Positions of the characteristic peaks measured by DSC.

3.2.2.2 Milling

In addition to the warped specimens, the PP-VS-structures showed strong warping especially on the top and bottom compression surfaces. A heat treatment was not feasible due to the risk of deforming the lattice structure. However, the warped compression faces would lead to problems during the compression tests. Therefore, the compression faces were machined flat on a milling machine prior to testing. Figure 3.13 (a) shows a structure with deformed surfaces. The milling setup to machine the top and bottom surfaces is shown in Figure 3.13 (b). The structures were clamped on the milling machine using a vacuum table and metal brackets. The toolhead was equipped with indexable tips with a special cutting-edge geometry for soft materials. Due to the vacuum clamping device the unit cell structure was not harmed resulting in a significant improvement of the flatness of the VS-structures and consequently in an increase of the quality of the compression tests.

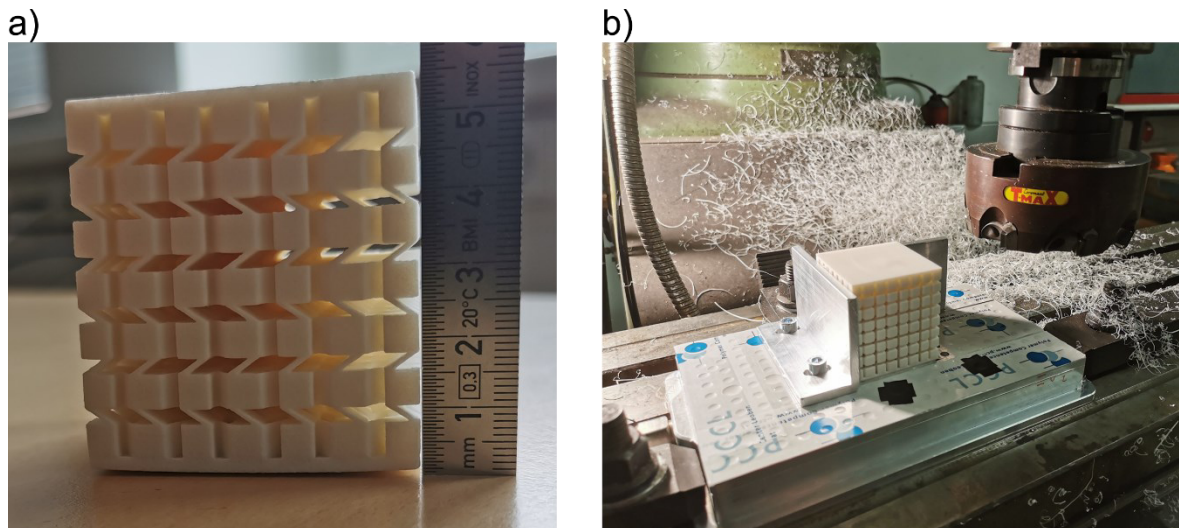


Figure 3.13: a) PP-VS-structure B and b) milling setup for machining the top and bottom faces.

3.2.3 Unwarping of TPP

After the TPP standard specimens (3PB/ Charpy and tensile test) arrived from the manufacturer, warpage was observed. Figure 3.14 shows an example of a warped TPP tensile specimen.



Figure 3.14: Warped specimens after delivery of a TPP.

The manufacturer concluded that the curing phase was the cause of the warping. The curing of the printed parts was done in an oven without any additional devices fixing the specimens. An increase of residual stress was suspected by the supplier causing the deformation. According to the experience of the company partner an additional annealing step was recommended. For that, the specimens were placed on a grating in the cold oven. The oven was heated up with 6.5 K/min until 150 °C was reached and kept constant for 10 minutes. Afterwards the oven was turned off and the specimens cooled down in the closed oven chamber until room temperature was reached. In contrast to the annealing procedure of the PP specimens (see section 3.2.2), no additional load was required for the annealing of the TPP samples.

3.2.4 Unpacking TPP VS-structures

As previously described in section 3.1, TPP is a 3D printable thermoset. The underlying two step production process results in a significant increase of mechanical properties after curing (brown part) when compared to the green part. Due to the high complexity of the VS-structures, the company partner Tiger had severe problems in removing the residual powder in the cavities of the structures after the shaping step. To determine possible solutions for unpacking the VS-structures the structures were delivered directly after shaping with the residual powder in the cavities. Due the chemical reactivity of the uncured material special care had to be taken. For this purpose, an air blow chamber was built, shown in Figure 3.15, to test the unpacking of the VS-structures.

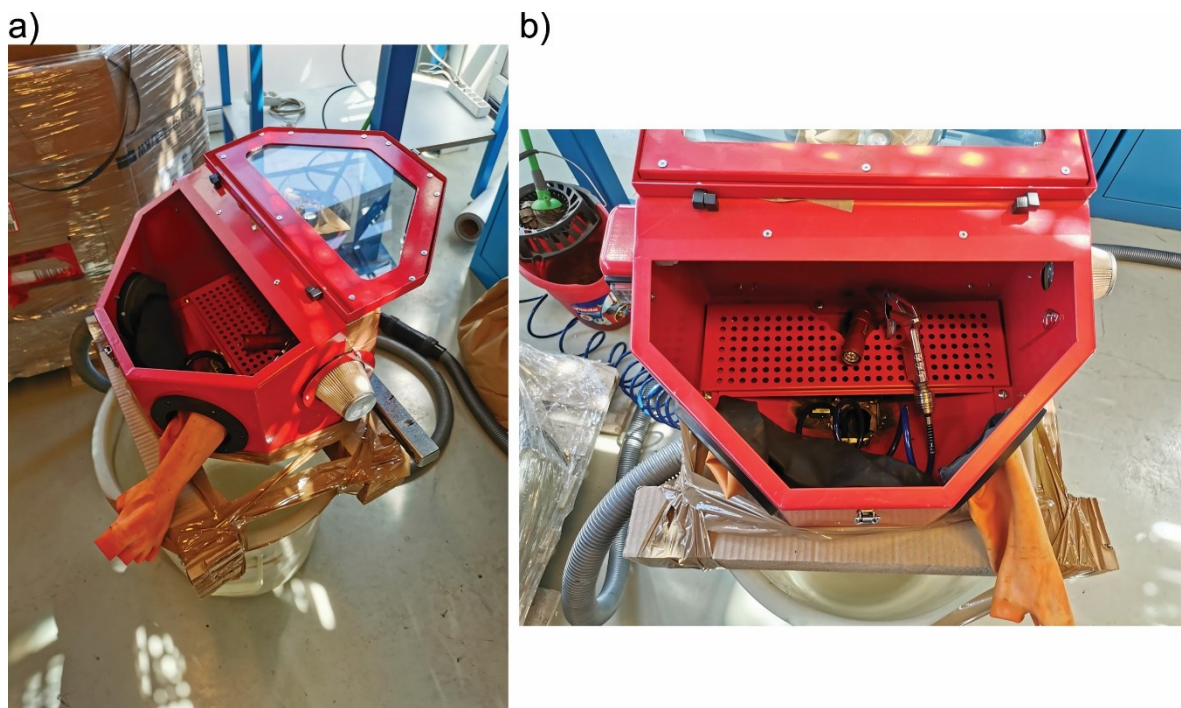


Figure 3.15: Air blow chamber to unpack the TPP-VS-structure from residual powder. a) Overview and b) detailed top view.

Figure 3.16 shows different VS-structures after unpacking. Especially in the corner areas of the structures, parts of the lattice structure broke off. Even after several tries, no solution was found to unpack the VS-structures without damaging the parts. Because of the problems during unpacking, no compression tests could be performed. Consequently, no final comparisons between compression tests and FEM simulations can be made. The

material data (Charpy impact, tensile, 3PB and DMA) obtained within this study was submitted to the company partner but will not be presented in more detail here.

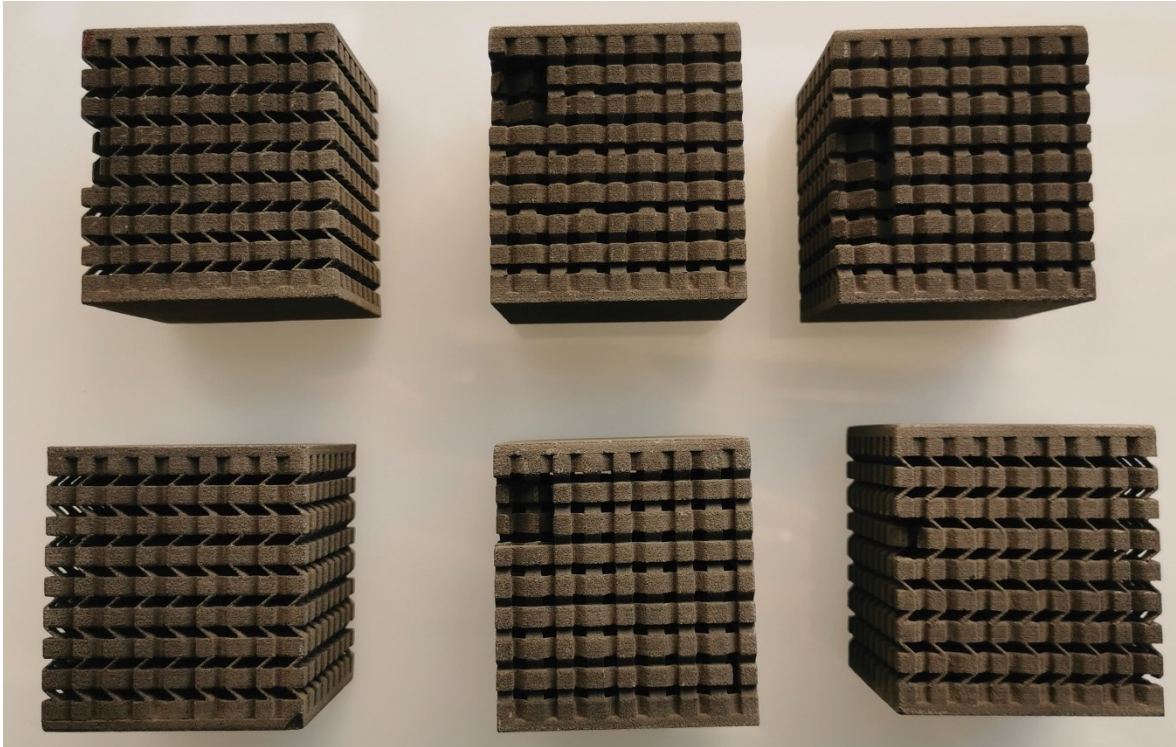


Figure 3.16: TPP-VS-structures after unpacking from the residual powder.

3.3 Dynamic Mechanic Analysis

To investigate the thermomechanical properties of the materials, dynamic mechanical analyses (DMA) were performed. For this, two specimens (printed in horizontal orientation, see Figure 3.2 c) of each material were tested with a dynamic tensile load. The measurements were performed with a 12 N DMA “DMA/SDTA861e” (Mettler Toledo, USA), shown in Figure 3.17. The temperature range was set to $-60\text{ }^{\circ}\text{C} - 120\text{ }^{\circ}\text{C}$. A heating rate of 3 K/min was used for all specimens. The test frequency was set to 1 Hz with a maximum force and displacement of 8 N and $3\text{ }\mu\text{m}$, respectively. The main test parameters are summarized in Table 3.8.



Figure 3.17: 12 N DMA “DMA/SDTA861^e” from Mettler Toledo, USA.

Table 3.8: DMA test parameters.

Repetitions	2 for each material
Start temperature	-60 °C
End temperature	120 °C
Heating rate	3 K/min
Max. Force	8 N
Max. displacement	3 μm
Offset	200 %
Frequency	1 Hz

3.4 Impact tests

To characterize the toughness of polymers, impact tests can be performed [22]. The Charpy impact test is commonly used with either notched or unnotched specimens [22]. The

Charpy impact tests were performed according to EN ISO 179-1:2010 [23] on a “CEAST Resil 25” (Compagnia Europea Apparecchi Scientifici Torino, Italy) at three different temperatures: $-30\text{ }^{\circ}\text{C}$, $0\text{ }^{\circ}\text{C}$ and room temperature ($23\text{ }^{\circ}\text{C}$). The specimens for the $0\text{ }^{\circ}\text{C}$ and $-30\text{ }^{\circ}\text{C}$ measurements were cooled down using the attached tempering chamber with liquid nitrogen. After filling the chamber with the specimens, the temperature control was turned on and a holding time of 60 minutes was chosen before the start of the impact tests. For each material and temperature, ten measurements with unnotched specimens were performed. The impact energy of the hammer was 2 J. Figure 3.18 shows the test setup for the impact tests. The dimensions of the tested specimens were measured using a digital caliper. The evaluation was done, according to the equations in section 2.3.1.



Figure 3.18: Charpy impact test setup.

3.5 Tensile tests

The tensile test is the basic test for quasi-static material characterization [22]. Furthermore, the tensile test data was used to generate an elastic-plastic material model of each tested material. The tensile tests were done according to EN ISO 527-2:1996 [27] on a universal

testing machine “Zwick Z250” (ZwickRoell GmbH & Co. KG, Germany). In addition, the Digital Image Correlation system (DIC) “Aramis 4M” (GOM GmbH, Germany) was used for the strain measurements. For the DIC system, each specimen had to be prepared with a spray pattern consisting of a white foundation using “NORD-TEST Entwickler U 89 Spray” (HELLING GmbH, Germany) and fine black spray dots using “Kontakt Chemie GRAPHIT 33” (CRC Industries Europe BVBA, Belgium). First the specimens were sprayed with a thin layer of the white foundation to avoid reflections of the surrounding light sources. Next, an even distribution of small black dots was applied. The goal was to create reference points for the DIC system. The longitudinal and transversal strain is calculated according to the movement of each point compared to the starting position. A calibration was done before each test series/condition with a calibration cube. Ten measurements for each material and temperature were performed. A force transducer with a limit of 10 kN was used. To avoid clamping issues, especially while testing at -30 °C, mechanical clamps were used. These clamps were tightened with 20 Nm using a torque wrench. The test speed was kept constant at 1 mm/min to avoid the influence of strain-rate dependency (as described in section 2.3.2.1) and improve the material modeling process. The tempering chamber was cooled down using liquid nitrogen. First, the specimens were sprayed with a suitable spray pattern (fine black dots required for the DIC measurement). Afterwards, the specimens for the 0 °C and -30 °C measurements were precooled in the chamber while cooling down to their respective temperature. After clamping each specimen and closing the chamber, an additional cooling time started. The cooling time for the 0 °C and -30 °C specimens were chosen to be 10 minutes and 20 minutes, respectively. During this time the automatic force control was active to keep the force at zero and to compensate dimensional changes while cooling. After awaiting the cooling time, the test was started. The room temperature specimens were kept at lab conditions. The start procedure was analogous to the low temperature test. The test ended at break (80 % of F_{max} ; standard parameter of the test software). Table 3.9 summarizes the test settings. The dimensions of the specimens were measured using a digital caliper. Figure 3.19 shows the test setup for the tensile tests with the DIC systems and the closed tempering chamber and a detailed view of the mechanical clamps with the specimen and the spray pattern. The evaluation of the engineering stress – strain was done using the method and equations described in section 2.3.2.1.

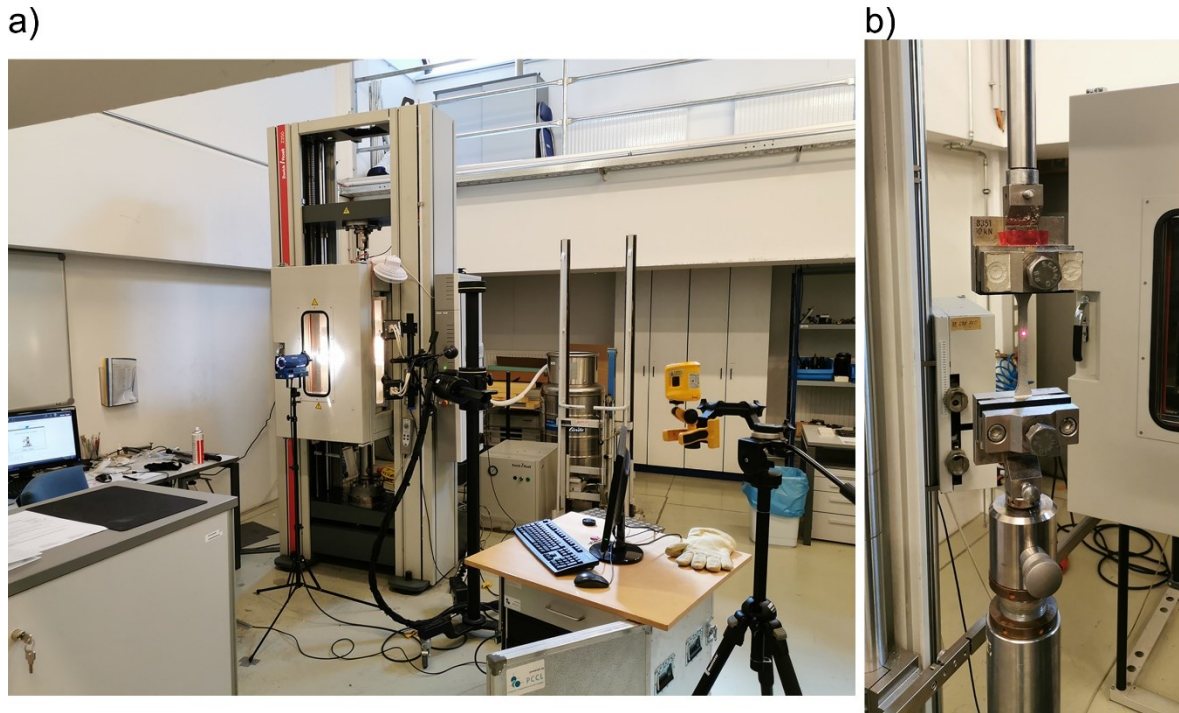


Figure 3.19: a) Universal testing machine with DIC system and b) detailed view of the mechanical clamps with specimen and spray pattern.

Table 3.9: Test settings of the tensile measurements.

Repetitions	10 for each material and temperature
Constant test speed	1 mm/min \pm 1 %/min
Force transducer	10 kN
Strain measurement	DIC system
Starting length	115 mm
Cooling time	0 °C: >10 min -30 °C: >20 min
Test end	Break (80 % of Fmax)

3.6 Three-point-bending tests

The bending load is one of the most frequently occurring load situation in modern engineering [22]. Especially the struts of the VS-structures are typical examples for bending loaded sub-elements of mechanical metamaterials. The bending test data was used to create elastic-plastic material models and were compared to their respective material model based on tensile tests. The three-point-bending (3PB) tests were performed according to EN ISO 178:2010 [31] on the universal testing machine described in

section 3.5. Figure 3.20 shows the bending setup, mounted in the testing machine while testing. The anvil span distance was 64 mm and the radii of both the upper anvil and the two fixed flexural anvils was 5 mm. Table 3.10 shows the 3PB test parameters.

The test speed was kept constant at 2 mm/min \pm 1%/min to improve the material modeling process (see section 2.3.2.1). All specimens were placed in the chamber while cooling down the chamber for precooling. After placing the specimen on the bending rig, the chamber was closed and an additional cooling time (10 minutes for 0 °C and 15 minutes for -30 °C) was awaited. After cooling the specimens down to the goal temperature, a preload of 0.1 MPa was applied. The preload was used to reduce wobbling of deformed specimens. After reaching the preload, the test started automatically. The room temperature specimens were kept in lab conditions. The preload and start procedure were analogous to the low temperature tests. The tests ended after break detection (force drop of 80 % of F_{max}) or after reaching a maximum bending strain of 15 %, whichever came first. The dimensions of the tested specimens were measured, before testing, using a digital caliper. The standard equations for calculating the main results for the 3PB are described in section 2.3.2.2.

Table 3.10: Test settings of the 3PB measurements.

Repetitions	10 for each material and temperature
Constant test speed	2 mm/min \pm 1%/min
Force transducer	10 kN; 500 N (PP only)
Strain measurement	Macro lever
Anvil span L_{span}	64 mm
$R_1 = R_2$	5 mm
Preload	0.1 MPa
Cooling time	0 °C: >10 min -30 °C: >15 min
Test end	Break (80 % of F_{max}) Bending strain \geq 15 %



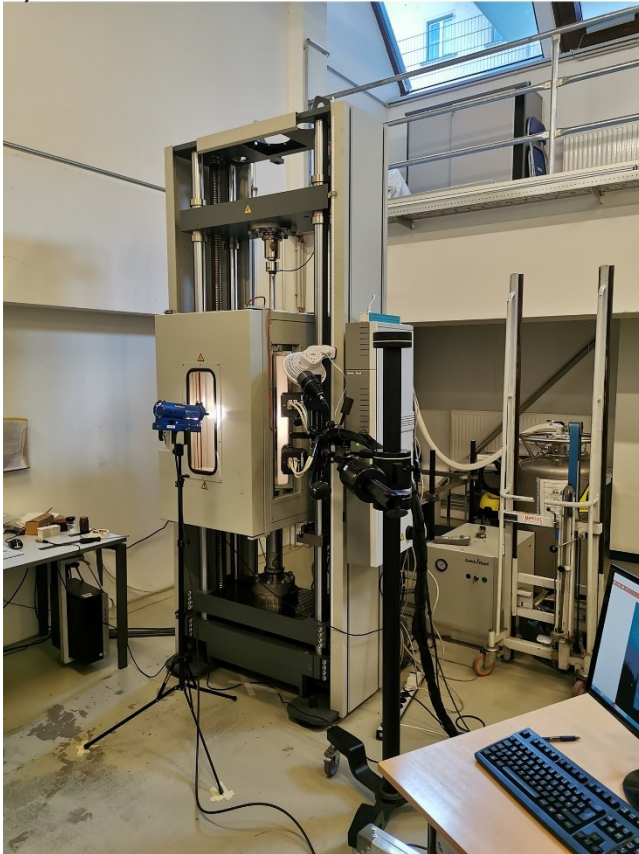
Figure 3.20: 3PB setup while testing.

3.7 Compression tests

In general, compression tests are used to characterize compressive behavior of polymers under uniaxial loading [22]. Especially within this study, the compression tests were performed to investigate the behavior of a mechanical metamaterial designed for compression applications. The VS-structure is defined by its tunable compression modulus by changing the geometric parameters of the unit cells [7]. Currently, there are no standards for the mechanical testing of metamaterials. However, for the analysis of the compression tests of the VS-structure, the standard as defined in EN ISO 604:2003 [33] was followed where possible. The tests were carried out using the same universal testing machine as described in section 3.5. In addition, the DIC system as described in section 3.5 was used as well. Figure 3.21 shows the compression test setup with the DIC system and a VS-structure with applied spray pattern. Table 3.11 lists the test parameters for the compression tests. The test was carried out with two parallel steel compression plates with diameters of 90 mm and a force transducer with maximum force of 10 kN. The temperature

chamber was cooled down with liquid nitrogen. Before testing, the structures were sprayed with a fine black spray pattern (see section 3.5). The contact areas of the compression plates were lubricated with a temperature resistant grease “BARRIERTA L 55/2” (Klüber Lubrication München GmbH & Co. KG, Germany). For the tests at low temperatures (0 °C and -30 °C) the cooling time (10 minutes for 0 °C and 20 minutes for -30 °C) was awaited before the preload was applied. After reaching a preload of 3N, the measurement was started. The test ended after break detection (force drop of 80 % of F_{max}) or after reaching a maximum bending strain of 15 %, whichever came first. The dimensions of the tested specimens were measured, before testing, using a digital caliper. The geometric parameters of the VS-structure were measured before testing using an optic microscope (see section 3.1.2.2).

a)



b)

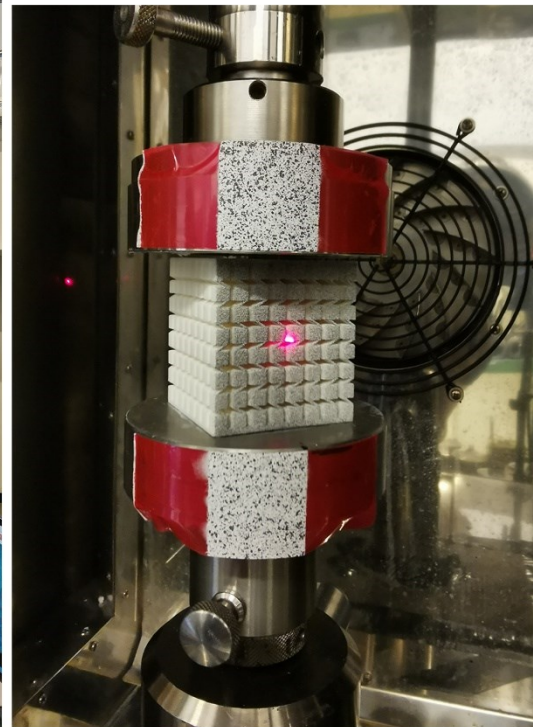


Figure 3.21: a) Compression test setup and b) detailed view of the VS-structure before testing with reference spray pattern on the compression plates.

Table 3.11: Test parameters for the compression tests.

Repetitions	5 for each structure, material, and temperature
Constant test speed	1 mm/min
Preload	3 N
Speed until preload	1 mm/min
Force transducer	10 kN
Cooling time	0 °C: >10 min -30 °C: >20 min
Test end	Break (80 % of Fmax) Bending strain ≥ 15 %
Lubed compression plates before each test	

3.8 Finite Element simulations

The key goal of this study is to compare different material modeling approaches for the simulation of the VS-structure. For this reason, a significant effort was put into the material modeling and structural simulations of VS-structures. Each of the following FEM simulations were performed using “Abaqus FEA 2019” (Abaqus). For evaluation purposes, several python [51] scripts were created.

3.8.1 Material modeling

To improve the FEM simulations and create a better representation of the nonlinear deformation behavior of the VS-structure (see section 2.4.1), elastic-plastic material models for each material and temperature were created. In addition, the difference between material models based on tensile and 3PB tests was analyzed.

To reduce the modeling effort, mean test curves were calculated before the initial modeling steps started. For this, measurements with a maximum stress less than 50 % of the maximum stress of the series were removed before calculating the mean curves. Beyond that, some outliers were sorted out due to very low deflections or because the test data showed a different appearance, caused by slipping, necking or other defects, compared to the general trend of the measurement. The goal was to only use comparable curves to reduce problems while optimizing the material model. For averaging the test data, a linear

interpolation between each single data point was needed to calculate the mean value. To scale the data accordingly, 1000 points were set in the averaging algorithm. Although, experience has shown that importing too many data points into a material model in Abaqus can lead to problems and simulation abortions. Therefore, only 50 points spread with a logarithmic interpolation were used as input data for the Abaqus material model. Table 3.12 lists all generated material models within this study for each material. In total 24 material models were created for PA12 and PP within this study.

Table 3.12: Generated material models for each material.

No.	Print orientation	Temperature in °C	Material model
1	horizontal	-30	Tensile based
2		-30	3PB based
3		0	Tensile based
4		0	3PB based
5		23	Tensile based
6		23	3PB based
7	vertical	-30	Tensile based
8		-30	3PB based
9		0	Tensile based
10		0	3PB based
11		23	Tensile based
12		23	3PB based

3.8.1.1 Tensile based material modeling

The Abaqus material model consists of an elastic part with Young's modulus and Poisson's ratio and the plastic part. For the tensile data set, the plastic part was defined by the yield stress – plastic strain curve. This requires tensile tests with a constant test speed due to the strain-rate dependency of polymers (see Figure 2.10). To increase the accuracy, longitudinal and transversal expansion measurements are required to obtain the Poisson's ratio, which is needed for the calculation of the yield stress – plastic strain data (see section 2.4.1.1). The evaluation was done by performing the steps described in section 2.4.1.1 on mean curves (see section 3.8.1) of each material and temperature.

3.8.1.2 3PB based material modeling

Due to the nonlinear behavior of the 3PB test, a reverse engineering approach is required for developing an elastic-plastic material model based on this kind of mechanical test [7]. For this purpose, an iterative parameter-optimization process was set up, based on bending force and deflection data, given by the mechanical tests, and FEM simulations [7]. Figure 3.22 shows the flow chart describing the reverse engineering process.

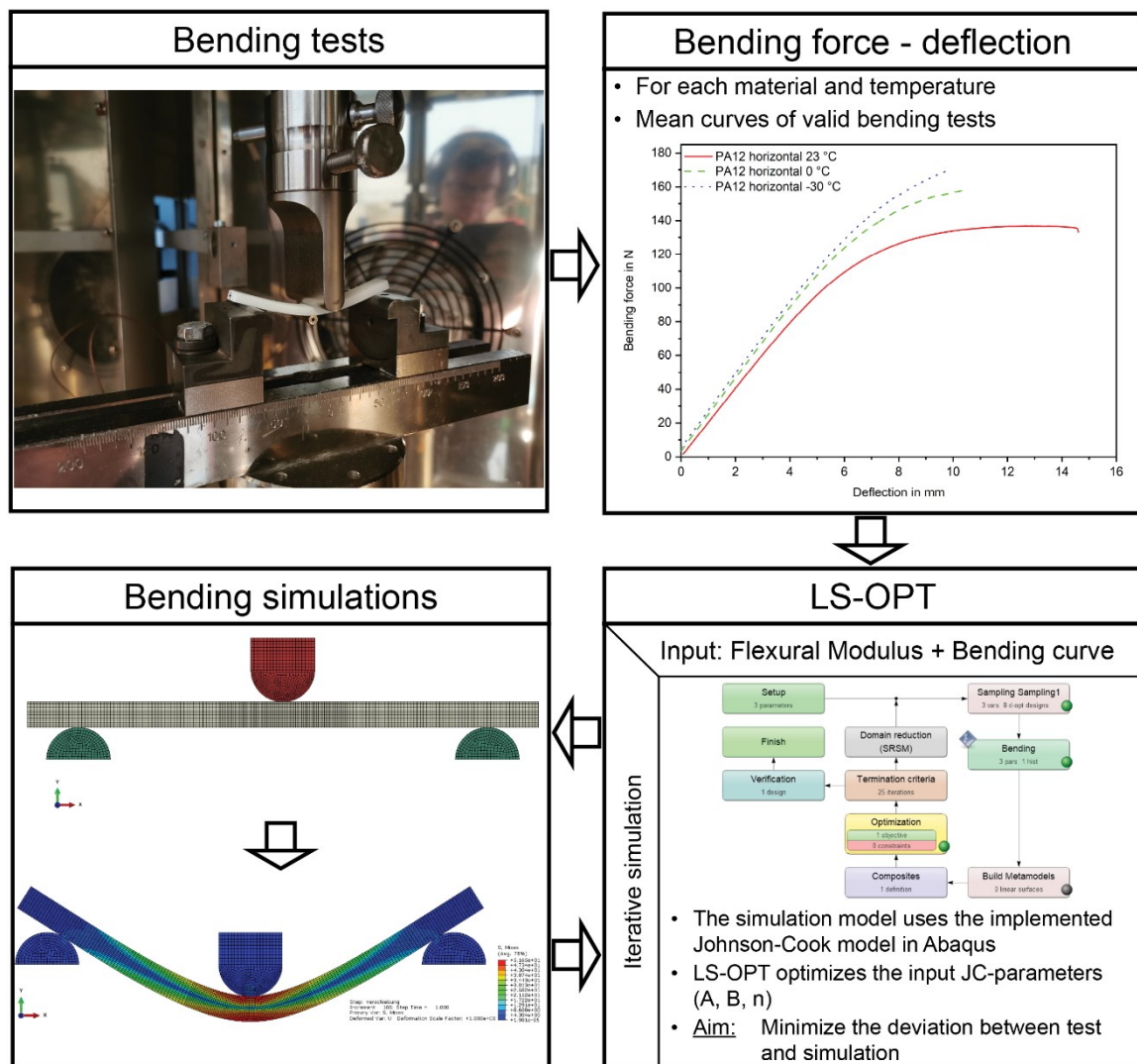


Figure 3.22: 3PB-reverse engineering approach for material optimization.

First the bending tests were performed as described in section 3.6. Next, mean curves of the tested data according to section 3.8.1 were calculated. The third step was to set up the parameter optimization system. For this, the parameter optimization program “LS-OPT” (DYNAmore GmbH, Germany) in combination with Abaqus was used. In Abaqus an

idealized 3PB test was set up. The simulation model uses the Johnson-Cook strain hardening model as described in section 2.4.1.2. The simulations were performed with constant temperature. As a result, the temperature dependency term was not considered. Beyond that, the strain-rate dependency was not considered as well in the Johnson-Cook model. Taking these simplifications into account, Eq. 3.1 shows the simplified Johnson-Cook equation for the yield stress applied in the Abaqus models.

$$\sigma_{yield} = [A + B \cdot \varepsilon_{plastic}^n] \quad (3.1)$$

LS-OPT was then used to optimize these parameters, by minimizing the deviation between the tested force – deflection curve and the resulting curve from the simulation. This was done in multiple iterations. The limits of the optimized parameters had to be set in the software in advance, the algorithm is then changing the limits to reduce the needed iterations. Pretests showed that the parameter A (which refers to the onset of yielding) is not allowed to take values less than 1, or the Abaqus simulation is aborted. Therefore, the minimum limit for A was set to 1 for all material models. To increase the quality of the optimization, two optimization runs were performed. A maximum of 25 iterations was chosen to optimize the Johnson-Cook parameters in the first run. The parameters from the first run were taken as input parameters for the second optimization run. The optimization only affects the plastic part of the material model in Abaqus. For the simulations based on 3PB data the flexural modulus (obtained from the mechanical tests) was used as the stiffness parameter for the elastic part of the material model. For the Poisson's ratio the measured values from the tensile tests were considered.

Figure 3.23 shows the meshed FEM model of the 3PB simulation. The model consists of four parts: the specimen, the upper anvil and the two counter parts of the flexural fixture anvil. For the contact condition, friction between the metal parts and the specimen was considered. The friction coefficient was chosen according to reference values from literature and set for PA12 $\mu=0.3$, PP $\mu=0.35$ [52 - 56]. The model was built up with 2D elements (plane strain elements), the width and thickness were adjusted according to the mean dimensions of the tested specimens. The global seed size for the specimen was set to 0.5 mm with a local seed size in the middle section of 0.25 mm. The element type of the specimens was set to be an 8-node biquadratic element with reduced integration (CPE8R).

The seed size of the anvil and fin was set to 0.5 mm with 4-node bilinear elements and reduced integration with hourglassing control (CPE4R) [57]. The material model consists of the elastic part, with the flexural modulus and the Poisson's ratio, and the plastic part. In the plastic part the Johnson-Cook hardening model was used with the parameters according to Eq. 3.1. The model was calculated using the standard implicit solver of Abaqus. The reaction force in N and the deflection in mm in y-direction was exported automatically from the simulation using a python script. These results were then loaded into LS-OPT during each iteration.

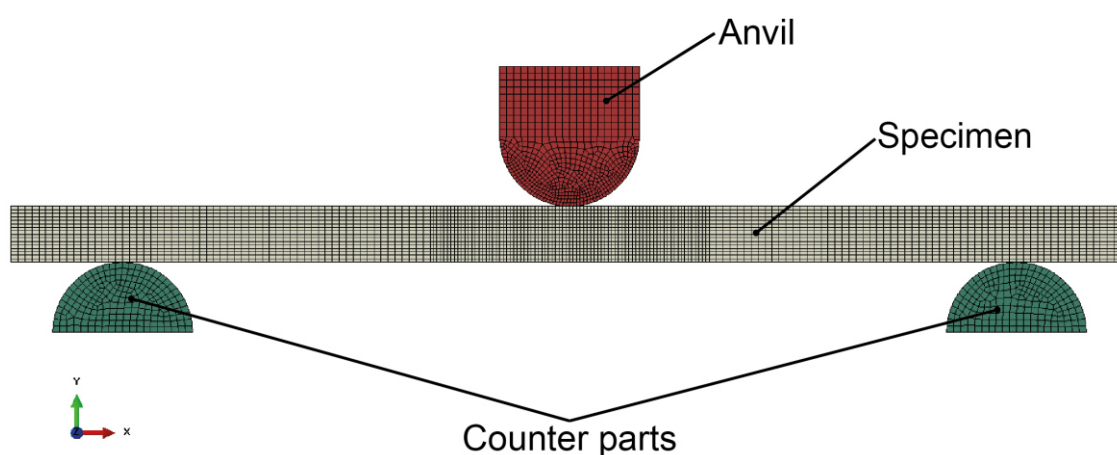


Figure 3.23: Simulation model for 3PB simulations (meshed parts).

3.8.2 Compression simulations

As already mentioned, the compression simulations and the final evaluation of the simulation results were performed using Abaqus in combination with in-house developed python scripts. The bending struts were separated from the rest of the structure to be able to generate a finer mesh in the struts since the main deformation when compressed occurs in the struts. The separation was done by partitioning the struts using datum planes. Only the struts in compression direction (in y-direction) were separated, as the struts perpendicular to the load direction do not affect the simulation results significantly. This simplification was made to reduce the total number of elements. Figure 3.24 shows the VS-structure in Abaqus with indicated partitions.

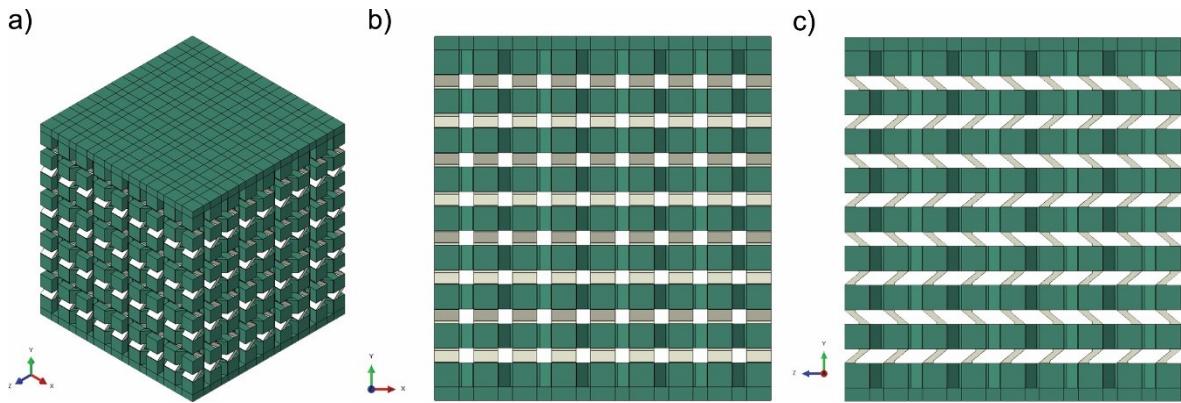


Figure 3.24: VS-structure in Abaqus with partitioned struts. a) 3D view, b) x-y view and c) z-y view (green = global mesh settings, grey = finer mesh for the struts).

The boundary conditions were modeled according to a simplified compression test. For the bottom surface the degree of freedom (DOF) in y-direction was locked, the other directions were free. The top surface was set to move by -1.6 mm in the y-direction, the other DOF remained free. The movement was applied to a reference point and coupled by equations (only in y-direction) to the entire top surface of the compression plate. The standard implicit solver of Abaqus was chosen to perform the simulation. Using a python script, the reaction force in N and the displacement in mm in y-direction were exported automatically. The nominal stress – strain behavior was calculated using the overall dimensions of the structure. The compression modulus was calculated in the strain range of 0.05% – 0.25%, similar to ISO 604 [33]. The general mesh element type for the VS-structure (green areas in Figure 3.24) were quadratic tetrahedral elements (C3D10) with a seed size of 1 mm. The mesh size of the struts was obtained by a mesh study as described in the next section.

3.8.3 Mesh test simulations

Before the final compression simulations were made, a mesh size study was performed. For this, the structure was seeded with the desired element sizes and afterwards the mesh was generated. The goal was to find the most efficient mesh size, meaning that the element size should be as small as possible for a sufficient simulation accuracy but big enough to keep simulation times low. Therefore, various mesh sizes were defined for the struts and the rest of the structure respectively. For the mesh test simulations, the VS-structure B was set up using the tensile material model of PA12 with horizontal and vertical orientation at 23 °C. The basic model and the modeling approach was kept the same as described in

section 3.8.2. The element size, element type and description of the simulated meshes for the struts (grey areas in Figure 3.24) are listed in Table 3.13.

Table 3.13: Element parameters for the struts in the VS-structure for the mesh test simulations.

Label	Seed size	Element type	Type reference
0.4 – tet	0.4 mm	Quadratic tetrahedral	C3D10
0.4 – hex	0.4 mm	Quadratic hexahedral	C3D20R
0.5 – tet	0.5 mm	Quadratic tetrahedral	C3D10
0.5 – hex	0.5 mm	Quadratic hexahedral	C3D20R
0.6 – tet	0.6 mm	Quadratic tetrahedral	C3D10
0.6 – hex	0.6 mm	Quadratic hexahedral	C3D20R
0.6 – hex – lin – tet	0.6 mm	Quadratic hexahedral	C3D20R
0.6 – hex – quad – full	0.6 mm	Quadratic hexahedral	C3D20

The general element type was kept the same for all simulations (as described in section 3.8.2) except for the simulations “0.6 – hex – lin – tet”, where the general element type was changed to C3D4 linear tetrahedral elements. Detailed descriptions of the element types according to the Abaqus manual [58] are listed in Table 3.14.

Table 3.14: Abaqus element type reference descriptions [58].

Type reference	Description
C3D4	4-node linear tetrahedron
C3D10	10-node quadratic tetrahedron
C3D20	20-node quadratic brick
C3D20R	20-node quadratic brick, reduced integration

Figure 3.25 shows the reaction force in y-direction as a function of the displacement in y-direction for the performed simulations. It was not possible to generate a mesh with 0.4 mm seed size with quadratic hexahedral elements (C3D20R). Therefore, they are not included in the study. Below a seed size of 0.5 mm the change in deformation behavior in comparison to the increase in simulation time is very small. In addition, it is known that tetrahedral elements are better for fitting complex shapes and react stiffer than hexahedral

elements with comparable element sizes [37]. Based on these results, a seed size of 0.5 mm with quadratic hexahedral elements (C3D20R) was chosen for the mesh of the struts.

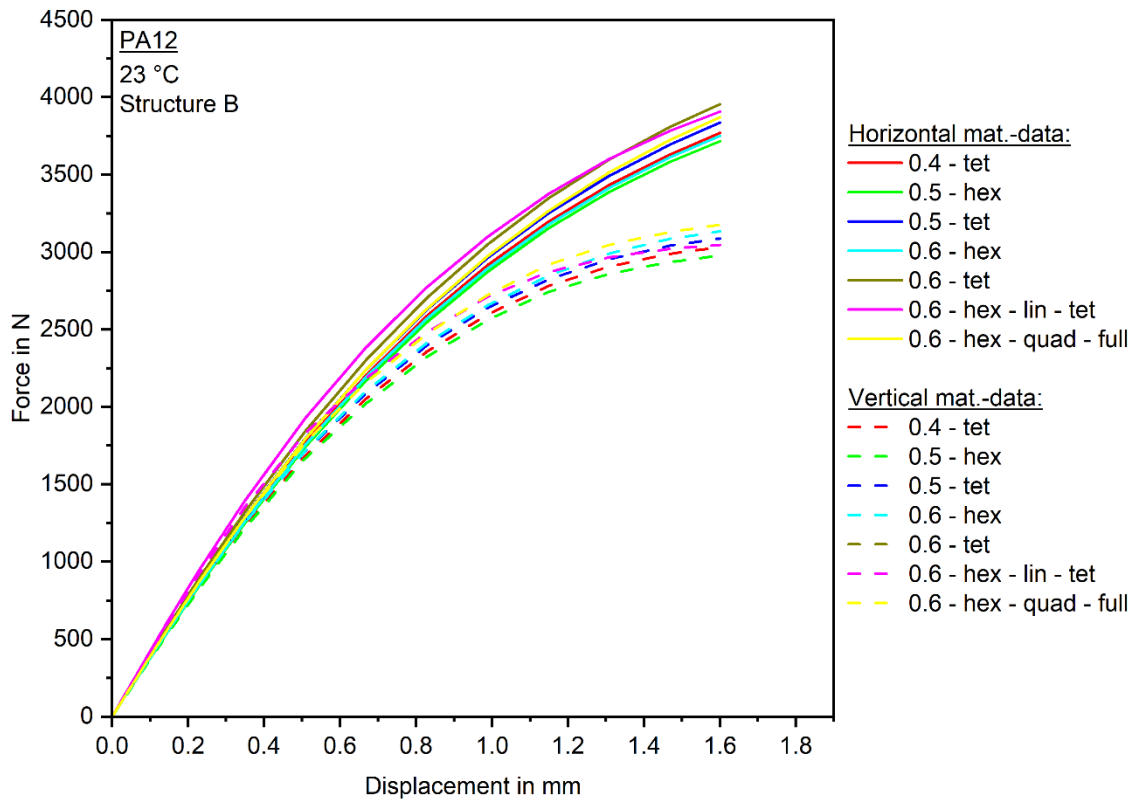


Figure 3.25: Mesh test simulation results with different seed sizes for PA12-VS-structure B with tensile based material models in horizontal and vertical direction at 23 °C.

4 RESULTS AND DISCUSSION

In this section, the results of the mechanical tests, as described in section 3, are presented. Based on the tensile and 3PB measurements, material models for the numerical simulations were generated to study the effect of different mechanical testing methods when applied to compression tests of metamaterials.

4.1 Polyamide 12

4.1.1 DMA results

The DMA measurements were performed according to the approach as described in section 3.3. Figure 4.1 shows the storage module E' and the mechanical loss factor $\tan(\delta)$ of the measured PA12 specimens.

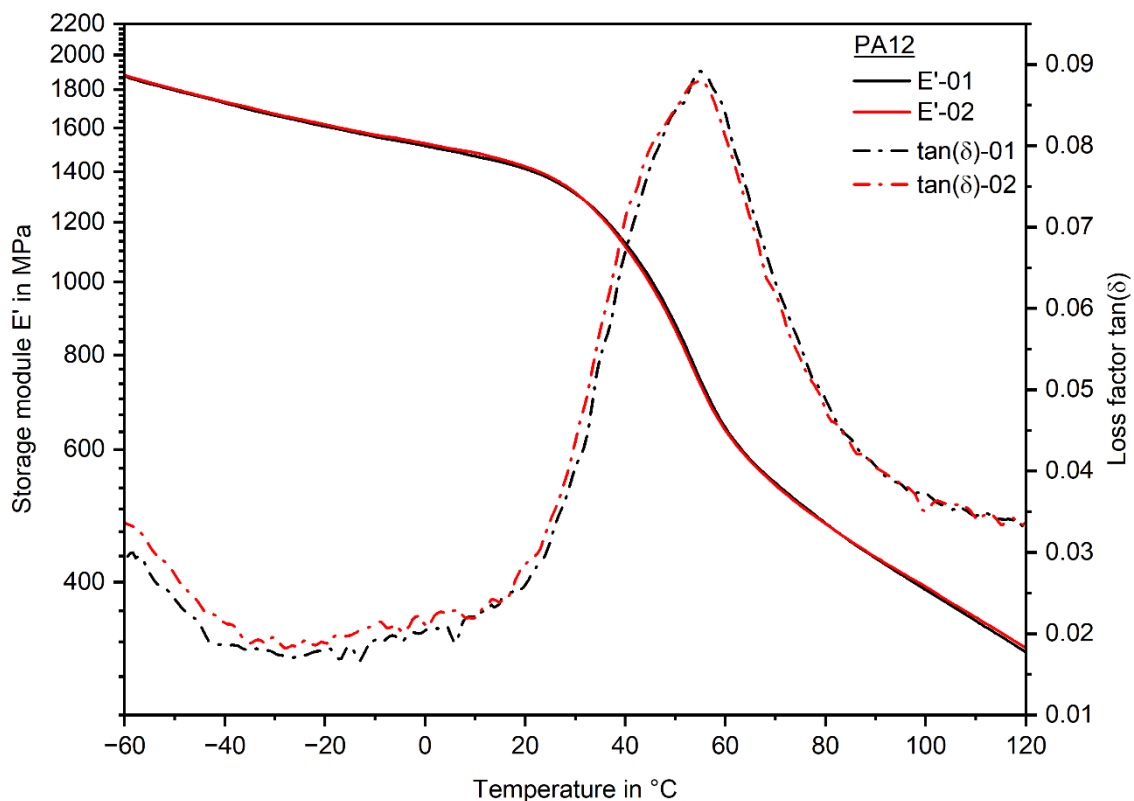


Figure 4.1: Storage module and loss factor of PA12.

The glass transition temperature was obtained from the peak of $\tan(\delta)$ and showed a value of $T_{g,PA12} = 55$ °C. According to Elsner et al. [30] and Hellerich et al. [26] the T_g for common

PA12 types is between 40 °C to 45 °C. However, these values are not specific to the material used in the additive manufacturing process by the supplier. Beyond that, Figure 4.1 shows a decrease of the storage modulus (from 1700 MPa to 1400 MPa) in the temperature range investigated in this study (between -30 °C to 23 °C). A significant decrease starts at 30 °C which is beyond the temperature range of the tested samples. As a result, no additional effects resulting from the transition between the energy-elastic and entropy-elastic state is expected.

4.1.2 Mechanical testing

To characterize the mechanical properties of the SLS printed PA12 under different load conditions, different mechanical tests were performed. Charpy tests were performed to determine the impact behavior, while tensile and 3PB tests were used to emulate different quasi-static load conditions. Beyond that, the tensile and 3PB test results served as input data for the material modeling process. These material models were then used to compare the compression tests of the VS-structures to numerical simulations.

4.1.2.1 Charpy impact tests

In contrast to the 3PB and tensile tests, the Charpy impact tests were not needed for FEM simulations. Details of the evaluation and experimental setup of the Charpy impact tests are described in section 2.3.1 and section 3.4, respectively. Figure 4.2 shows the mean Charpy impact strength values and their respective standard deviation for each temperature and orientation.

The measurements show that the mean impact strength is decreasing for increasing temperature (from 26.6 kJ/mm² to 22.6 kJ/mm² for horizontal and 12.2 kJ/mm² to 8.6 kJ/mm² for vertical print orientation). According to the literature, the impact strength should be increasing for increasing temperature [26, 28, 59, 60]. This characteristic stands in conflict with the mean test results shown in Figure 4.2 where the impact strength is decreasing for increasing temperature. A possible explanation could be that moisture was absorbed by the specimens (due to the hydrophilic behavior of PA12) during cooling. It is known that the impact strength is increasing for increasing moisture content for Polyamide [30]. Because of the holding time moisture from the air could have been absorbed by the

specimens resulting in an increase of the impact strength with decreasing temperature. However, due to the overlapping deviation margins no significant trend can be proven with this data. The results also show that the Charpy impact strength of the vertical specimens is more than 50 % lower compared to the horizontal ones. This finding can be explained by the difference in printing direction. For the Charpy tests, the impact hammer hits the vertical specimen directly in the intersection area of the different layer, which explains the lower impact strength compared to horizontal oriented specimens. The effect of decreased mechanical properties of vertical printed parts is well described in the literature and can be explained with the layer structure and a lack of adhesion between the layer of parts produced by additive manufacturing [61 - 63].

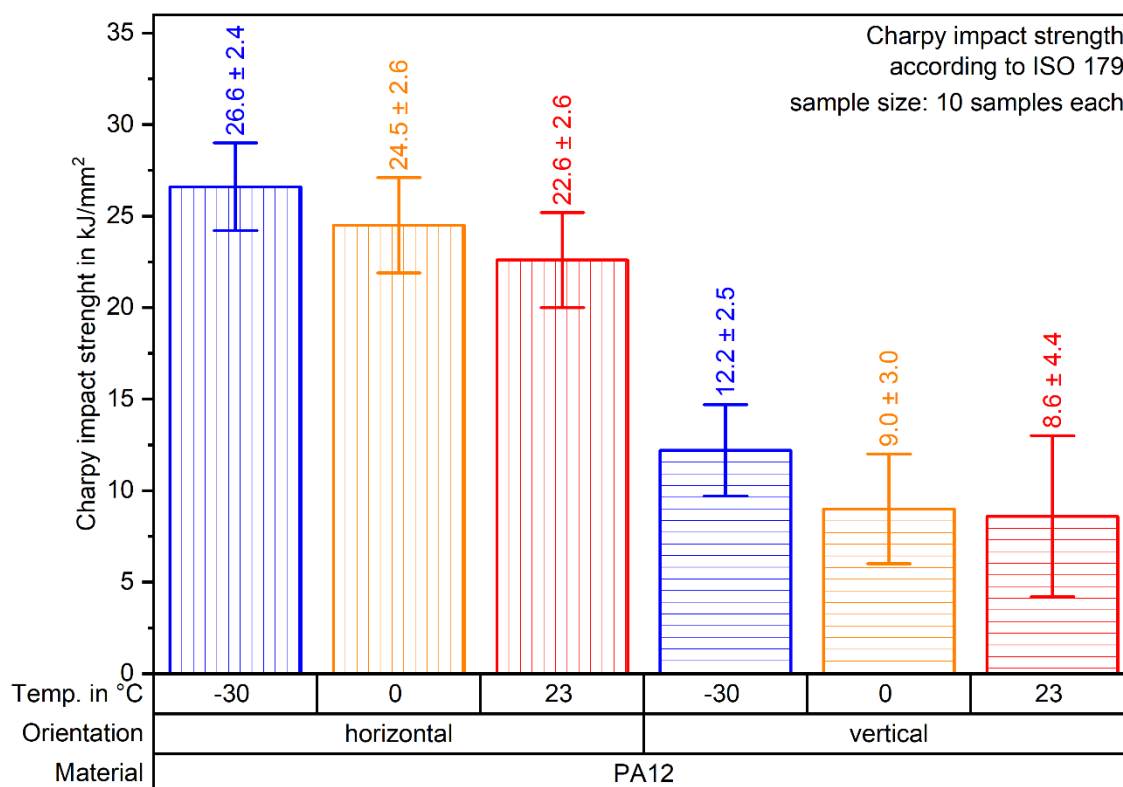


Figure 4.2: Mean Charpy impact strength and standard deviation of 10 specimens for each orientation and temperature of PA12.

4.1.2.2 Tensile tests

Details of the evaluation and experimental setup of the tensile tests are described in section 2.3.2.1 and section 3.5, respectively. Figure 4.4 shows the obtained engineering stress – strain curves for both orientations and three temperatures. In general, ten

specimens were tested for each configuration. However, due to errors of the DIC measurement, the data of one horizontal and one vertical 23 °C measurement was not usable and was therefore not included in this study.

Figure 4.4 a) and b) shows the mean tensile strength and the main strain at break of the specimens with their respective standard deviation, respectively. It can be observed that the tensile strength is decreasing with increasing temperature (from 57 MPa to 43 MPa for horizontal and 46 MPa to 29 MPa for vertical print direction). In contrast, the strain at break value is increasing with increasing temperature (from 4.8 % to 9.5 % for horizontal and 2.7 % to 3.3 % for vertical printed specimens). Although the observed strain at break for the vertically oriented specimens at 0 °C (2.1 %) is below the results of the -30 °C, the overlapping deviation margins do not allow for further conclusions. Figure 4.5 a) and b) shows the mean Young's moduli and mean Poisson's ratios, respectively. Similar to the tensile strength, the Young's modulus decreases with increasing temperature (from $2.1 \cdot 10^3$ MPa to $1.9 \cdot 10^3$ MPa for horizontal and from $2.2 \cdot 10^3$ MPa to $1.7 \cdot 10^3$ MPa for vertical print direction). However, almost no difference between the horizontal and vertical print direction is observed. On the other hand, the Poisson's ratio increases from 0.35 to 0.39 for horizontal and from 0.34 to 0.37 for vertical oriented specimens with increasing temperature. The temperature dependency of the tensile strength, strain at break, Young's modulus and Poisson's ratio fits very well to the expected behavior of polymers in general and is well documented in literature [24, 28, 64 - 67]. Additionally, it can be observed that the mechanical properties in vertical direction are significantly reduced, whereas the standard deviation is increased. This is commonly observed in additively manufactured specimens [61 - 63, 68]. This leads to the conclusion that the reproducibility of the SLS process is limited in vertical direction and special care must be taken when creating a material model for numerical analysis. The results of the tensile tests are summarized in Table 4.1.

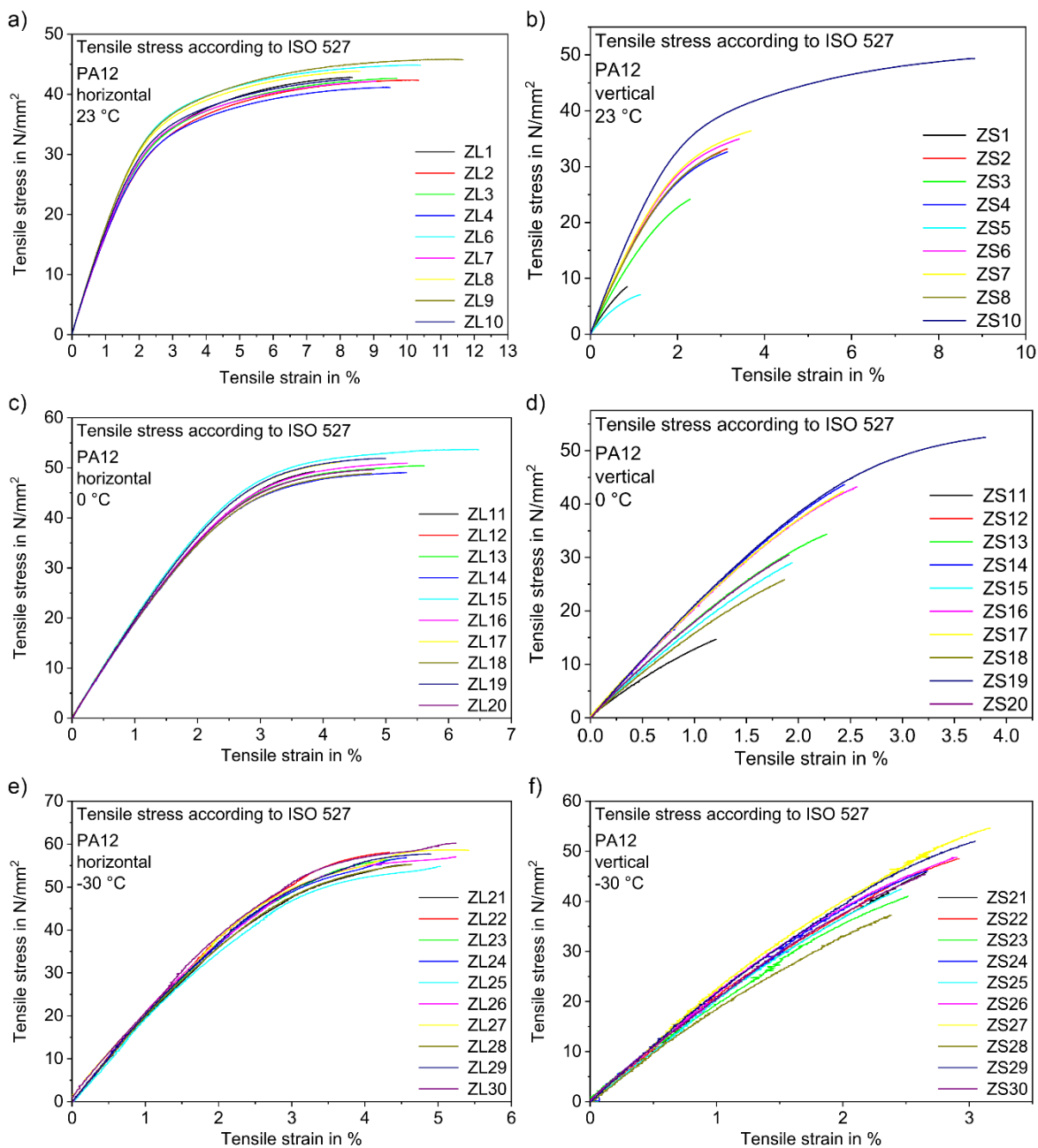


Figure 4.3: Tensile stress – strain curves of PA12 for a) horizontal at 23 °C, b) vertical at 23 °C, c) horizontal at 0 °C, d) vertical at 0 °C, e) horizontal at -30 °C and f) vertical at -30 °C.

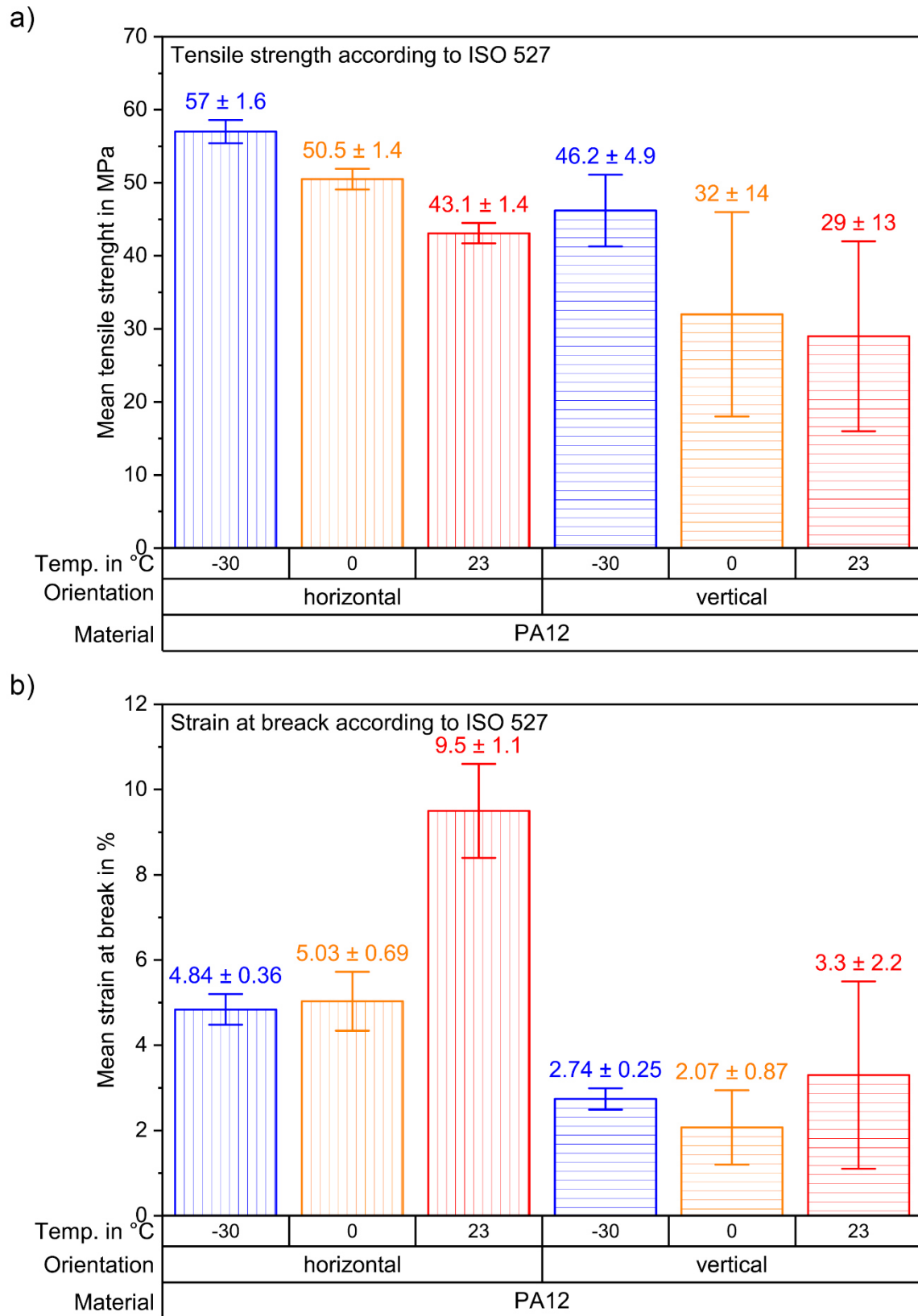


Figure 4.4: PA12 tensile test results. a) Mean tensile strength and b) mean strain at break.

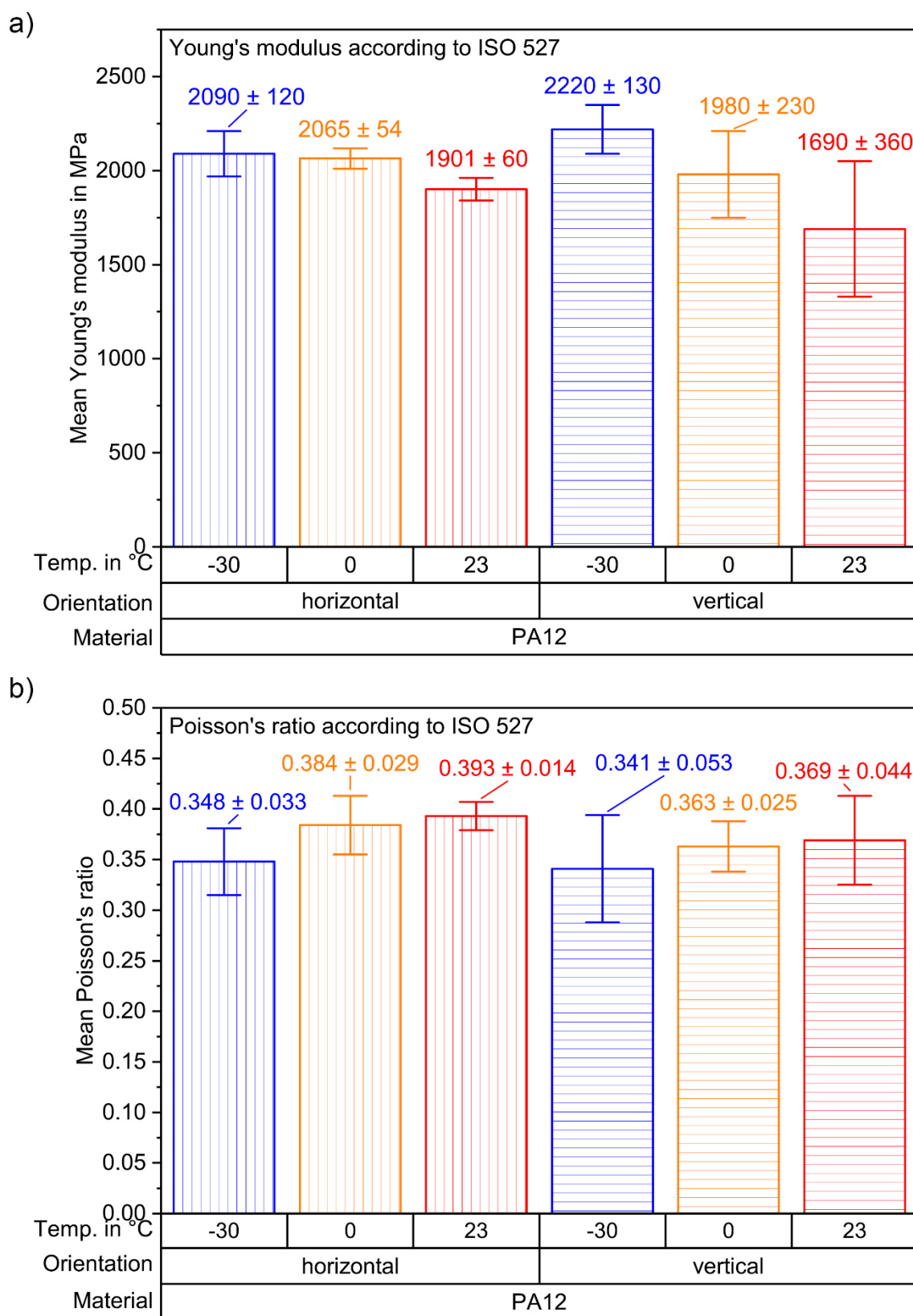


Figure 4.5: PA12 tensile test results. a) Mean Young's modulus and b) mean Poisson's ratio.

Table 4.1: Mean tensile test results for PA12.

Orient.	Temp.	Tensile strength	Strain at break	Young's modulus	Poisson's ratio
	in °C	in MPa	in %	in MPa	-
horizontal	-30	57.0 ± 1.6	4.84 ± 0.36	2090 ± 120	0.348 ± 0.033
	0	50.5 ± 1.4	5.03 ± 0.69	2065 ± 54	0.384 ± 0.029
	23	43.1 ± 1.4	9.5 ± 1.1	1901 ± 60	0.393 ± 0.014
vertical	-30	46.2 ± 4.9	2.74 ± 0.25	2220 ± 130	0.341 ± 0.053
	0	32 ± 14	2.07 ± 0.87	1980 ± 230	0.363 ± 0.025
	23	29 ± 13	3.3 ± 2.2	1690 ± 360	0.369 ± 0.044

4.1.2.3 3PB tests

Details of the evaluation and experimental setup of the 3PB tests are described in section 2.3.2.2 and section 3.6, respectively. Figure 4.6 shows the bending stress – strain curves for all test temperatures and print orientations of PA12. In general, ten 3PB specimens were tested, although two specimens of the vertical (tested with 0 °C) and one of the horizontal (tested with -30 °C) orientation broke right after applying the preload. They were not included in the evaluation.

Figure 4.7 a) and b) shows the mean flexural strength and strain at break of the specimens with their respective standard deviation, respectively. It can be observed that the flexural strength is decreasing for increasing temperature (from 95 MPa to 75 MPa for horizontal and from 62 MPa to 43 MPa for vertical print direction). The flexural modulus (see Figure 4.8) is decreasing for increasing temperature as well ($2 \cdot 10^3$ MPa to $1.8 \cdot 10^3$ MPa for the horizontal and from $1.7 \cdot 10^3$ MPa to $1.4 \cdot 10^3$ MPa for the vertical print direction). In contrast, the mean strain at break increases for increasing temperature (from 6.8 % to 10 % for the horizontal oriented specimens). These findings fit to the overall temperature behavior of polymers (see section 4.1.2.2). Although the strain at break data of the vertical oriented specimens shows an opposite trend, with a small decrease for increasing temperature (from 4 % to 3.8 %). However, due to the overlapping deviation margins, this trend cannot be proven in detail. The standard deviations of the vertically oriented specimens are significantly higher than the deviations of the horizontally oriented ones.

Analogous to the Young's modulus shown in section 4.1.2.2, the flexural modulus is decreasing for increasing temperature, which again fits the expected behavior [22, 28]. In general, the mean flexural modulus is lower for the vertical oriented specimens when compared to horizontal ones (similar to the tensile test results). The results of the 3PB measurements are summarized in Table 4.2.

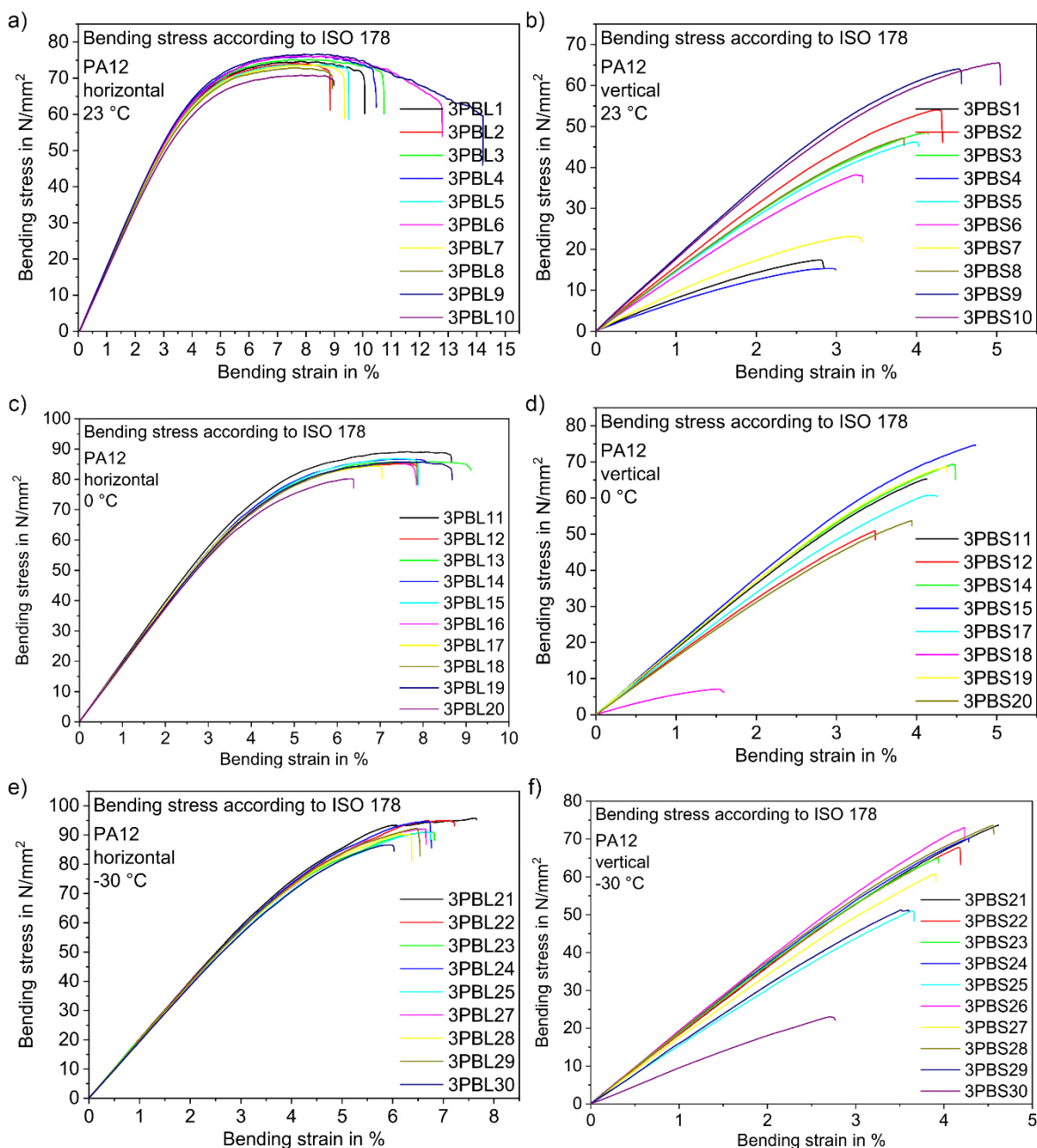


Figure 4.6: Bending stress – strain curves of PA12 for a) horizontal at 23 °C, b) vertical at 23 °C, c) horizontal at 0 °C, d) vertical at 0 °C, e) horizontal at -30 °C and f) vertical at -30 °C.

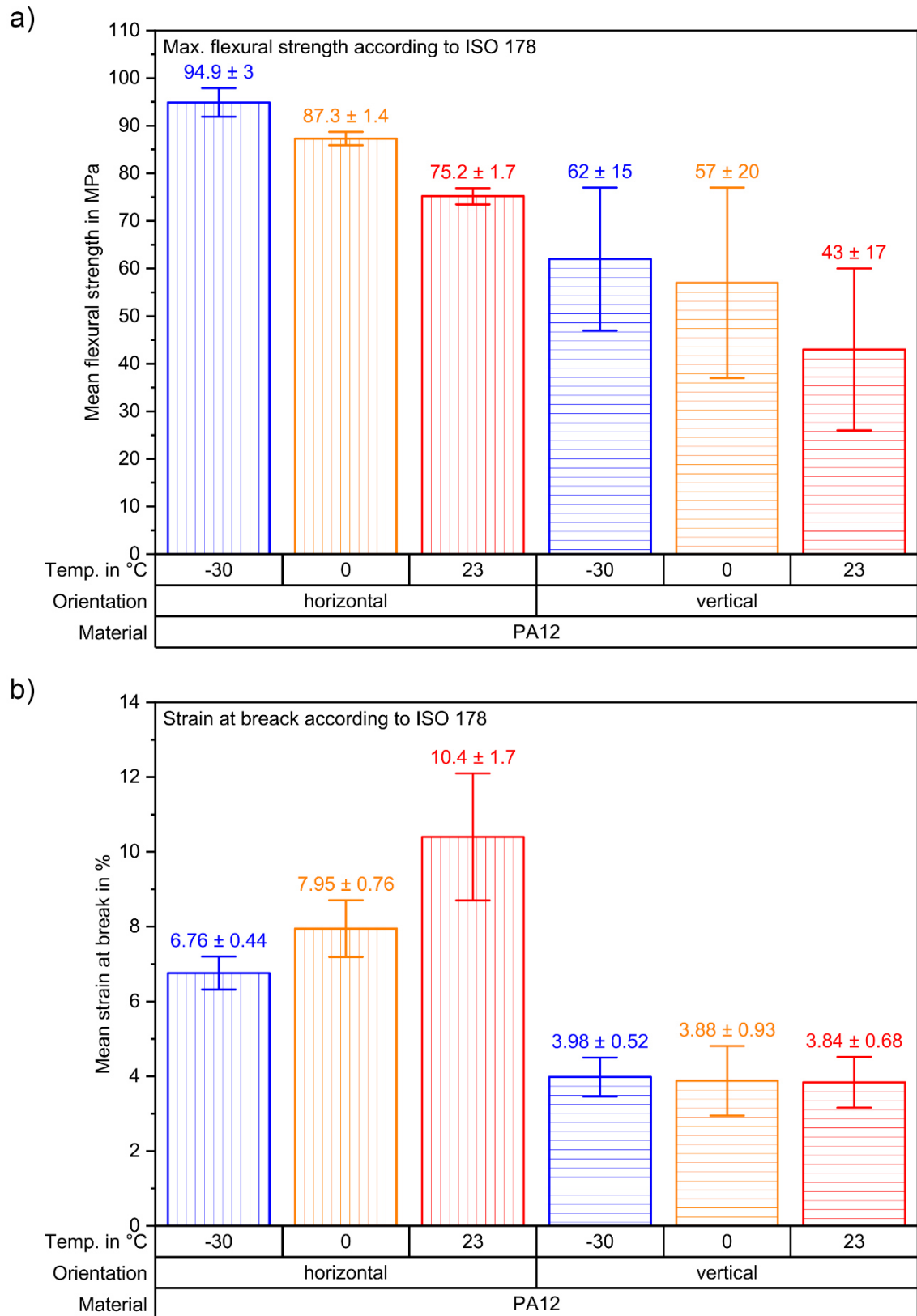


Figure 4.7: PA12 bending test results. a) Mean flexural strength and b) mean strain at break.

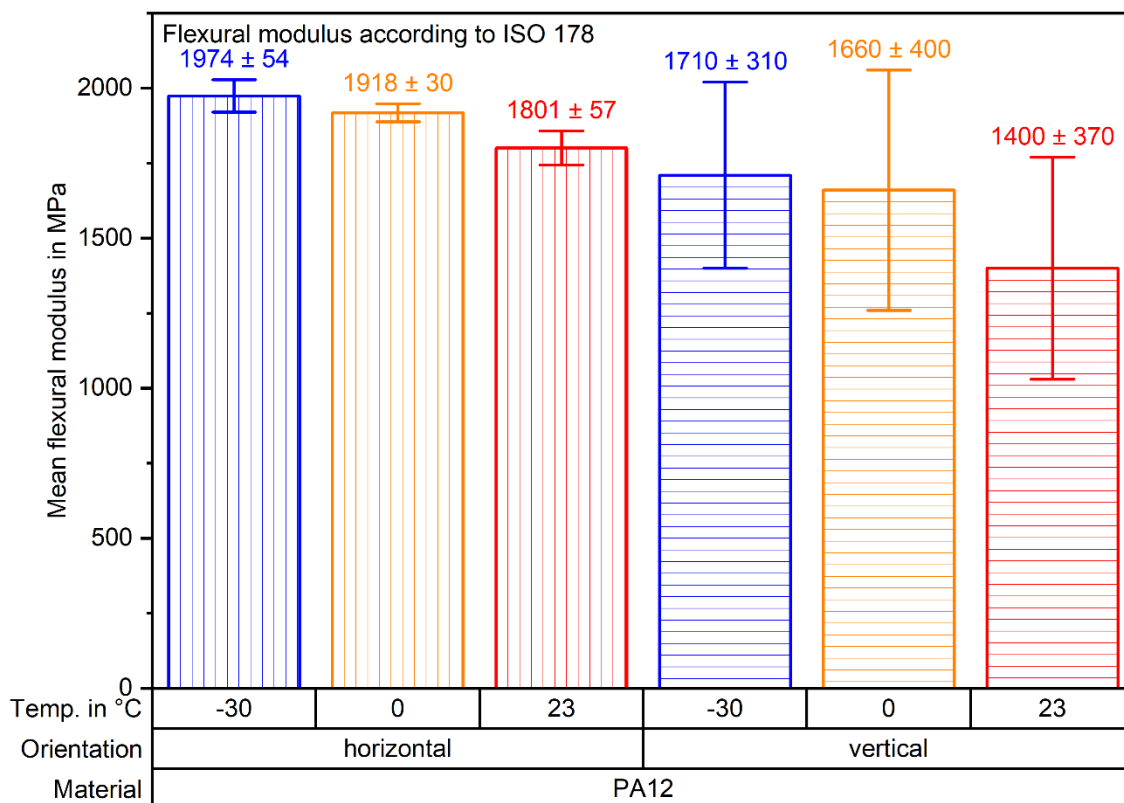


Figure 4.8: Mean flexural modulus of PA12 for horizontal and vertical oriented specimens.

Table 4.2: Mean 3PB test results for PA12.

Orientation	Temperature	Flexural strength	Strain at break	Flexural modulus
	in °C	in MPa	in %	in MPa
horizontal	-30	94.9 ± 3.0	6.76 ± 0.44	1974 ± 54
	0	87.3 ± 1.4	7.95 ± 0.76	1918 ± 30
	23	75.2 ± 1.7	10.4 ± 1.7	1801 ± 57
vertical	-30	62 ± 15	3.98 ± 0.52	1710 ± 310
	0	57 ± 20	3.88 ± 0.93	1660 ± 400
	23	43 ± 17	3.84 ± 0.68	1400 ± 370

4.1.2.4 VS-structure compression tests

To compare the influence of different material modeling approaches on the simulations of VS-structures, compression tests of additively manufactured structures were performed. The experimental approach is described in section 3.7. Figure 4.9 shows the compressive stress – strain curves for each test, structure, and temperature (0 °C and -30 °C only for structure B). For each test condition five structures were tested.

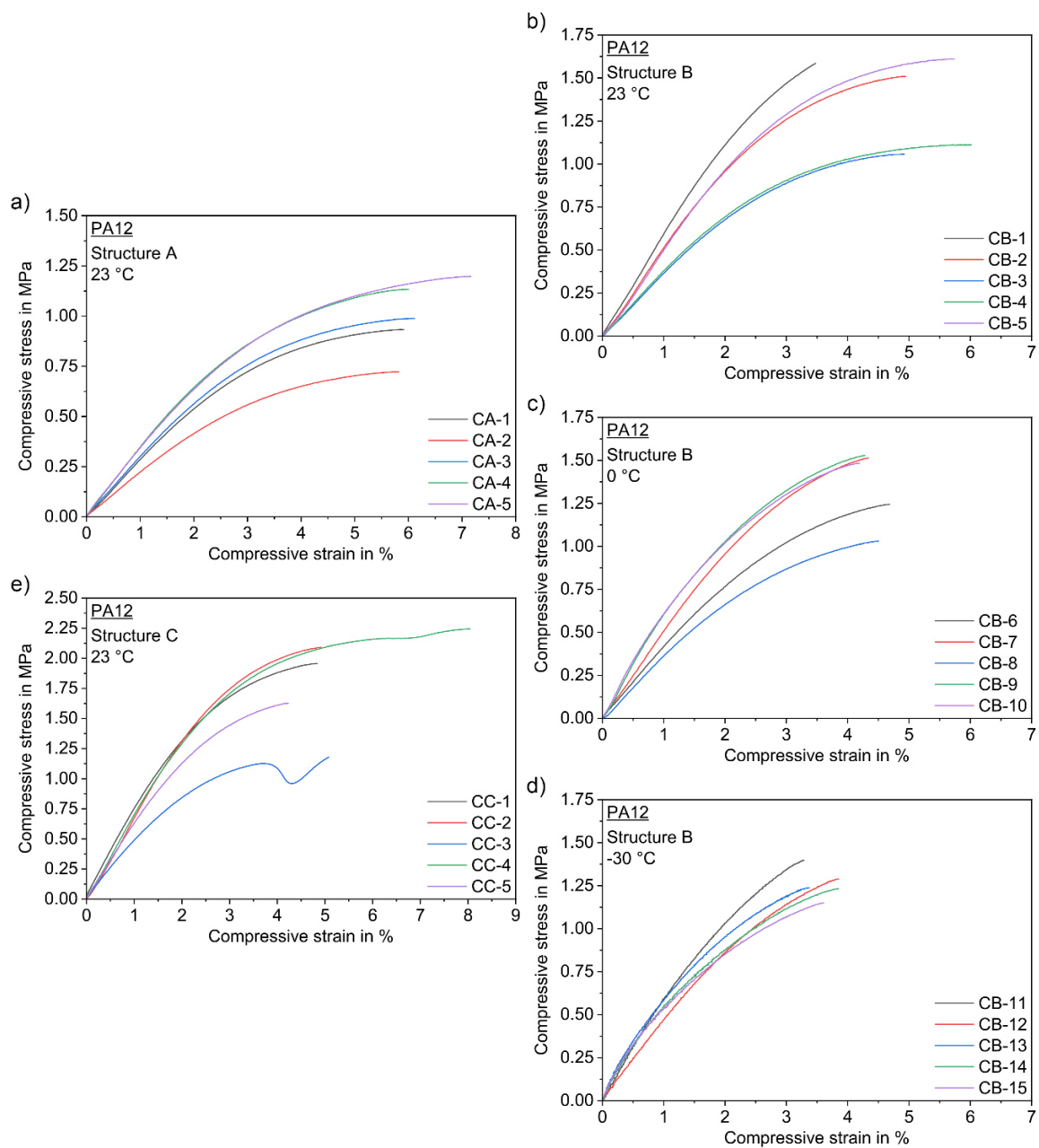


Figure 4.9: PA12 compressive stress – strain curves for all five repetitions for a) VS-structure A at 23 °C, b) VS-structure B at 23 °C, c) VS-structure B at 0 °C, d) VS-structure B at -30 °C and e) VS-structure C at 23 °C.

Figure 4.10 a) and b) shows the mean compressive strength and compressive strain at break, respectively. Figure 4.11 shows the compressive modulus of the tested PA12-VS-structures. It can be observed that structure A has the lowest mean compressive modulus (30 MPa), structure C has the highest (61 MPa) and structure B at 23 °C (43 MPa) has a value in between the two. According to Fleisch et al. [7], this behavior was expected based on the set of geometric parameters of the different VS-structures. The same trend is visible for the compressive strength (structure A has 1 MPa, B has 1.4 MPa and C has 1.9 MPa) (see Figure 4.10 a)). The strain at break results in Figure 4.10 b) show that structure A has the highest possible strain (8.1 %) and structure B at 23 °C (5.9 %) and C (6.1 %) have similar values. Overall, the standard deviation is very noticeable across all the mechanical parameters obtained from the measurements. This can be explained by the printing direction of the struts during the manufacturing process. Since they were oriented along the z-direction, the layer adhesion has a significant influence on the mechanical properties of the structure (see sections 4.1.2.2 and 4.1.2.3). Additionally, geometric imprecisions of the structure by the manufacturing process further increase the deviations.

The behavior of VS-structure B shows the expected temperature dependency for polymers. That is, for increasing temperature the compressive modulus decreases (from 66 MPa to 43 MPa) and the strain at break increases (from 4 % to 5.9 %). According to the literature the compressive strength should decrease for increasing temperature [24, 28, 64]. Due to the noticeable standard deviations of the measurements, this cannot be confirmed or denied. The compression test results are summarized in Table 4.3.

Table 4.3: Mean compression test results for PA12-VS-structures.

Structure	Temp.	Compressive strength	Strain at break	Compressive modulus
	in °C	in MPa	in %	in MPa
A	23	1.05 ± 0.24	8.11 ± 0.91	29.6 ± 6.2
B	-30	1.32 ± 0.13	4.00 ± 0.45	66 ± 12
	0	1.37 ± 0.22	4.79 ± 0.33	50 ± 13
	23	1.38 ± 0.27	5.9 ± 1.4	42.9 ± 8.4
C	23	1.86 ± 0.39	6.1 ± 1.2	61.0 ± 7.8

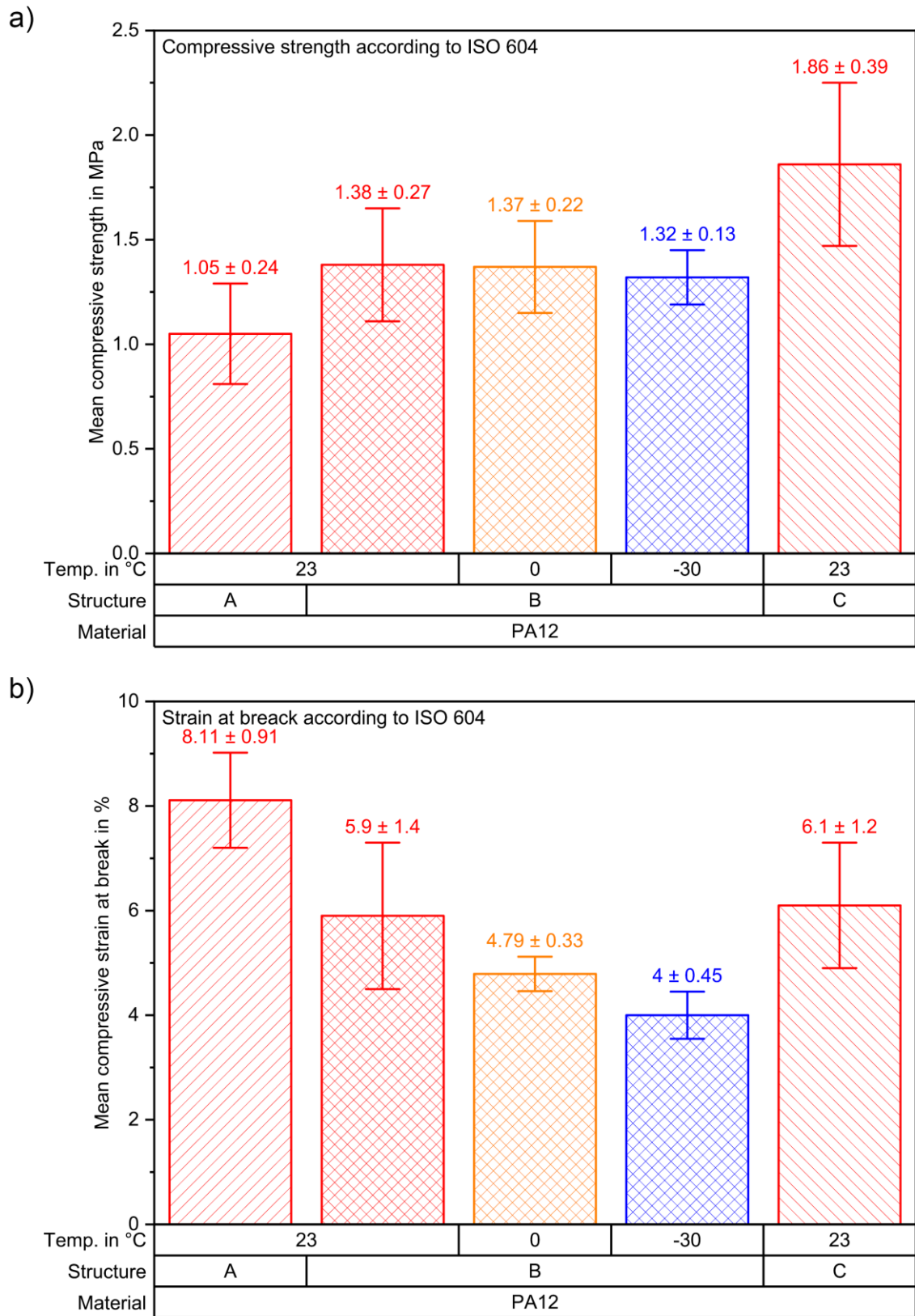


Figure 4.10: PA12 compression test results. a) Mean compressive strength and b) mean compressive strain at break.

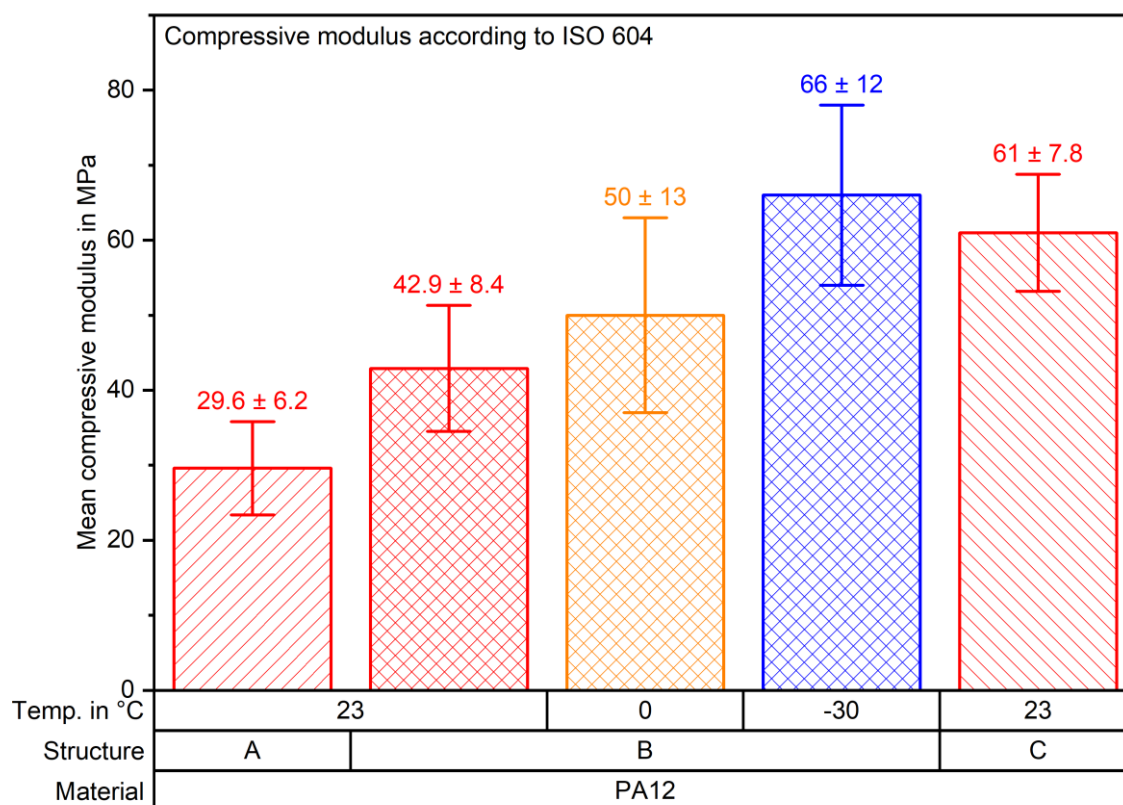


Figure 4.11: Mean compressive modulus for PA12-VS-structures.

4.1.3 Material modeling

To investigate the influence of the different experimental approaches on the quality of elastic-plastic material models used to simulate mechanical metamaterials, various tensile and 3PB based material models were created. The following sections describe the input data and the resulting material models.

4.1.3.1 Tensile based yield stress – plastic strain model

To generate an elastic-plastic material model based on tensile tests, the approach described in section 3.8.1.1 was used. To reduce the simulation effort only one model for each temperature and print orientation was calculated. Therefore, the test data needed to be averaged first. Two options exist for averaging multiple data curves. First, by averaging from 0% strain to the total maximum of all measurements. This would lead to discontinuities or jumps in the mean curve every time when the maximum strain of one measurement is reached. The second option is to average from 0% the minimum strain of all measurements. This option would avoid discontinuities or jumps but could lead, on the

other hand, to a loss of information especially if the minimum strain of one measurement is significantly lower than the rest of the specimens. Therefore, not all stress – strain measurements were considered for averaging. A good example can be seen in Figure 4.4 b), where the measurements ZS1 and ZS5 are significantly lower than ZS4. To avoid loss of information, only the measurements with a strain of $\geq 50\%$ of the maximum strain tested were considered for the material modeling. Figure 4.12 shows the mean tensile stress – strain curves for each temperature and print orientation.

Based on this data and the equations given in section 2.4.1.1 the yield stress – plastic strain behavior was calculated. The mean curves were calculated as described in section 3.8.1. Figure 4.13 shows the calculated yield stress – plastic strain behavior of the tested conditions and the datapoints used for the elastic-plastic material model. The data for both print directions show the already described trend that the material becomes more ductile with increasing temperature. Due to the averaging of the test data, the strain at break values cannot be used for further discussions but the yield stress data shows the already shown trend of decreasing stresses for increasing temperature.

As already mentioned, the elastic-plastic material model implemented in Abaqus uses the Young's modulus and the Poisson's ratio for the elastic part and the yield stress – plastic strain data for the plastic part. The used Young's modulus $E_{tens,valid}$ and the Poisson's-ratio ν_{valid} of the valid measurements (from the mean stress – strain curves) is given in Table 4.4. The 50 data points of the yield stress – plastic strain curve can be seen Table 7.1 and Table 7.2 in section 7.1.

Table 4.4: PA12 input data for elastic material models, based on tensile tests, in Abaqus.

Orientation	Temperature in °C	$E_{tens,valid}$ in MPa	ν_{valid}
horizontal	23	1901	0.39
	0	2065	0.38
	-30	2087	0.35
vertical	23	1864	0.39
	0	2054	0.37
	-30	2183	0.34

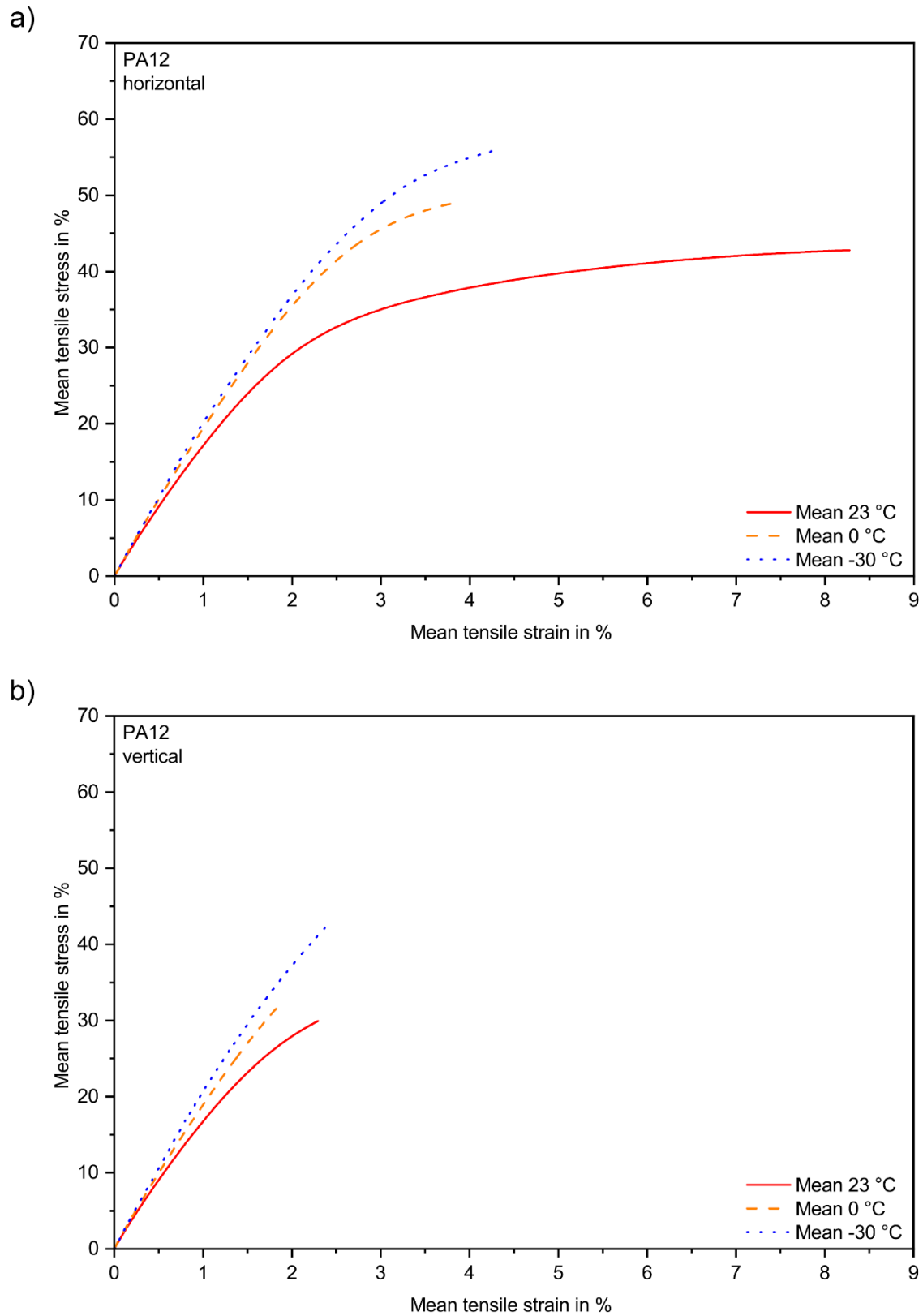


Figure 4.12: PA12 mean tensile stress – strain for a) horizontal and b) vertical print direction.

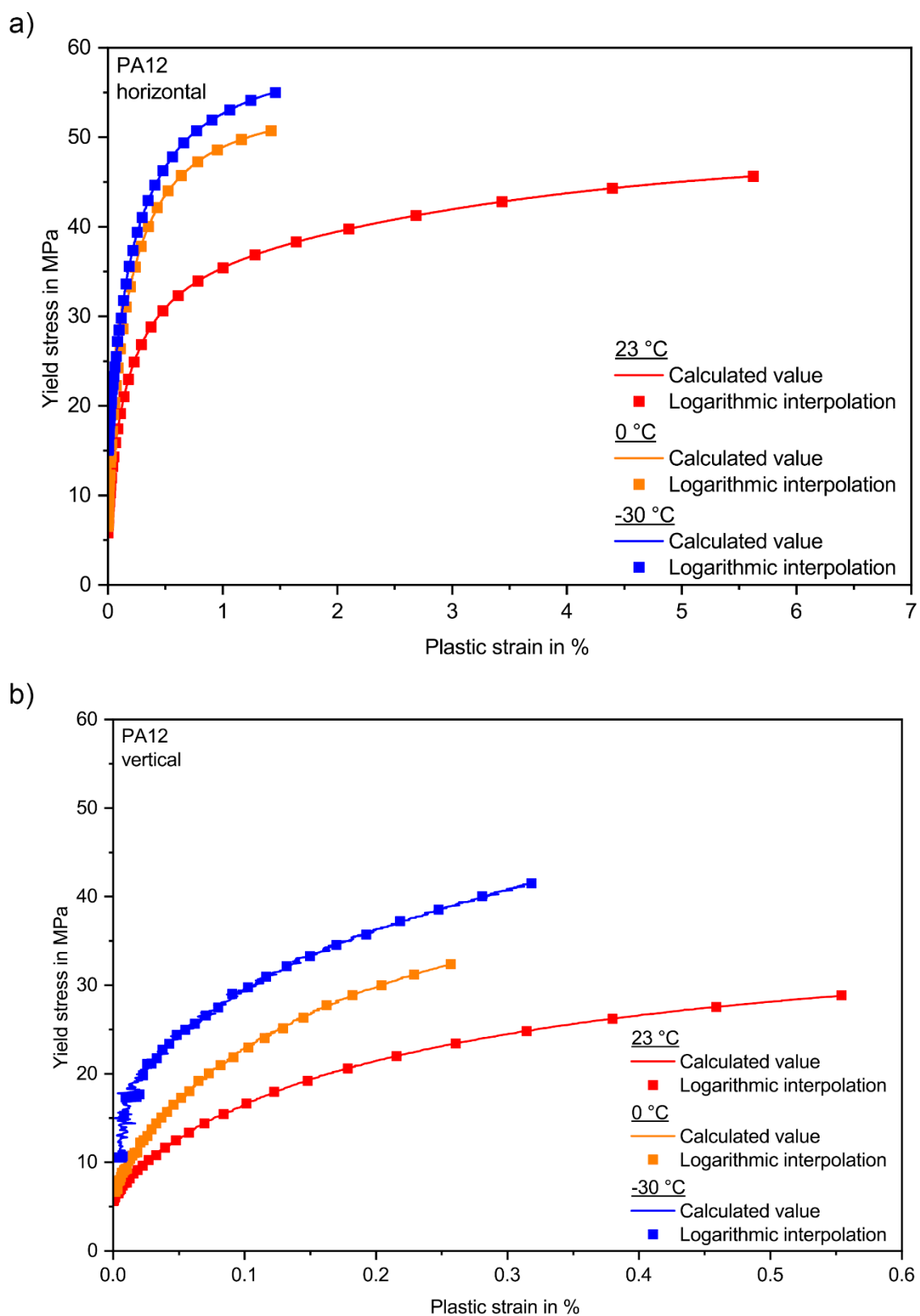


Figure 4.13: PA12 yield stress – plastic strain for a) horizontal and b) vertical print direction.

4.1.3.2 3PB tests-based Johnson-Cook optimization

Based on the experimental approach for the iterative optimization processes, as described in section 3.8.1.2, the Johnson-Cook parameters for each temperature and print orientation were calculated. Similar to the averaging process for the tensile test data, as explained in section 4.1.3.1, the mean bending force – deflection was calculated for all test conditions. The simulation result of the underlying 3PB simulations for the optimization processes is a bending force – deflection curve. Another simplification of the 3PB simulation model is that the preload from the tests was not considered for the simulations. Therefore, the input test data of the bending force is shifted to zero. Figure 4.14 shows the mean force – deflection curves for each temperature and print orientation.

As already mentioned, only the Johnson-Cook parameters A , B and n are needed for the simulations in this study. Figure 4.15 shows the comparison of measured bending force – deflection curves and the resulting curves after optimization using the Johnson-Cook parameters. Table 4.5 shows the valid elastic (flexural modulus $E_{3PB,valid}$ and Poisson's ratio ν_{valid}) and plastic input parameters for the Abaqus material model.

Good agreement between the measured and optimized force – deflection curves can be observed (see Figure 4.15). Although Figure 4.15 a) shows a small deviation between the measured and the optimized force – deflection curves, this deviation is within the expected tolerances of this material modeling approach.

Table 4.5: PA12 input data for elastic-plastic material models, based on 3PB tests, in Abaqus.

Orientation	Temp.	elastic		plastic		
		$E_{3PB,valid}$ in MPa	ν_{valid}	JC – A	JC – B	JC – n
horizontal	23 °C	1801	0.39	1.0	65.2	0.126
	0 °C	1918	0.38	1.0	172.0	0.358
	-30 °C	1962	0.35	1.0	254.0	0.420
vertical	23 °C	1619	0.39	1.0	600.0	0.734
	0 °C	1801	0.37	1.0	761.0	0.663
	-30 °C	1795	0.34	1.0	421.0	0.500

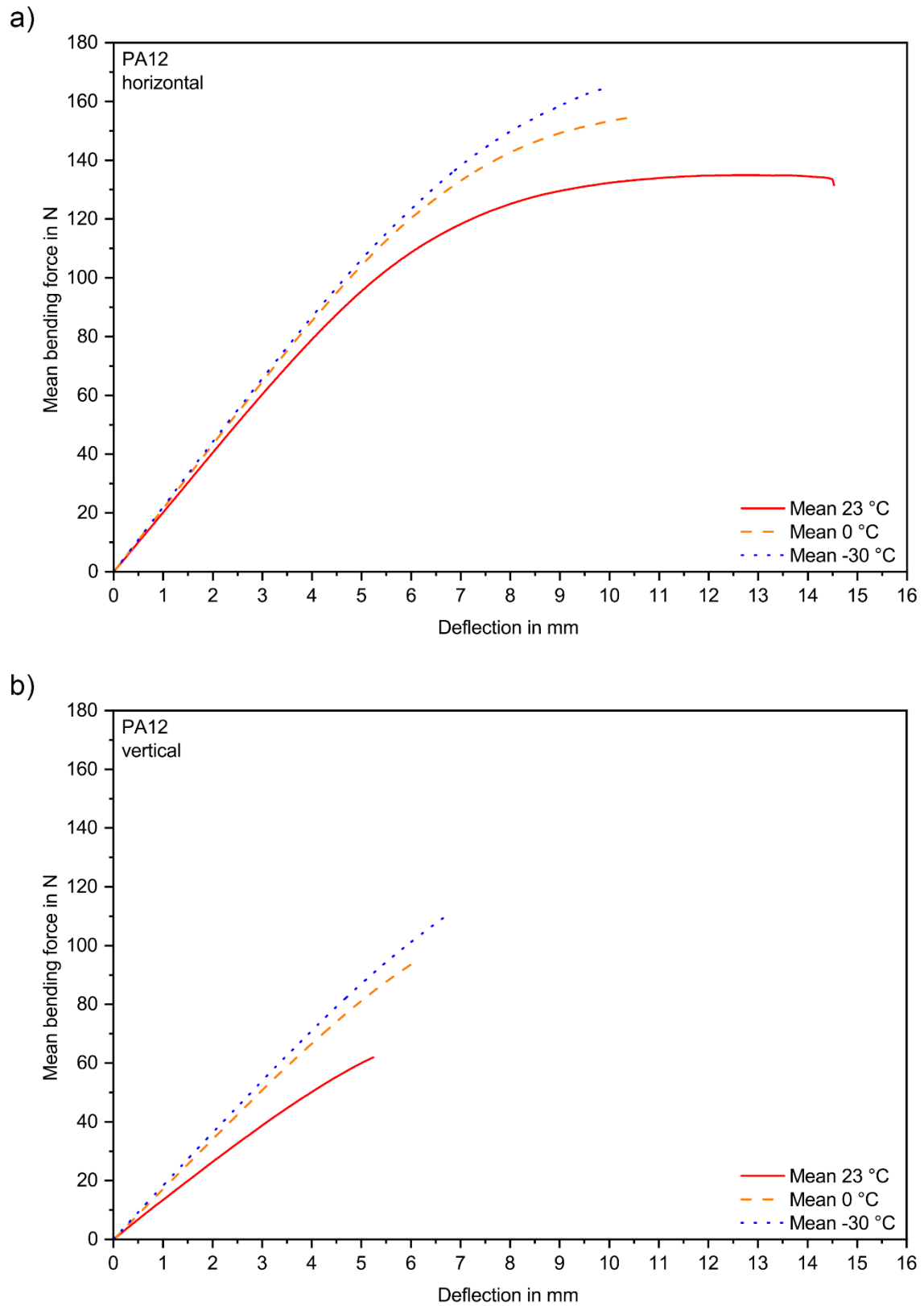


Figure 4.14: PA12 mean bending force – deflection of a) horizontal and b) vertical print direction.

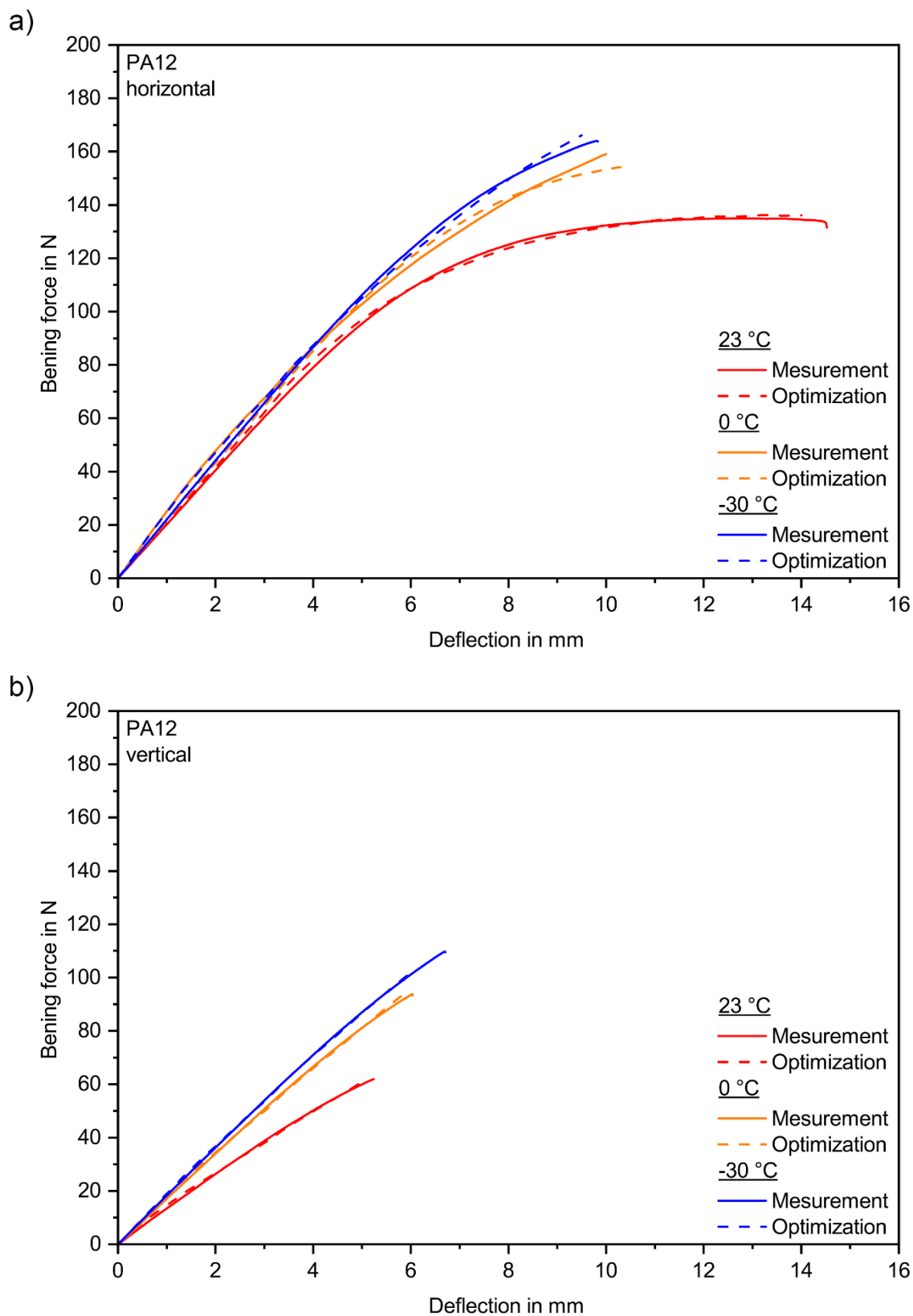


Figure 4.15: Comparison of measured and optimized bending force – deflection curves for PA12 with a) horizontal and b) vertical print direction.

It has to be noted that the material parameter A is set to a value of $A = 1$ during the optimization for every material model. The parameter A describes the offset of the yield curve and therefore the onset of the plastic behavior. Numerical effects or deviations of the model regarding process details (friction, preload, etc.) can lead to a mismatch in overall system stiffness. This then causes the optimization algorithm to compensate by creating an early onset of the plastic region by setting the parameter A to its minimal value.

Figure 4.16 shows the summary of the optimization history of the PA12 23 °C horizontal print direction measurement. The figure shows that after seven iterations the parameter A is tending to a minimum value.

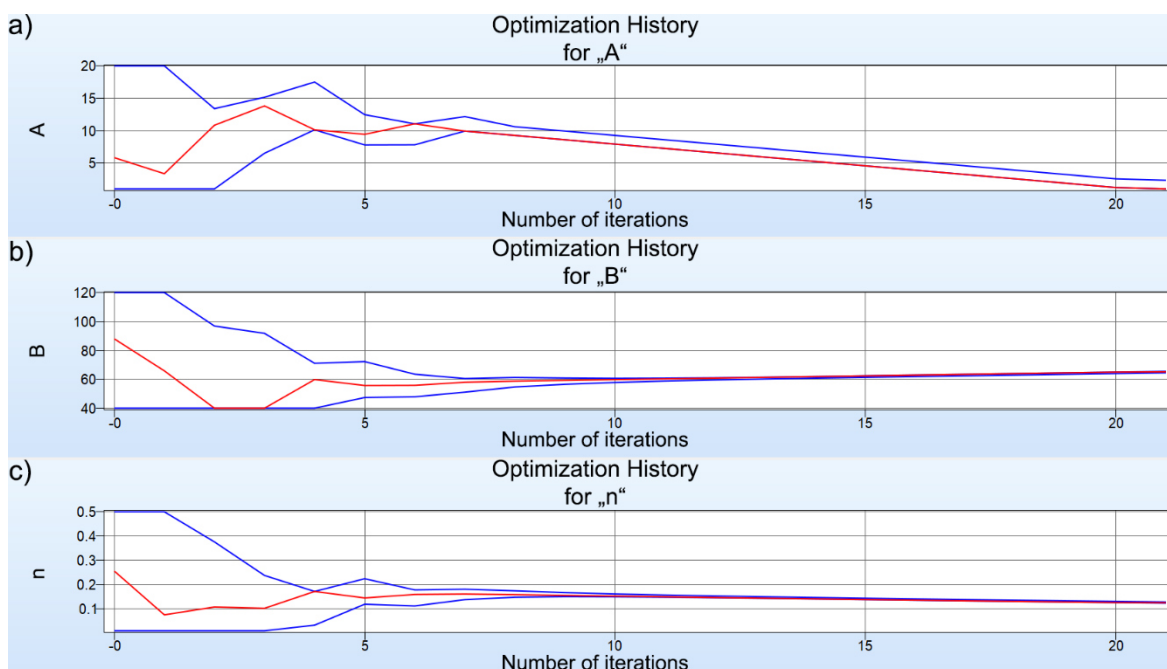


Figure 4.16: Optimization history of PA12-horizontal-23 °C. a) Parameter A , b) parameter B and c) parameter n .

4.1.4 VS-structure simulations and comparison

The simulation models were set up according to section 3.8.2 with the already mentioned material models. For this study, one simulation was made for each material modeling approach, as well as for horizontal and vertical print orientation. In addition, simulations for each temperature were conducted for VS-structure B. This results in a total of four simulations for VS-structures A and C and twelve simulations for VS-structure B. Figure 4.17 shows the nominal compressive strain – stress curves of the tested structures and the

associated simulations. An overall comparison of the shape of the given curves shows that the elastic-plastic material models (tensile and 3PB based) lead to a significant improvement when compared to a pure elastic model.

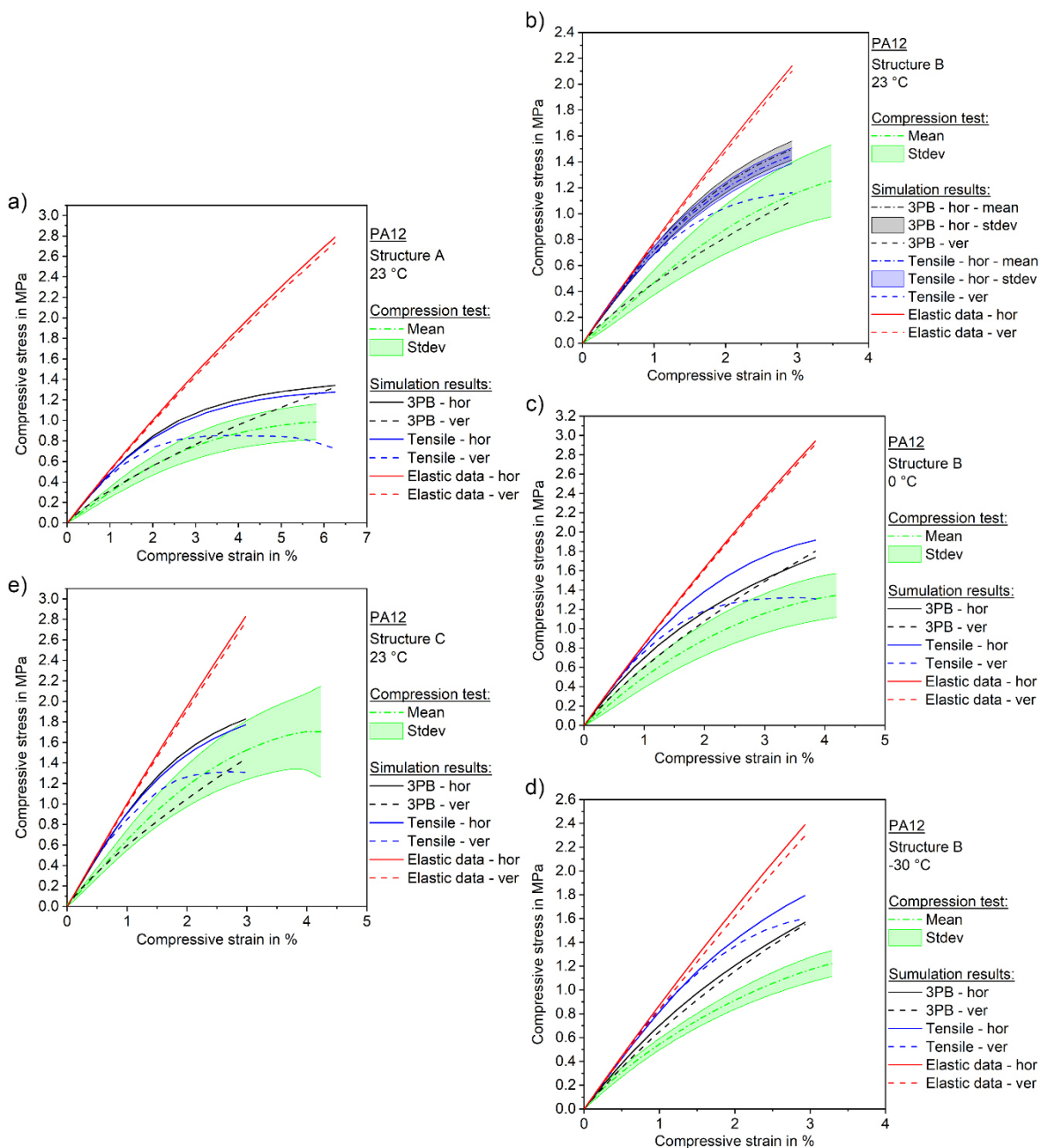


Figure 4.17: Compressive stress – strain of the VS-structures of PA12 with mean test data and simulation results for tensile and 3PB based material model in horizontal and vertical print direction. a) Structure A at 23 °C, b) structure B at 23 °C, c) structure B at 0 °C, d) structure B at -30 °C and e) structure C at 23 °C.

In addition, Figure 4.17 b shows error simulations using material models based on the tensile and 3PB standard deviations. For these models, the basic material test data was calculated by adding (for the upper boundary) and subtracting (for the lower boundary) the standard deviation (Stdev) to the mean values for both the tensile and 3PB data for PA12 with horizontal print direction at 23 °C. After calculating the upper and lower boundary test data, the material modeling for tensile and 3PB measurements, shown in section 3.8.1.1 and 3.8.1.2, was performed with this data and simulations were set up. This resulted in four additional simulations to display the deviation trend of the simulation data. To reduce the material modeling effort, it was then evaluated if the standard deviation of the simulated compressive modulus is comparable to the deviation of the tensile and bending test data, since simulations should be linear in low strain regions. Since the relative deviations of the tests and the compression simulations using the correlating material models are in similar ranges (see Table 4.6), the deviations for the final comparison of the compressive moduli of the VS-structures are calculated using the relative deviation of the mechanical tests (tensile and 3PB independently). For this comparison, only the relative deviation was considered. This simplification was done to reduce the material modeling and simulation effort significantly and to show the possibility of error simulations for the final comparison.

Table 4.6: Mean values and standard deviations of the moduli for the comparison of the error simulations.

		Moduli (tensile, 3PB and compressive) of PA12; horizontal print orientation; 23 °C		
		Mean in MPa	Stdev. in MPa	Relative deviation in %
Tensile based	test data	1900	60	3.1
	comp. sim	80	3.1	3.8
3PB based	test data	1800	57	3.2
	comp. sim	80	3.0	3.7

Figure 4.18 shows the mean values and the standard deviation of the moduli given by the mechanical tests and the simulations. The figure shows the compressive modulus for PA12 for each orientation, temperature, and test method. In general, the data shows that the simulations results have a higher stiffness when compared to the compression tests. It

must be mentioned that for the simulations the, near to reality, CAD models using the measured geometric parameters (see section 3.1.2.2) were chosen. However, it was not possible to measure the geometric parameters of the unit cells on the inside of the structure. Because of this and the high complexity of the structures itself, which might affect the print quality during manufacturing, the large deviation of the compression structures can be explained (compare Figure 4.9 and Figure 4.17). Figure 4.18 also shows that the compressive modulus based on the 3PB test material models is in general lower than the data given by the tensile based models. This trend was expected as the flexural modulus is smaller than the tensile modulus (see Figure 4.5 and Figure 4.8). Finally, the simulations using the material models based on the 3PB tests with specimens in vertical print direction show the best agreement regarding the stiffness between simulation and the real compression tests for each VS-structure. Due to the fact the struts of the VS-structures were deformed under a bending load it was already assumed that the 3PB based models should fit the real compression tests better than the tensile based material models. A possible conclusion why the vertical based models fit the compression tests better can be found in the assumption that the structures were produced along the z-axis of the SLS printer (see section 3.1.2.2). This would cause layer changes under a specific angle (based on the geometric parameters of the unit cell) and in combination with the bending load distribution along the thickness of the struts a mixed mode between the pure horizontal and vertical loading of the material is created. The results show that this mixed mode can be best described with vertical based material models.

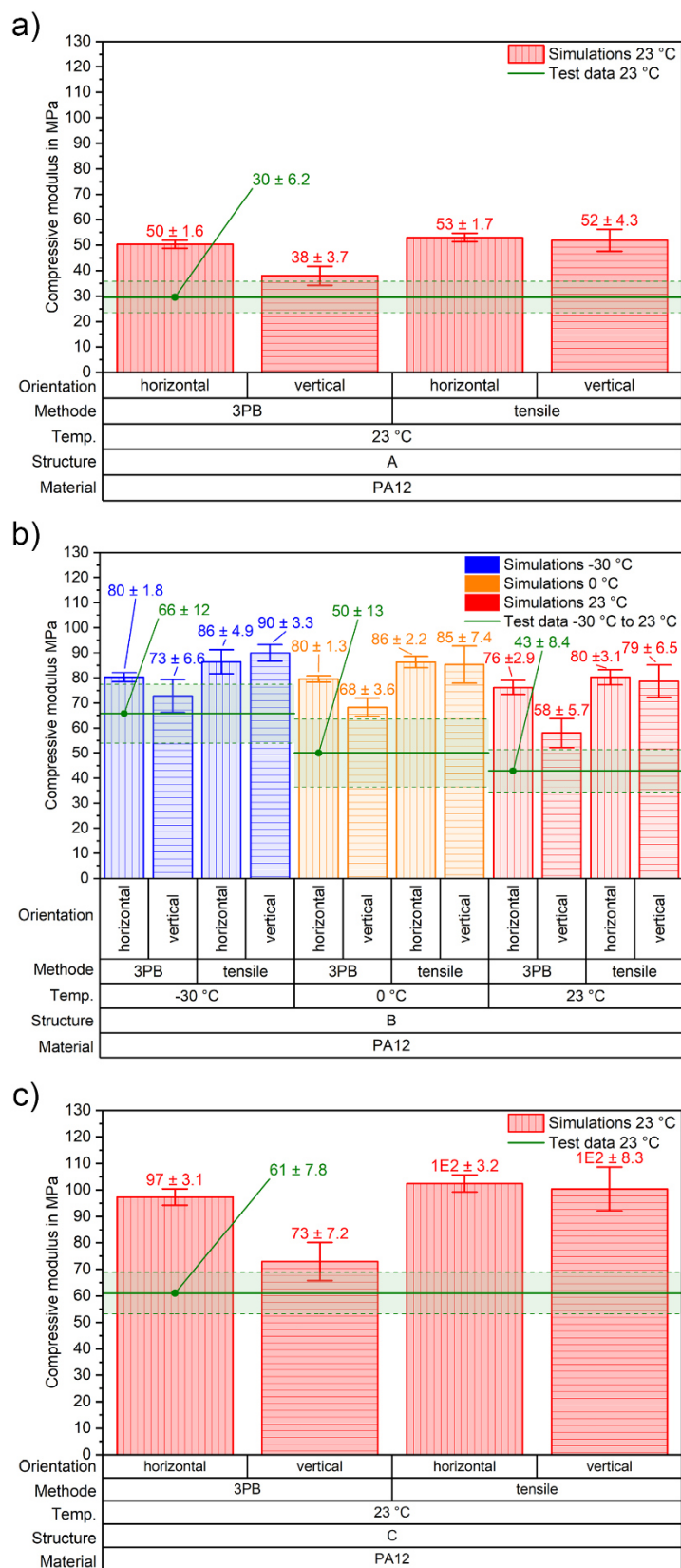


Figure 4.18: Comparison of the simulated compressive modulus for PA12 with horizontal and vertical print direction using tensile and 3PB based material models and the real compression test data for a) VS-structure A, b) VS-structure B and c) VS-structure C.

4.2 Polypropylene

4.2.1 DMA results

The DMA measurements for PP were performed using the test conditions as described in section 3.3. Figure 4.19 shows the storage module and the loss factor of the tested PP specimens. The measurements show a glass transition temperature of $T_{g,PP} = 5.3\text{ }^{\circ}\text{C}$. Between $-30\text{ }^{\circ}\text{C}$ and $0\text{ }^{\circ}\text{C}$ a big drop (from 2500 MPa to 1400 MPa) is observed. The drop marks the glass transition region where the deformation behavior of polymers changes significantly [28]. According to the literature, the T_g for standard PP types can be found in the range of $-10\text{ }^{\circ}\text{C}$ for static testing to $10\text{ }^{\circ}\text{C}$ for dynamic testing [24, 30].

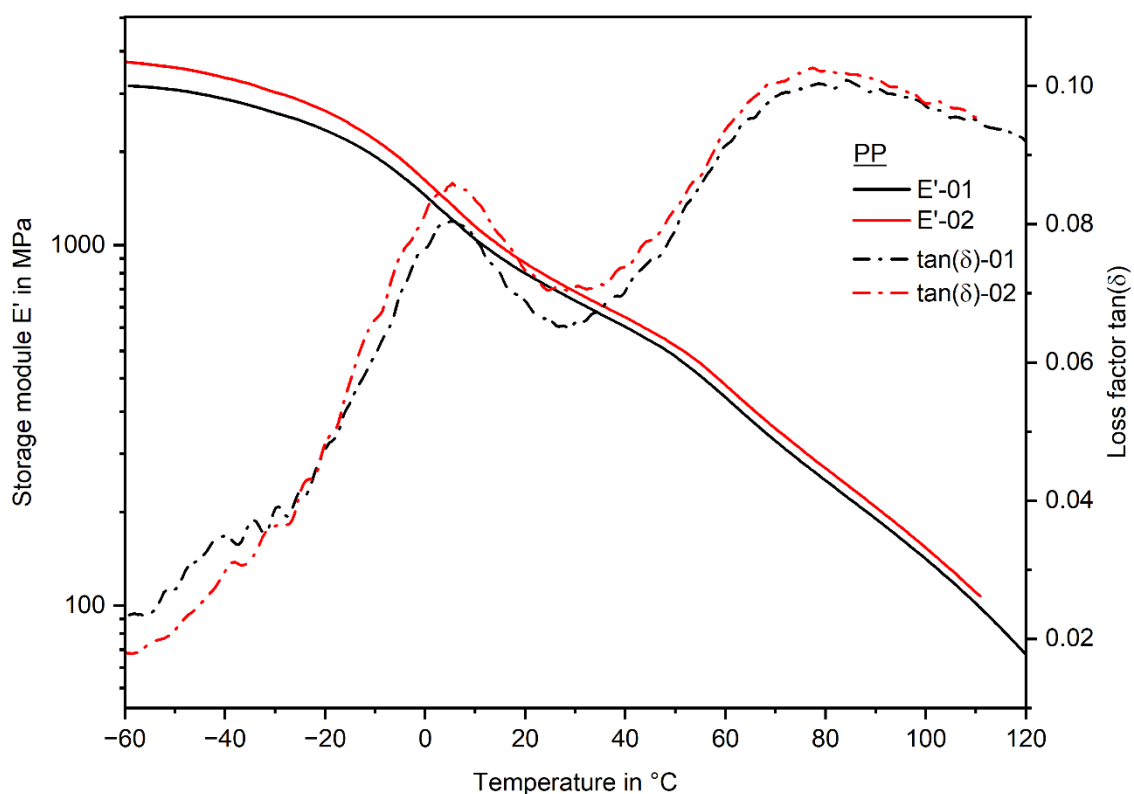


Figure 4.19: Storage module and loss factor of PP.

4.2.2 Mechanical testing

The same set of mechanical tests as for PA12 were carried out for PP. This includes Charpy impact, tensile, 3PB and compression tests.

4.2.2.1 Charpy impact tests

Details of the evaluation and experimental setup of the Charpy impact tests are described in section 2.3.1 and section 3.4, respectively. Figure 4.20 shows the Charpy impact strength for the tested PP specimens in horizontal and vertical print direction for 23 °C, 0 °C and -30 °C. The data shows an increasing impact strength for horizontal (from 4.10 kJ/mm² to 13.4 kJ/mm²) and vertical (from 3.18 kJ/mm² to 7.8 kJ/mm²) print orientation for increasing temperature. In general, a decreased impact strength can be observed for the vertical oriented specimens, compared to the horizontal ones, similar to PA12. Although the effect is less pronounced. In addition, within the standard deviation the data are equivalent resulting in no clear trend. Noticeable is the big deviation of the measurements with the horizontal oriented specimens at 23 °C. The specimens were delivered in one batch and chosen randomly across Charpy and 3PB tests. In addition, the assignment to each test temperature was done randomly. As a result, no explanation for the big deviation for the 23 °C measurements with horizontal orientation can be given.

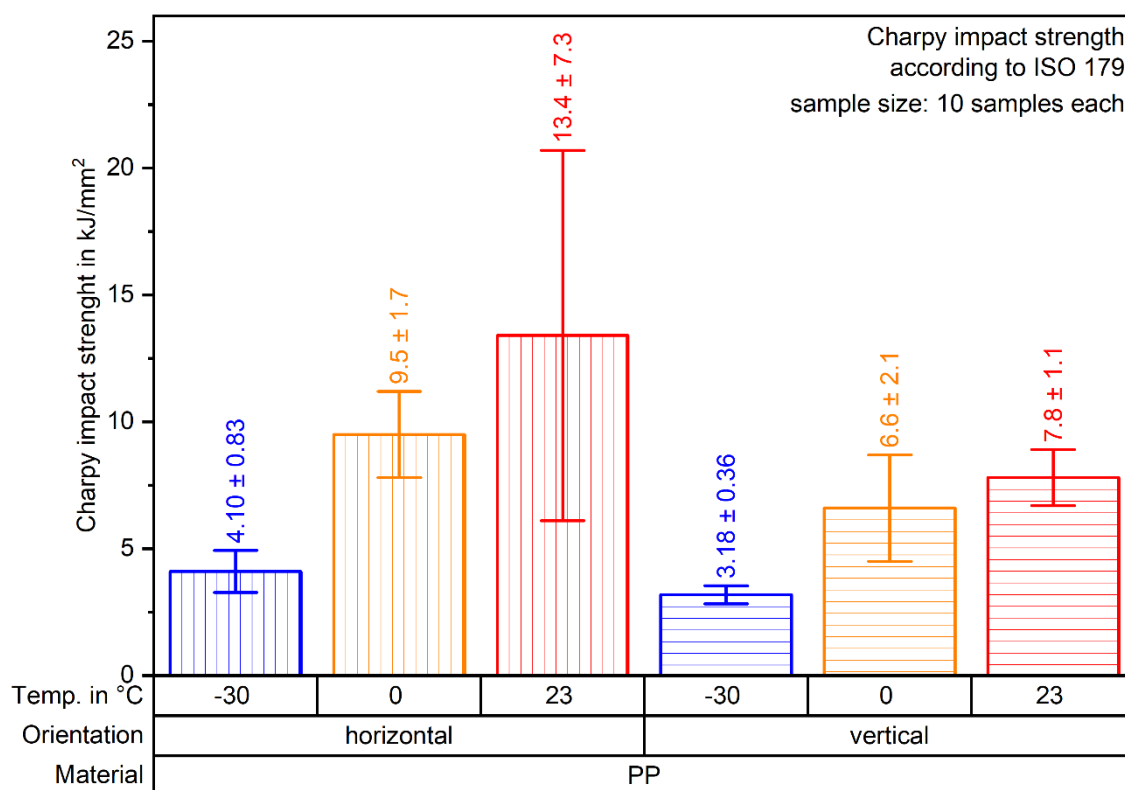


Figure 4.20: Mean Charpy impact strength of 10 specimens each orientation and temperature of PP.

4.2.2.2 Tensile tests

The tensile tests of PP were performed analogous to the measurements of PA12 described in section 4.1.2.2. The evaluation of the test data was done according to section 2.3.2.1 and the experimental approach is described in section 3.5. Figure 4.21 shows the tensile stress – strain curves for each measurement and test condition.

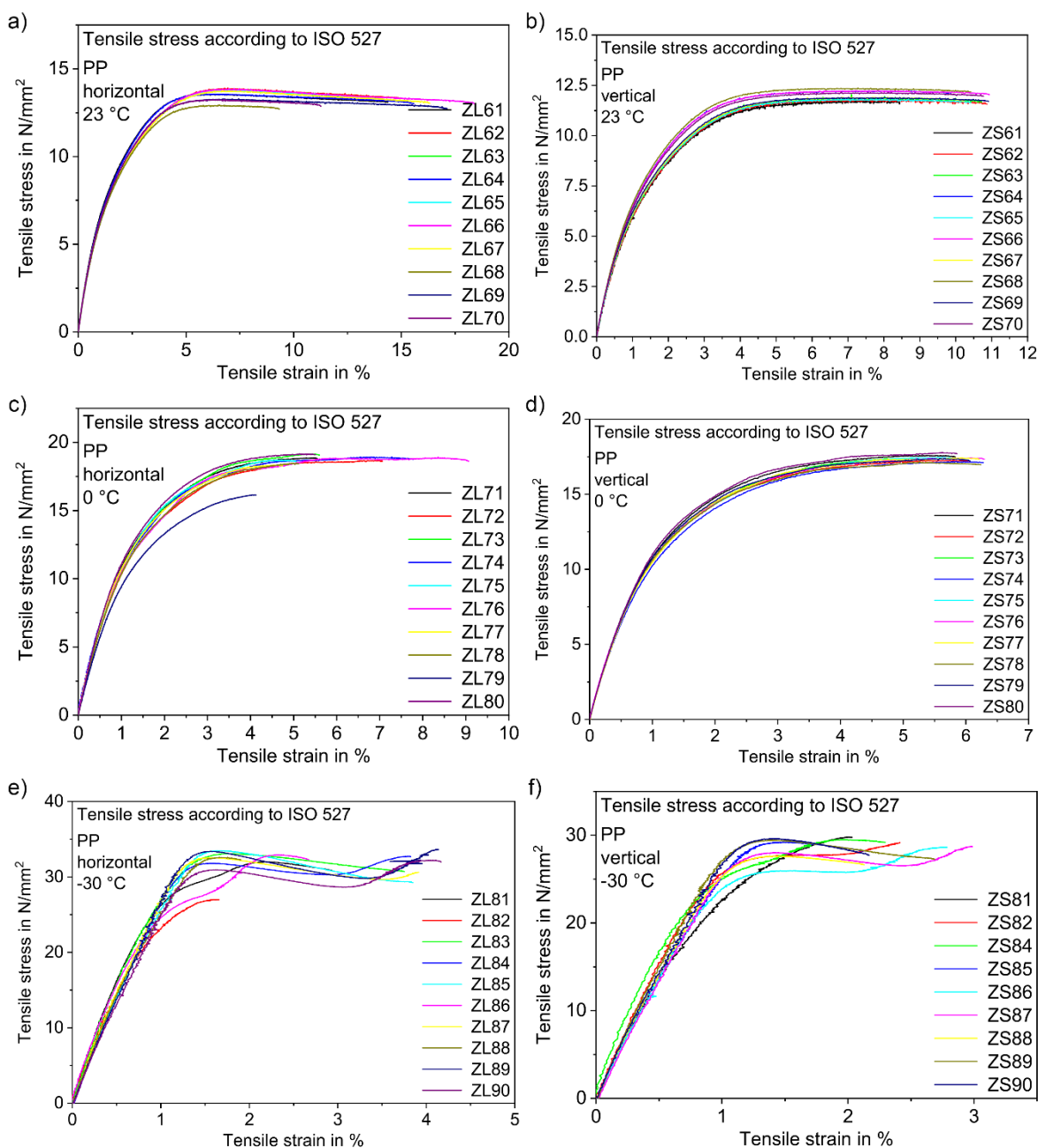


Figure 4.21: Tensile stress – strain curves of PP for a) horizontal at 23 °C, b) vertical at 23 °C, c) horizontal at 0 °C, d) vertical at 0 °C, e) horizontal at -30 °C and f) vertical at -30 °C.

Due to an error of the DIC system no data was saved for measurement ZS83 (vertical, -30 °C). Especially for the -30 °C a necking behavior was observed in some measurements. Due to a reduced plasticity of Polymers at lower temperatures this behavior was not expected to occur only for the -30 °C measurements [30]. Another explanation for this behavior can be given with slipping of the specimens in the mechanical clamps. The mechanical clamps were fastened with 20 Nm using a torque wrench. Due to the reduced temperature and a thermal contraction of the steel parts of the clamp an increase of the friction in the thread of the mechanical clamps occurs. Because of this increased friction, the applied 20 Nm may not have been enough to apply the required clamping force to the specimen. At this point no satisfying conclusion for this hypothesis can be made.

Figure 4.22 a) and b) shows the mean tensile strength and the main strain at break of the specimens with their respective standard deviation. It can be observed that the tensile strength is decreasing with increasing temperature (from 32 MPa to 14 MPa for horizontal and from 29 MPa to 12 MPa for vertical print direction). In contrast, the strain at break value is increasing with increasing temperature (from 3.3 % to 15 % for horizontal and from 2.4 % to 10 % for vertical print direction). Figure 4.23 a) and b) show the mean Young's modulus and the mean Poisson's ratio of the tested specimens, respectively. Similar to the tensile strength, the Young's modulus decreases with increasing temperature (from $3 \cdot 10^3$ MPa to $8.3 \cdot 10^2$ MPa for horizontal and from $3.1 \cdot 10^3$ MPa to $8.3 \cdot 10^2$ MPa for vertical oriented specimens). Figure 4.23 b) shows an increasing Poisson's ratio (from 0.34 to 0.43 for horizontal and from 0.29 to 0.42 for vertical oriented specimens) for increasing temperature. As previously described this trends fits to the commonly known behavior of for polymers [30, 64 - 66].

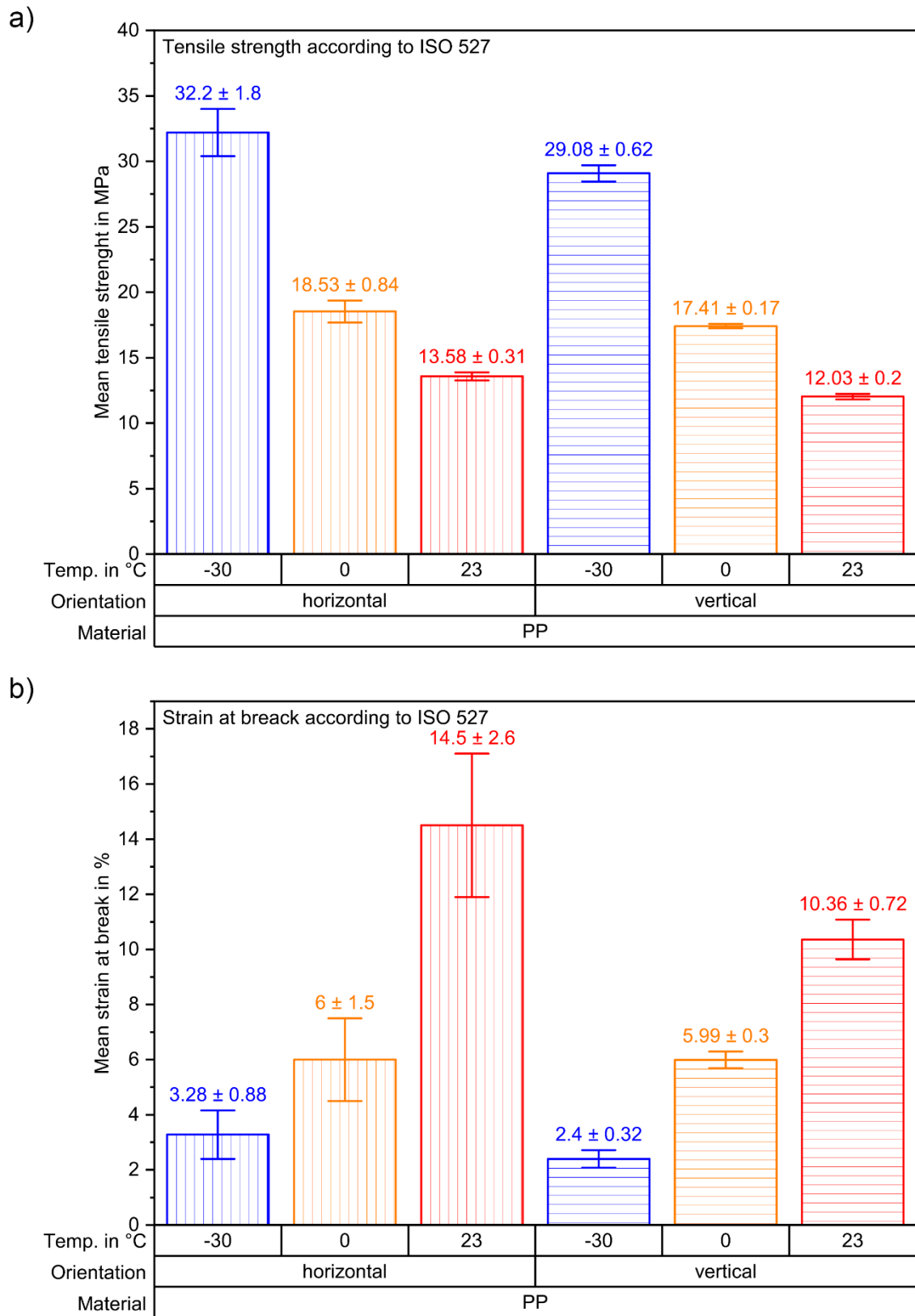


Figure 4.22: PP tensile test results. a) Mean tensile strength and b) mean strain at break.

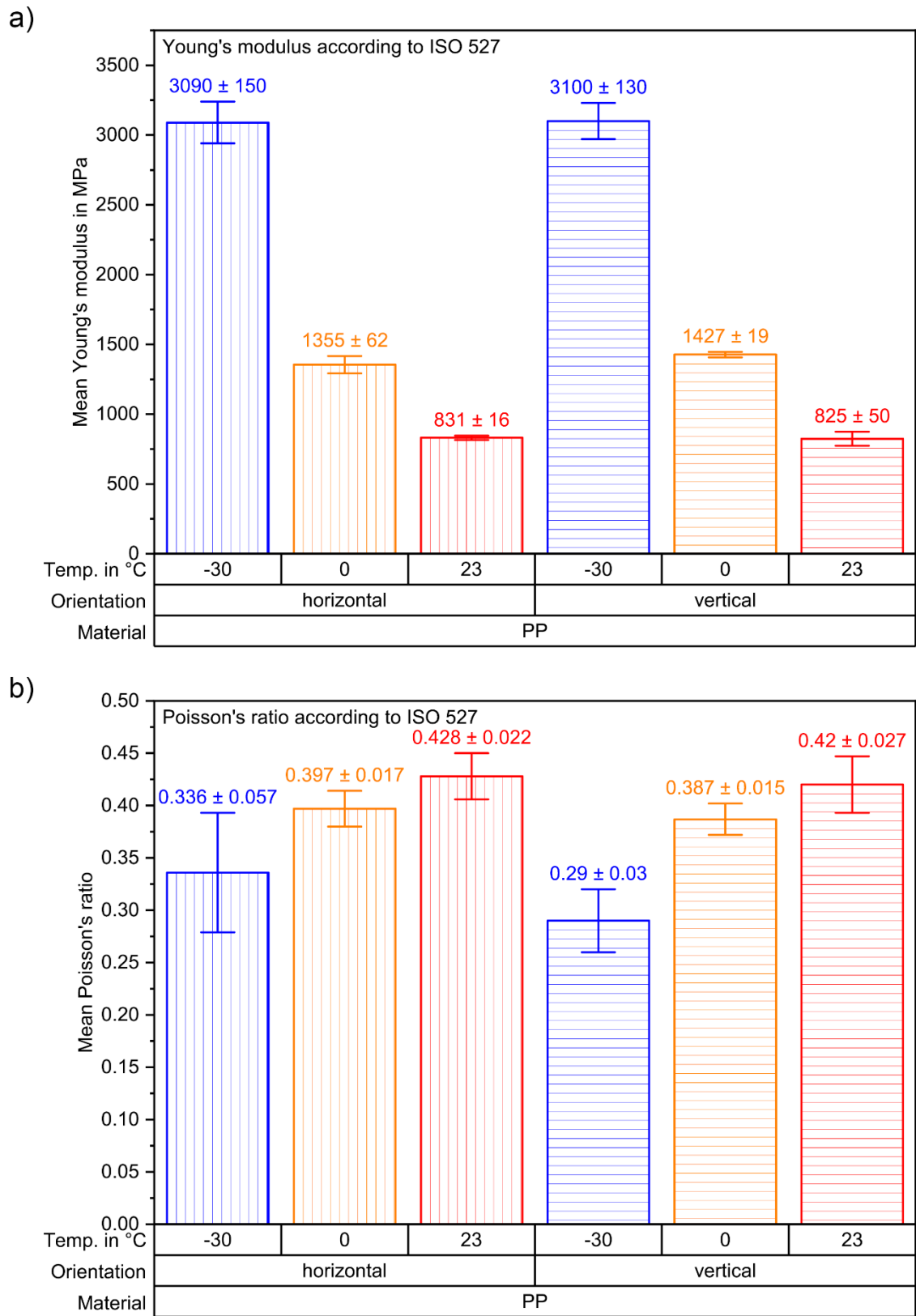


Figure 4.23: PP tensile test results. a) Mean Young's modulus and b) mean Poisson's ratio.

Noticeable is the strong decrease of the tensile strength and Young's modulus between -30 °C and 0 °C compared to 0 °C and 23 °C. This strong decrease can be explained by the transition between the energy-elastic and entropy-elastic state of semi crystalline polymers [26]. Characteristic for this transition is the glass transition temperature T_g [30]. The DMA measurement (see section 4.2.1) results in a value of $T_{g,PP} = 5.3$ °C. In addition, the measurement shows a stronger drop in the storage module between -30 °C and 0 °C compared to 0 °C and 23 °C, which marks the glass transition region in the area below 0 °C. Due to the observed drop in DMA measurements a strong change of the tensile behavior between -30 °C and 0 °C was expected and can be seen in the results. It is noticeable, that the Young's modulus shows no difference between horizontal and vertical oriented specimens. For the tensile strength and strain at break a small decrease is observed. The results of the tensile tests are summarized in Table 4.7.

Table 4.7: Mean tensile test results for PP.

Orient.	Temp.	Tensile strength	Strain at break	Young's modulus	Poisson's ratio
	in °C	in MPa	in %	in MPa	-
horizontal	-30	32.2 ± 1.8	3.28 ± 0.88	3090 ± 150	0.336 ± 0.057
	0	18.53 ± 0.84	6.0 ± 1.5	1355 ± 62	0.397 ± 0.017
	23	13.58 ± 0.31	14.5 ± 2.6	831 ± 16	0.428 ± 0.022
vertical	-30	29.08 ± 0.62	2.40 ± 0.32	3100 ± 130	0.290 ± 0.030
	0	17.40 ± 0.17	5.99 ± 0.30	1427 ± 19	0.387 ± 0.015
	23	12.03 ± 0.20	10.36 ± 0.72	825 ± 50	0.420 ± 0.027

4.2.2.3 3PB tests

Details of the evaluation and experimental setup of the 3PB tests are described in section 2.3.2.2 and section 3.6, respectively. Figure 4.24 shows the bending stress – strain curves for the tested specimens for each temperature and print orientation.

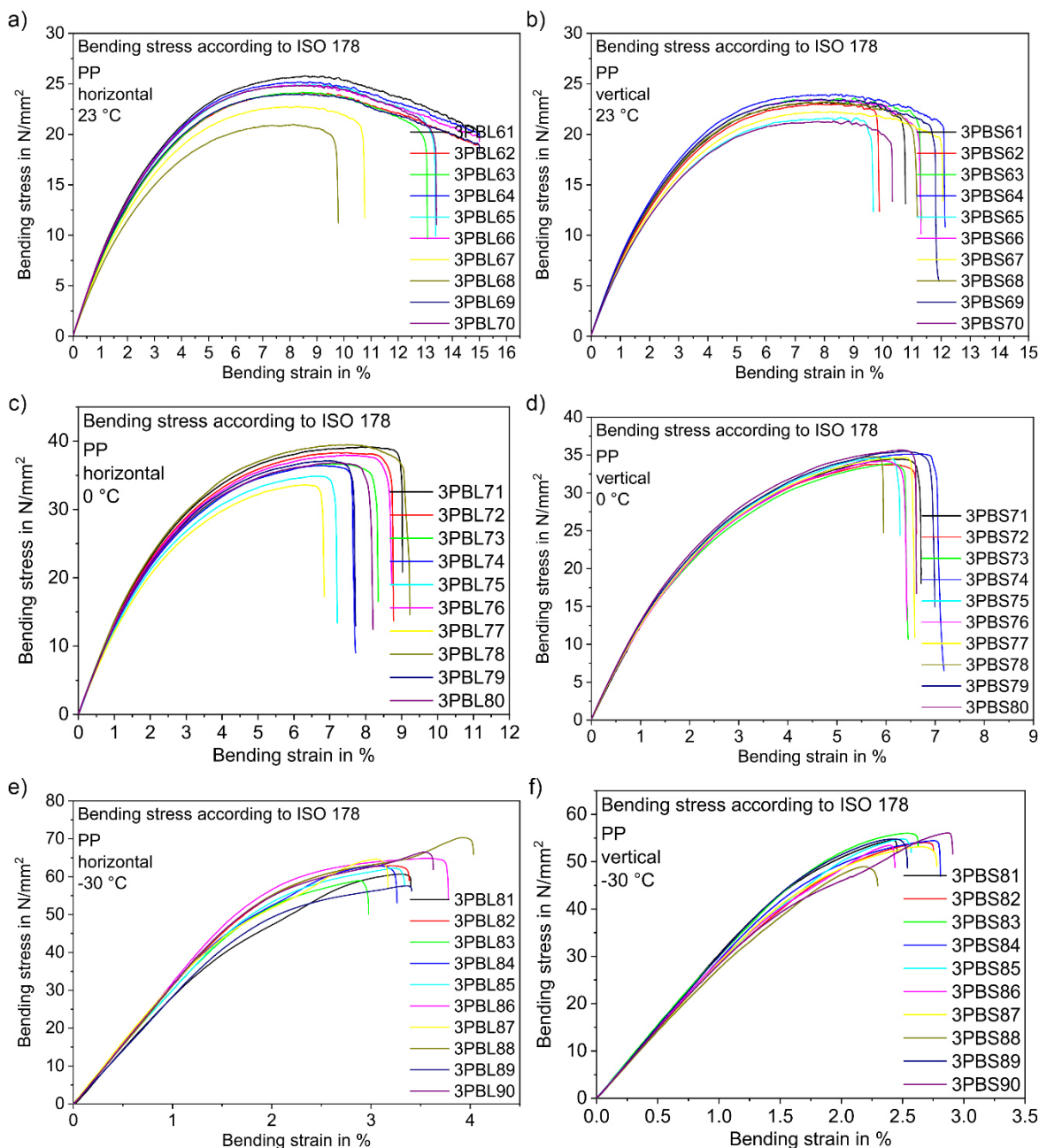


Figure 4.24: Bending stress – strain curves of PP for a) horizontal at 23 °C, b) vertical at 23 °C, c) horizontal at 0 °C, d) vertical at 0 °C, e) horizontal at -30 °C and f) vertical at -30 °C.

Figure 4.25 a) and b) shows the mean flexural strength and the mean strain at break of the specimens with their respective standard deviation. It can be observed that the flexural strength is decreasing for increasing temperature (64 MPa to 25 MPa for horizontal and from 55 MPa to 24 MPa for vertical print direction). The flexural modulus (see Figure 4.26) is decreasing for increasing temperature as well (from $3.1 \cdot 10^3$ MPa to $8.3 \cdot 10^2$ MPa for horizontal and from $3 \cdot 10^3$ MPa to $8.1 \cdot 10^2$ MPa for vertical oriented specimens). In contrast,

the mean strain at break is increases for increasing temperature (from 3.4 % to 14 % for horizontal and from 2.6 % to 11 % for vertical print direction). As already mentioned, this behavior fits to the trend described in the literature. Comparing the tensile tests, a strong decrease of the flexural strength and flexural modulus can be seen between the -30 °C and 0 °C as well. The possible reasons for the tensile behavior are described in section 4.2.2.2 and can be applied for the 3PB tests as well. The results of the 3PB tests are summarized in Table 4.8.

Table 4.8: Mean 3PB test results for PP.

Orientation	Temperature	Flexural strength	Strain at break	Flexural modulus
	in °C	in MPa	in %	in MPa
horizontal	-30	63.8 ± 3.5	3.44 ± 0.29	3130 ± 130
	0	37.7 ± 1.7	8.18 ± 0.75	1418 ± 47
	23	24.8 ± 1.3	13.5 ± 1.8	829 ± 40
vertical	-30	54.8 ± 1.9	2.62 ± 0.18	3010 ± 87
	0	35.38 ± 0.61	6.58 ± 0.33	1375 ± 32
	23	23.65 ± 0.82	11.06 ± 0.84	808 ± 34

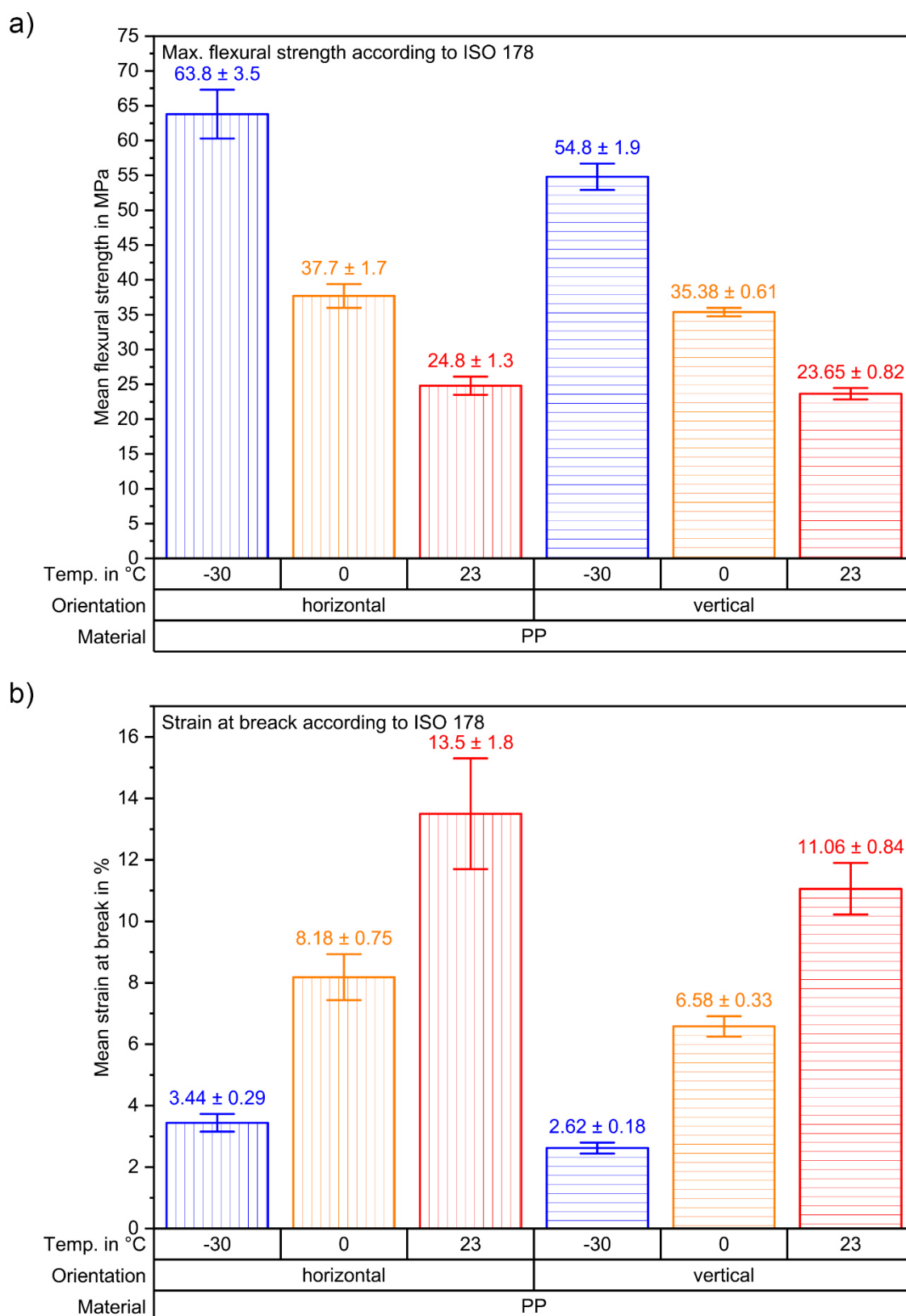


Figure 4.25: PP bending test results. a) Mean flexural strength and b) mean strain at break.

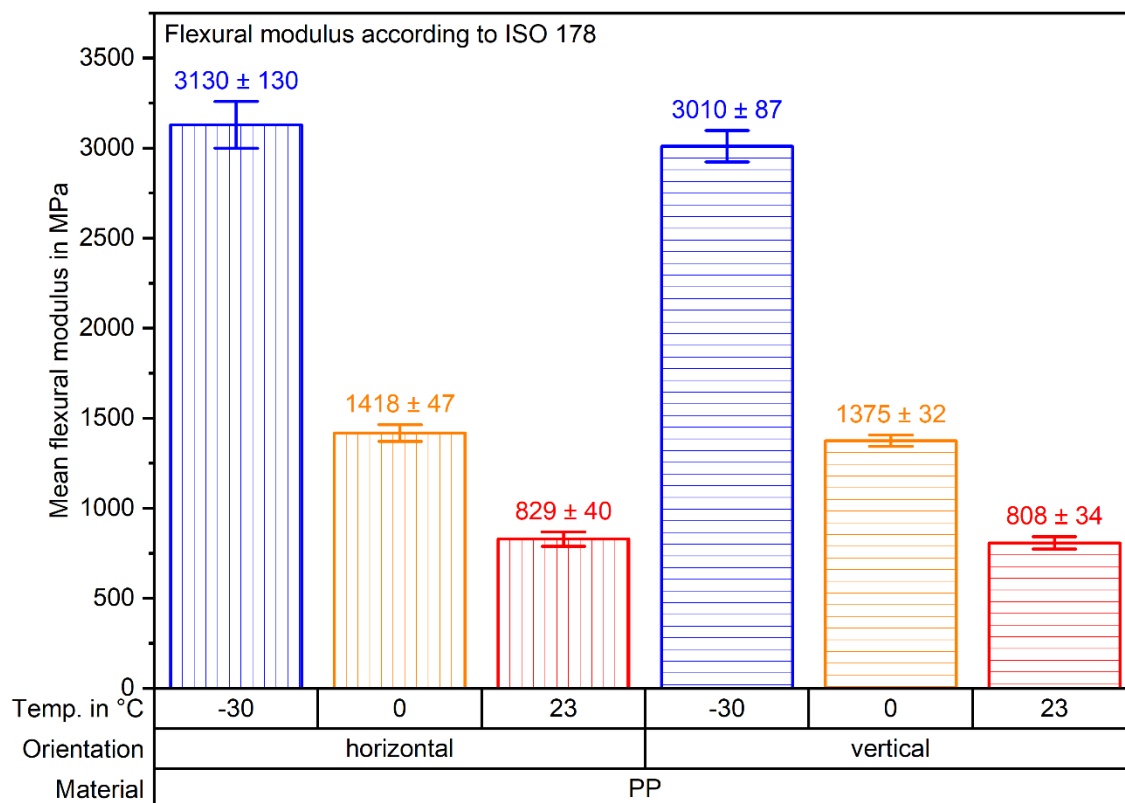


Figure 4.26: Mean flexural modulus of PP for horizontal and vertical oriented specimens.

4.2.2.4 VS-structure compression tests

The compression tests of the PP-VS-structures were performed using the experimental approach described in section 3.7 and the evaluation described in section 2.3.2.3. Figure 4.27 shows the compressive stress – strain for each test, structure, and temperature (0 °C and -30 °C only for structure B). For each test condition, five structures were tested.

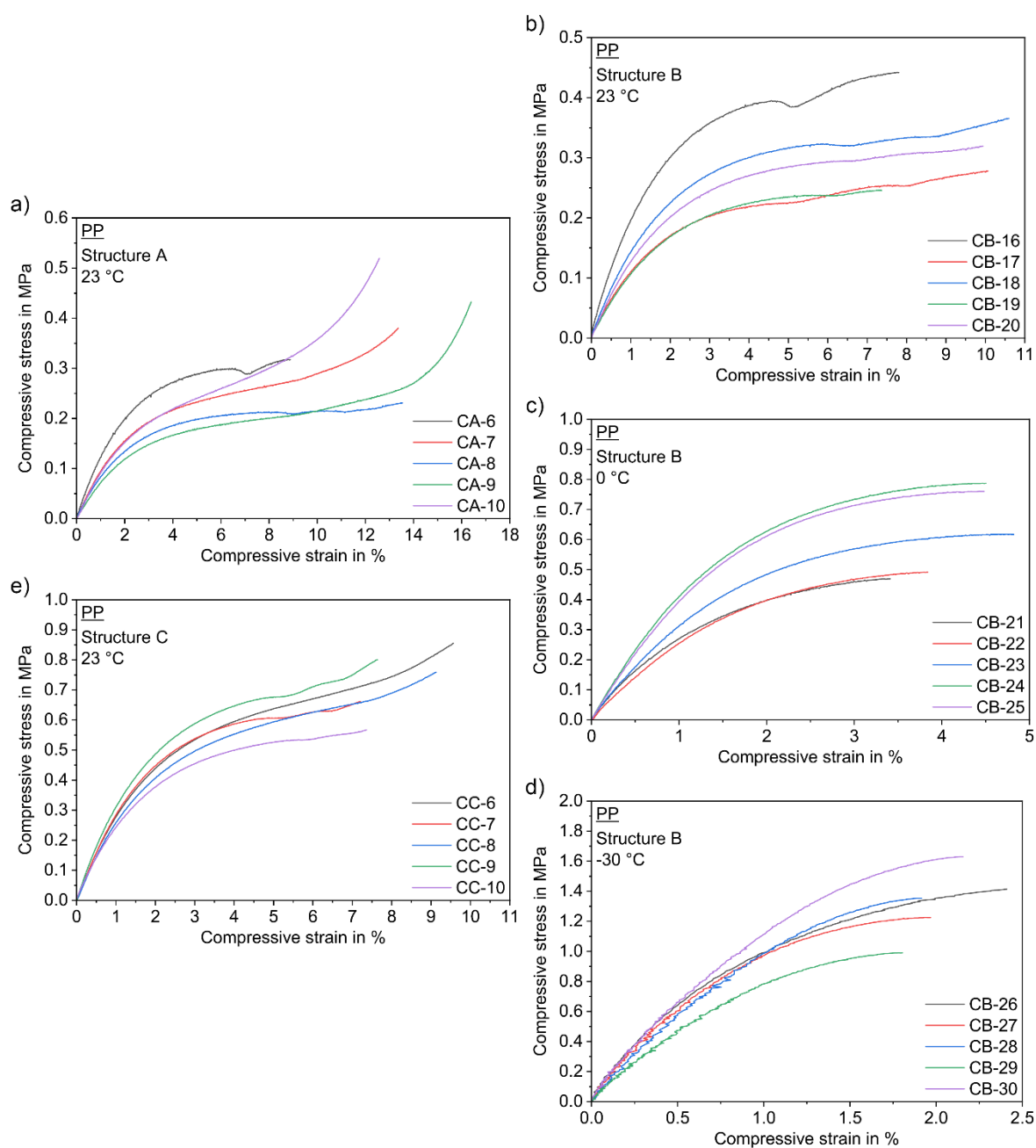


Figure 4.27: PP compressive stress – strain curves for all five repetitions for a) VS-structure A at 23 °C, b) VS-structure B at 23 °C, c) VS-structure B at 0 °C, d) VS-structure B at -30 °C and e) VS-structure C at 23 °C.

Figure 4.28 a) and b) shows the mean compressive strength and the mean strain at break, respectively. Figure 4.29 shows the mean compressive modulus for the tested PP-VS-structures. It can be observed that the stiffness increases from structure A (10 MPa) to structure C (33 MPa). This trend can be seen for the compressive strength as well (from 0.38 MPa for structure A to 0.73 MPa for structure B). Although the mean compressive

strength of PP-VS-structure B (0.33 MPa) is lower than the value for structure A (0.38 MPa). A more detailed consideration of the data shows, that the standard deviations of the tests are very high (compare test curves in Figure 4.27) which results in overlapping deviation margins for characteristic results, concluding that a further discussion is unreasonable.

The comparison of the temperature dependency of the VS-structure B shows a decreasing compressive strength (from 1.5 MPa to 0.33 MPa) and compressive modulus (from $1.2 \cdot 10^2$ MPa to 16 MPa) for increasing temperature. In contrast, the strain at break is increasing for increasing temperature (from 2.6 % to 9.2 %). A strong decrease of the compressive strength and compressive modulus can be seen between -30 °C and 0 °C. This trend was already seen for the tensile and 3PB behavior. The results of the compression tests are summarized in Table 4.9.

Table 4.9: Mean compression test results for PP-VS-structures.

Structure	Temp.	Compressive strength	Strain at break	Compressive modulus
	in °C	in MPa	in %	in MPa
A	23	0.38 ± 0.11	13.1 ± 2.5	10.4 ± 2.5
B	-30	1.47 ± 0.23	2.61 ± 0.31	124 ± 20
	0	0.64 ± 0.16	5.21 ± 0.49	39.4 ± 7.4
	23	0.332 ± 0.077	9.2 ± 1.4	15.8 ± 4.6
C	23	0.73 ± 0.12	8.2 ± 1.1	32.9 ± 3.8

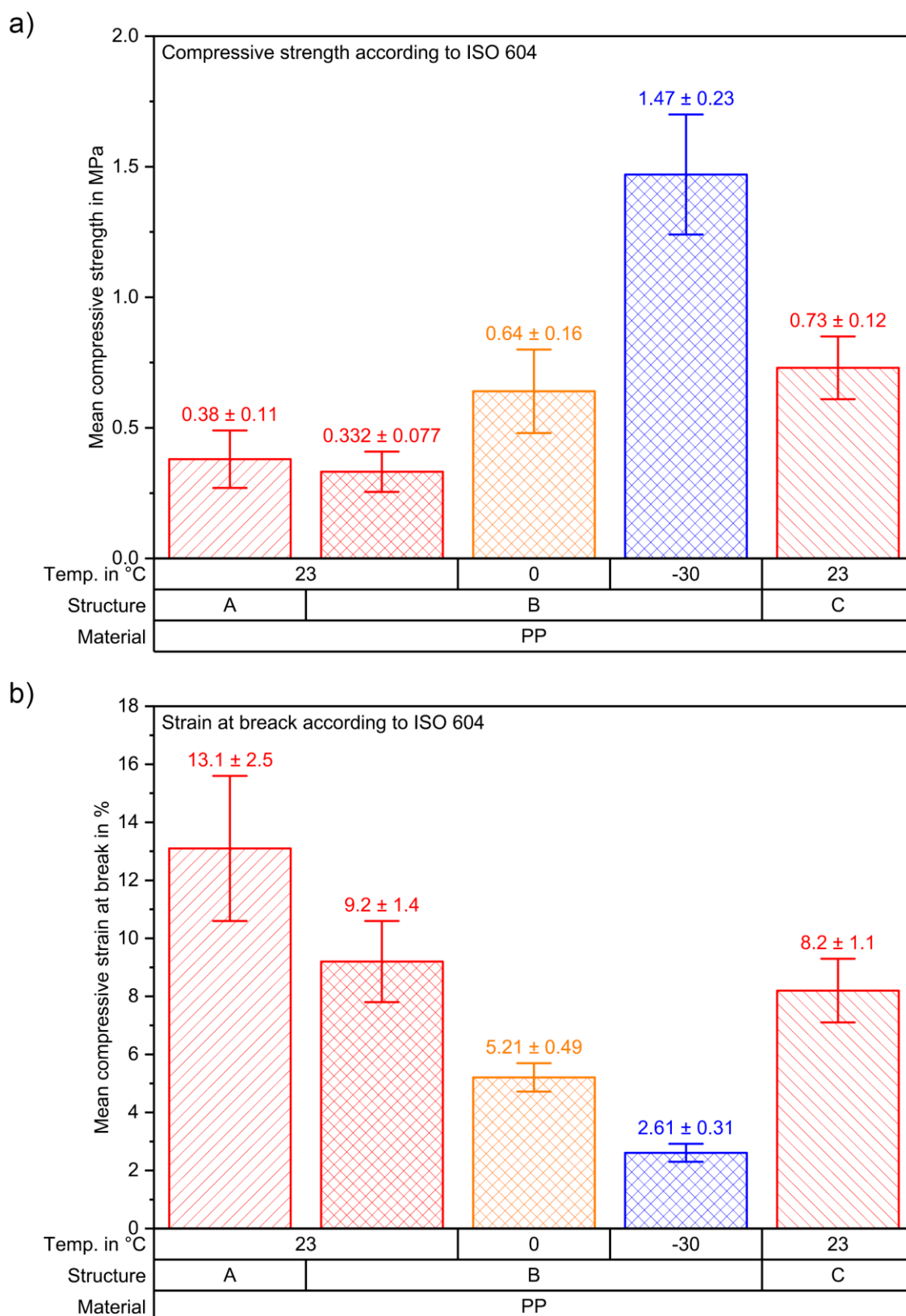


Figure 4.28: PP compression test results. a) Mean compressive strength, b) mean compressive strain at break.

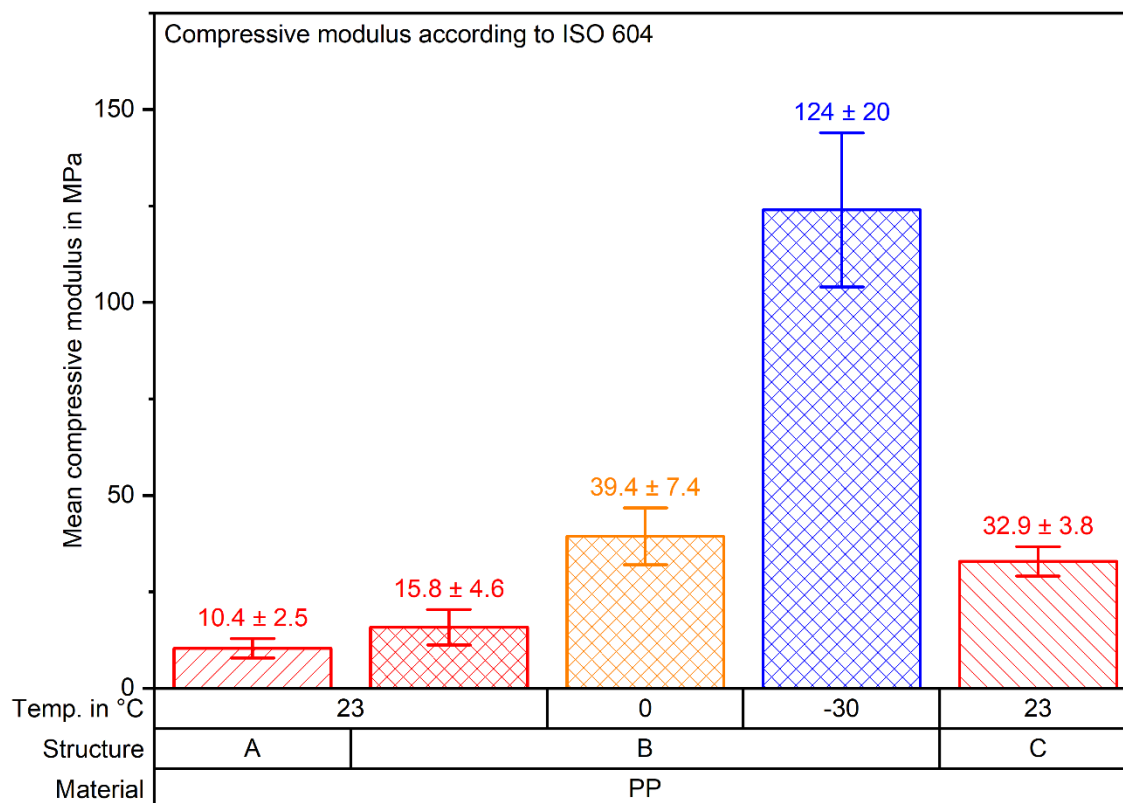


Figure 4.29: Mean compressive modulus for PP-VS-structures.

4.2.3 Material modeling

Analogue to the material models found for PA12, the previously described measurements were used to generate models for PP as well. The elastic parts of the material models are given by the Young's modulus (tensile based model) and flexural modulus (3PB based model). The plastic parts are modeled using the experimental approach given in section 3.8.1.

4.2.3.1 Tensile based yield stress – plastic strain model

Based on the tensile tests and the experimental approach given in section 3.8.1.1, the tensile based material models were calculated similar to the PA12 material models. First, the mean curves of the measured data were calculated (see section 3.8.1). For averaging only measurements with $\geq 50\%$ strain compared to the maximum strain tested were considered. Additionally, due to the observed necking behavior, the measurements ZL81 and ZL86 (horizontal, -30 °C) and ZS81 and ZS84 (vertical, -30 °C) were not considered.

Figure 4.30 shows the mean tensile stress strain curves for PP for all test conditions (orientation and temperature).

Based on the data, the yield stress – plastic strain was calculated using the equations in section 2.4.1.1. The calculated yield stress – plastic strain data and the logarithmic scaled input data for Abaqus are depicted in Figure 4.31.

Analogues to Table 4.4, Table 4.10 shows the valid Young’s modulus and Poisson’s ratio for the elastic part of the elastic-plastic material model for PP. Additionally, Table 7.3 and Table 7.4 in section 7.2 show the yield stress – plastic strain data for the plastic part.

Table 4.10: PP input data for elastic material models, based on tensile tests, in Abaqus.

Orientation	Temperature in °C	$E_{tens,valid}$ in MPa	ν_{valid}
horizontal	23	831	0.43
	0	1370	0.39
	-30	3040	0.32
vertical	23	825	0.42
	0	1430	0.39
	-30	3080	0.28

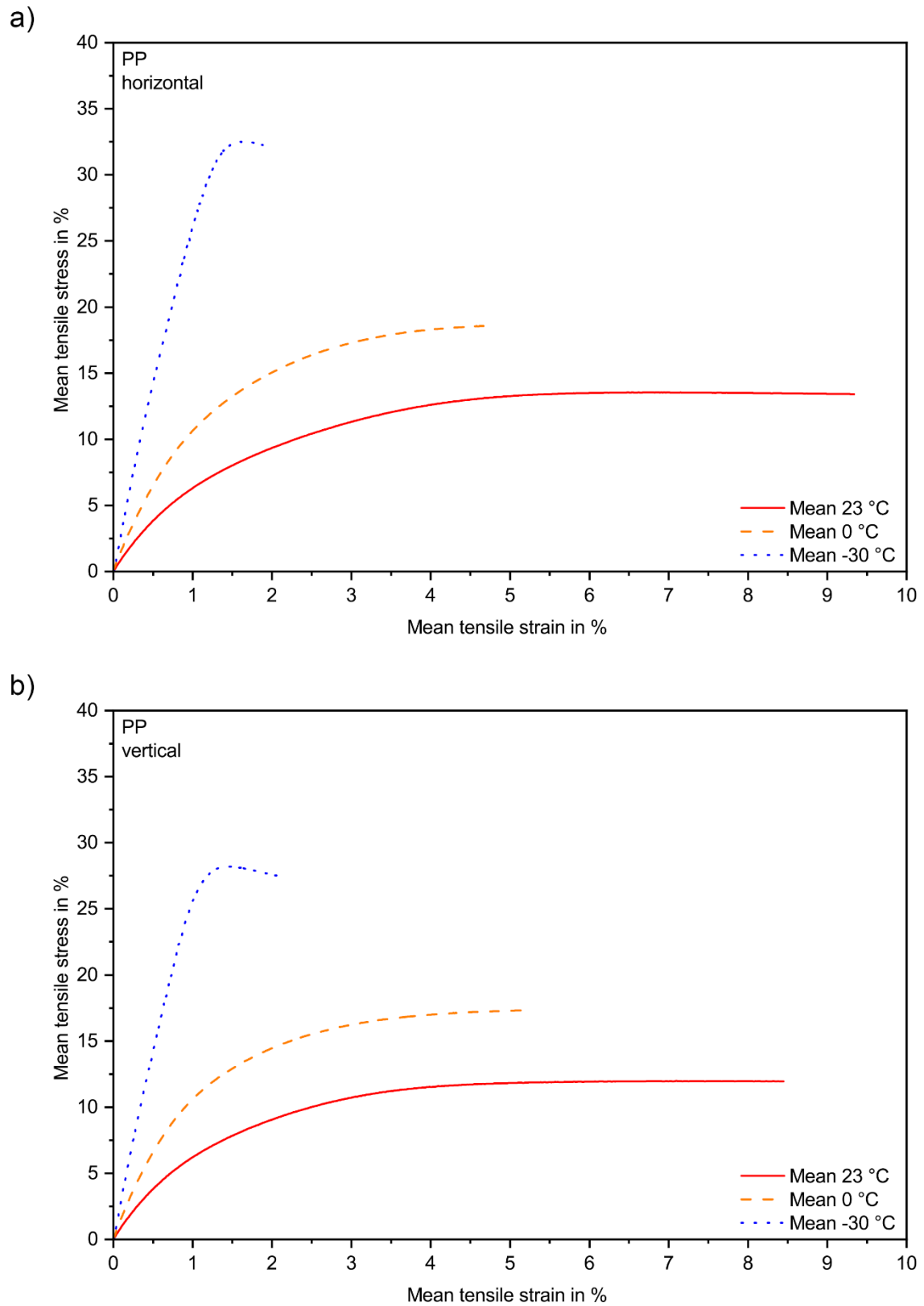


Figure 4.30: PP mean tensile stress – strain for a) horizontal and b) vertical print direction.

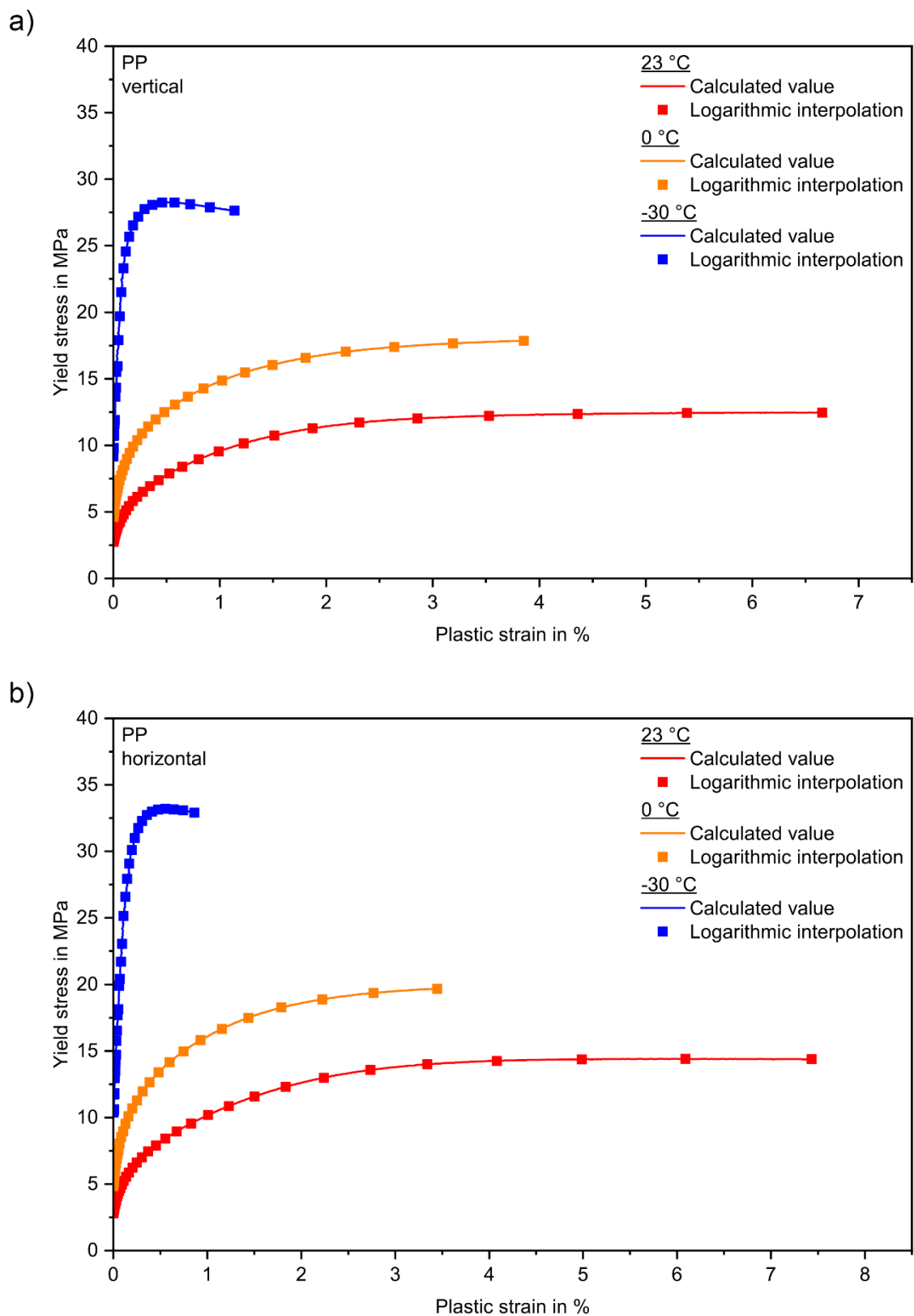


Figure 4.31: PP yield stress – plastic strain for a) horizontal and b) vertical print direction.

4.2.3.2 3PB tests-based Johnson-Cook optimization

Besides the tensile based material, models based on the 3PB experiments were generated using the 3PB test data shown in section 4.2.2.3 and the reverse engineering approach described in section 3.8.1.2. Like the tensile based material models, mean curves of all valid measurements for each test condition were calculated first. Only measurements with a flexural strain $\geq 50\%$ of the maximum strain were considered valid. Figure 4.32 shows the mean curves for each print orientation and temperature.

The Johnson-Cook parameter A again converges to the minimum set value. Due to the already described issue, that Abaqus is not able to handle small values for parameter A , no additional tests were performed with smaller A -values. The real test data and the 3PB simulations are in good agreement (see Figure 4.33). A summary of the input data for the elastic-plastic material model based on 3PB tests is shown in Table 4.11.

Table 4.11: PP input data for elastic-plastic material models, based on 3PB tests, in Abaqus.

Orientation	Temp.	elastic		plastic		
		$E_{3PB,valid}$ in MPa	ν_{valid}	JC – A	JC – B	JC – n
horizontal	23 °C	846	0.43	1.0	25.4	0.275
	0 °C	1437	0.39	1.0	172.0	0.358
	-30 °C	3128	0.32	1.0	254.0	0.420
vertical	23 °C	808	0.42	1.0	600.0	0.734
	0 °C	1375	0.39	1.0	761.0	0.663
	-30 °C	3012	0.28	1.0	421.0	0.500

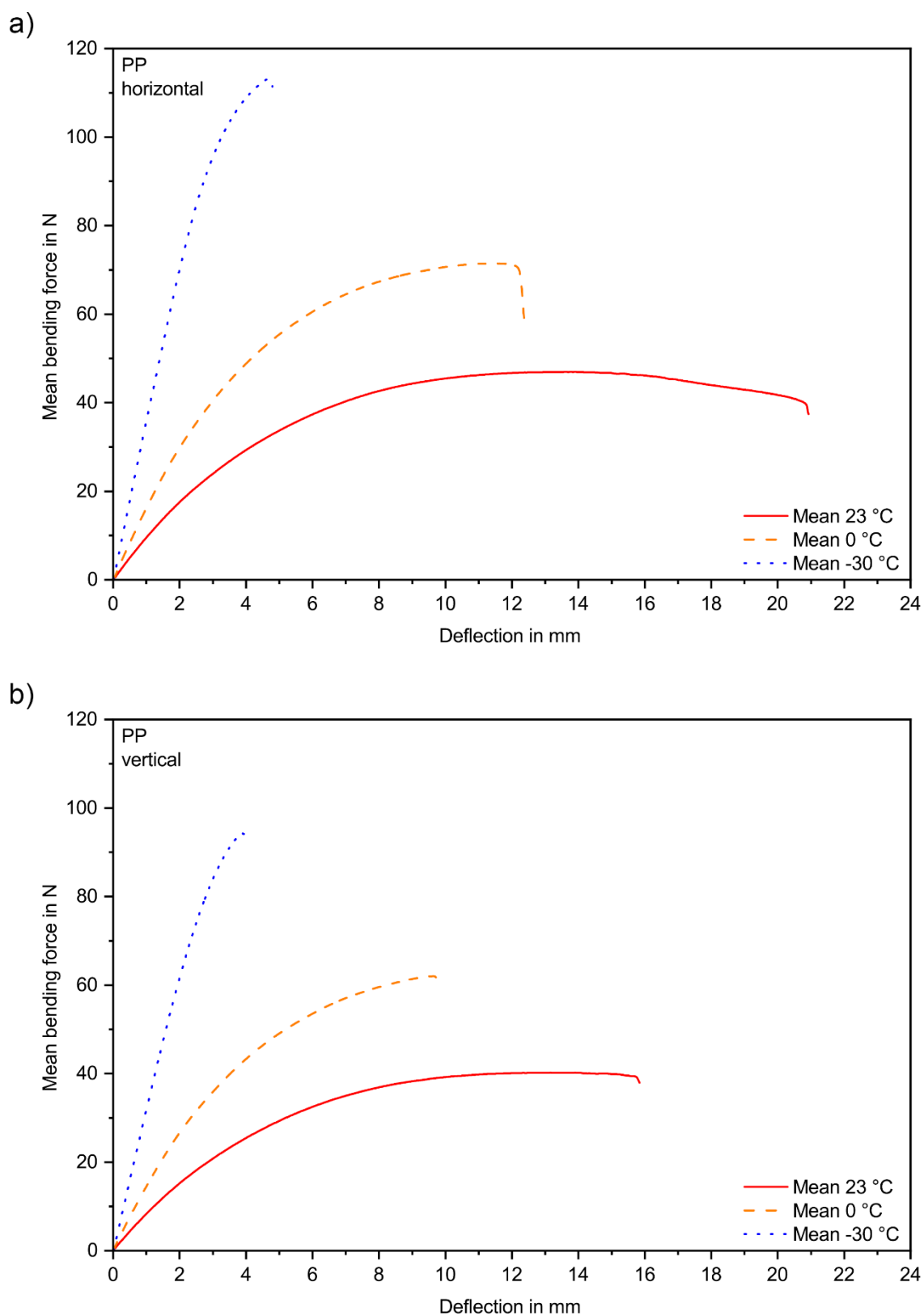


Figure 4.32: PP mean bending force – deflection of a) horizontal and b) vertical print direction.

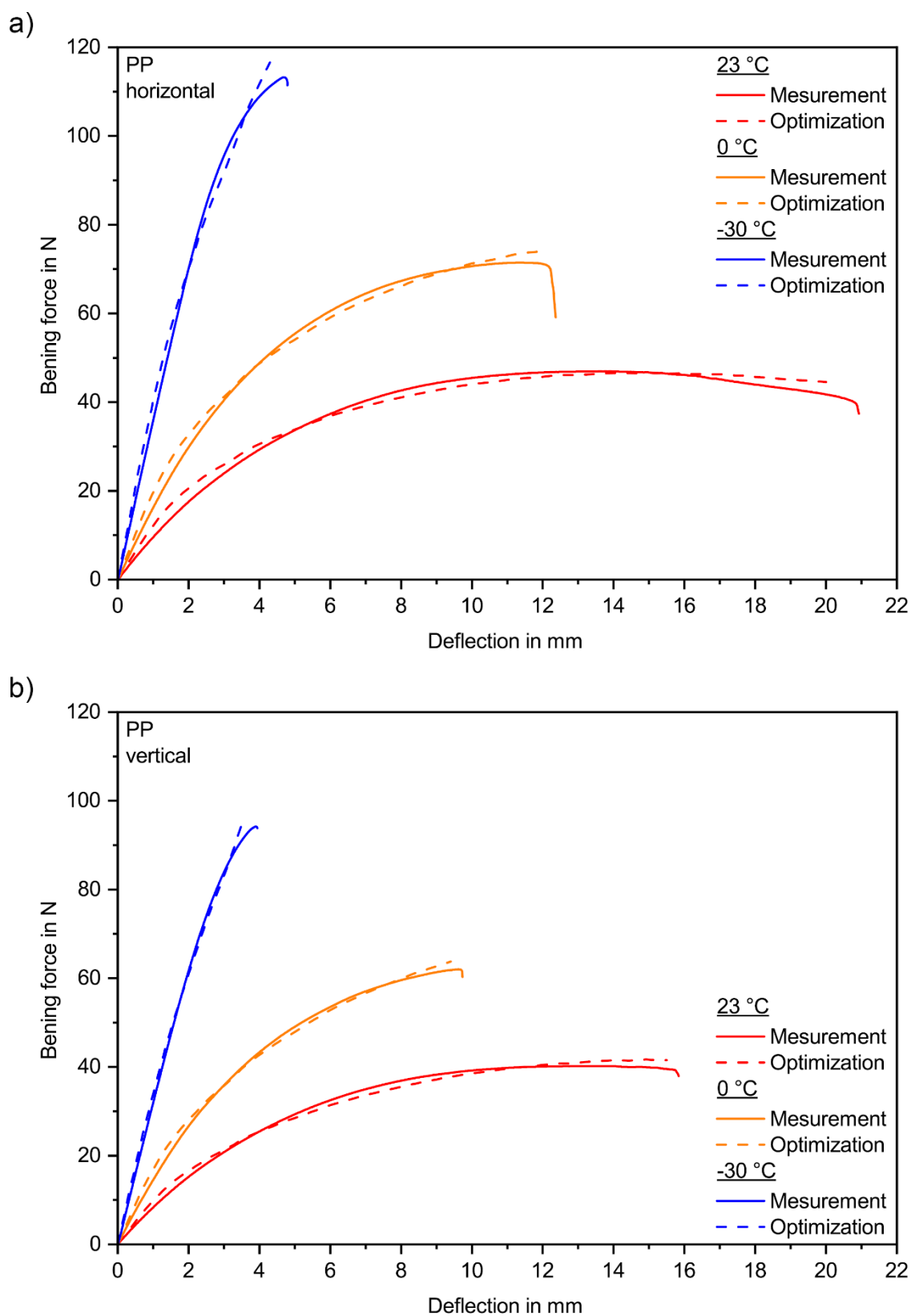


Figure 4.33: Comparison of measured and optimized bending force – deflection curves for PP with a) horizontal and b) vertical print direction.

4.2.4 VS-structure simulations and comparison

The compression simulations with PP material models were performed using the FEM models described in section 3.8.2.

Figure 4.34 shows the comparison of the nominal compressive stress – strain of the compression tests, simulations with pure elastic models and simulations using the generated elastic-plastic models. The elastic-plastic models lead to a significant improvement of the simulation results compared to pure elastic models. Especially for the simulations of structure A, structure B at 0 °C and -30 °C and structure C a good agreement with the compression tests can be seen. It must be mentioned that the simulation results are strongly depending on the generated real CAD models of the structures. Due to the issue that the geometric parameters can only be measured on the outside surfaces a deeper knowledge of the true geometric parameters cannot be gained. Therefore, the quality of the comparative simulations is limited.

Figure 4.35 shows the nominal compressive modulus of the simulations and the initial compression tests. In addition, the deviation margins based on the standard deviations of the Young's moduli or flexural moduli were added to the figure (as described in section 4.1.4). In general, the simulations are reacting stiffer than the compression tests. Overall, no significant difference between the simulations using tensile based and 3PB based material models can be seen. In total no difference between the material models based on horizontal and vertical print direction can be observed. Especially for the VS-structure B -30 °C the simulation results are in the same range as the compression test results. This can be explained by the increased stiffness of the material at -30 °C while testing below T_g .

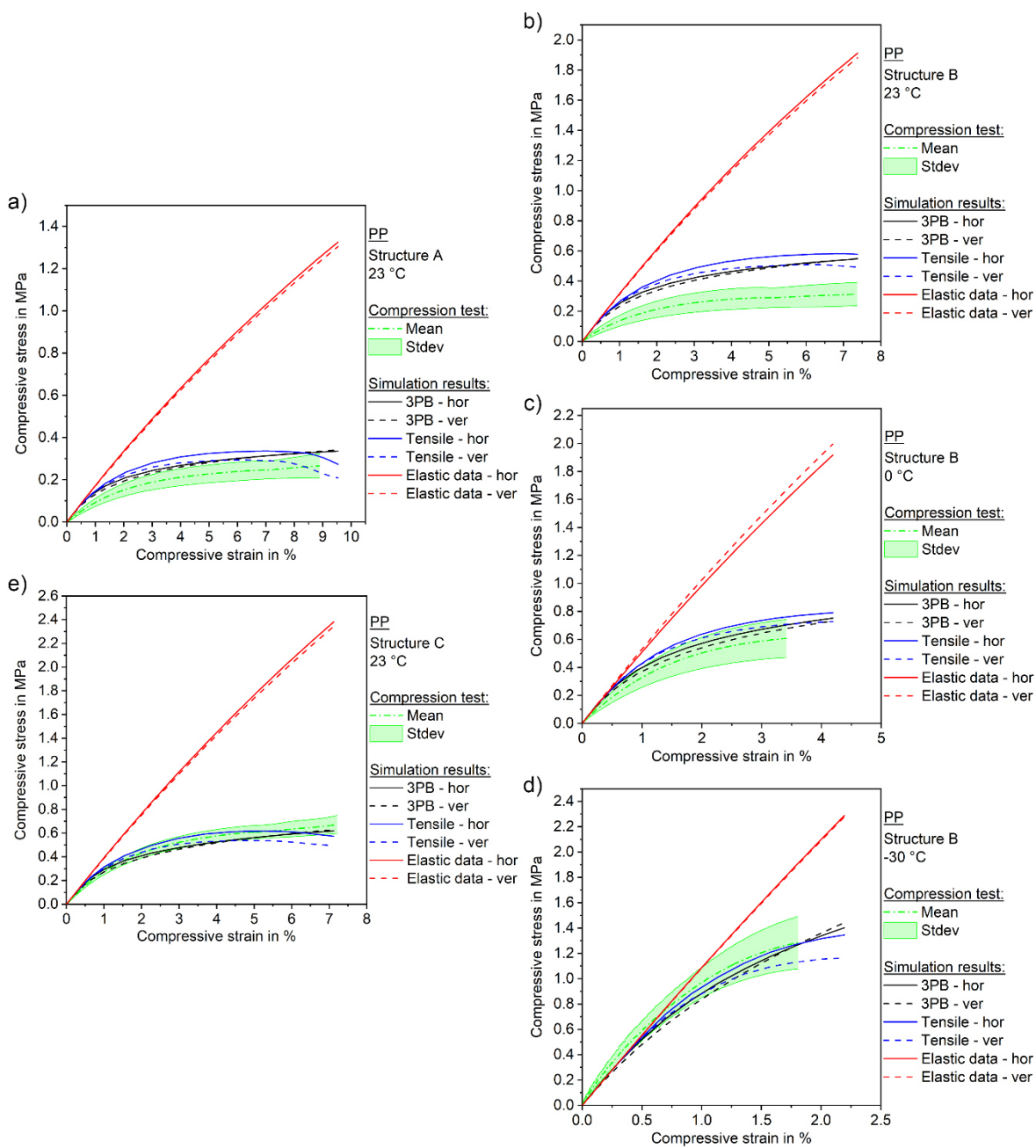


Figure 4.34: Compressive stress – strain of the VS-structures of PP with mean test data and simulation results for tensile and 3PB based material model in horizontal and vertical print direction. a) Structure A at 23 °C, b) structure B at 23 °C, c) structure B at 0 °C, d) structure B at -30 °C and e) structure C at 23 °C.

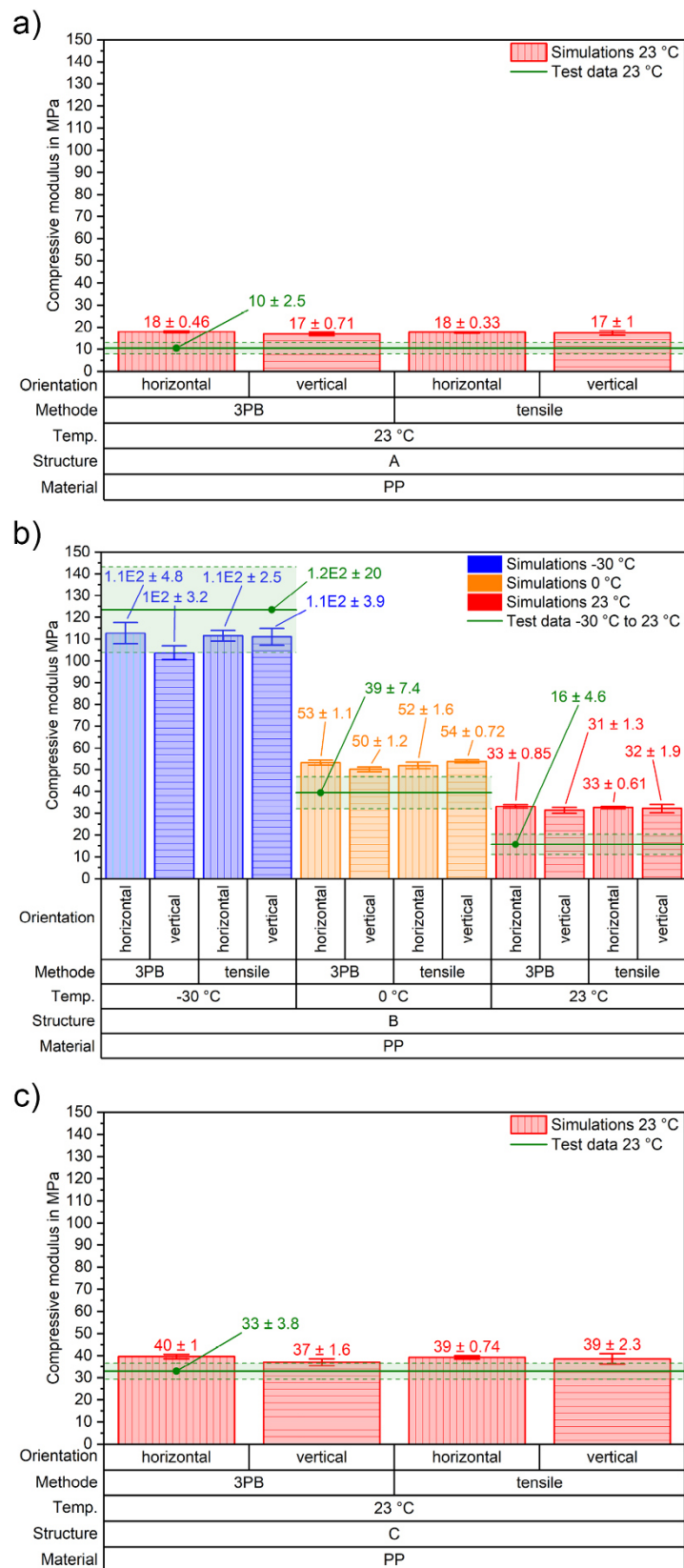


Figure 4.35: Comparison of the simulated compressive modulus for PP with horizontal and vertical print direction using tensile and 3PB based material models and the real compression test data for a) VS-structure A, b) VS-structure B and c) VS-structure C.

5 SUMMARY, CONCLUSION AND OUTLOOK

The goal of this study was to investigate the influence of different material modeling approaches on the quality of finite element simulations of mechanical metamaterials. Beyond that, the temperature dependency, and the influence of the print orientation was analyzed. For this, different material characterization methods (see section 3) were performed for Selective Laser Sintered Polyamide 12 and Polypropylene with specimens provided in horizontal and vertical print direction at $-30\text{ }^{\circ}\text{C}$, $0\text{ }^{\circ}\text{C}$ and $23\text{ }^{\circ}\text{C}$. Material models for FEM simulations based on the mechanical test data were generated. Additionally, full-scale compression tests of a variable stiffness mechanical metamaterial with different geometric parameters were done. Finally, simulations of the full-scale compression tests with material models based on the experiments were performed and compared to the compression tests.

During the sample production, the supplier of the TPP-VS-structures was not able to produce intact structures due to unpacking problems. TPP is a 3D printable thermoset which requires a two-step process for manufacturing. First the material is coarsely sintered to its desired shape followed by a secondary curing step. In between, the residual powder needs to be replaced by a temperature inherent salt to support the structure while curing. During the removal of the residual powder section of the VS structure broke of due to the reduced mechanical properties of the uncured material. Due to that, TPP was not considered for the ongoing discussion within this study.

After receiving the standard specimens of PP from the supplier, strong warpage was detected. To increase the quality of the specimens before testing, an annealing step was performed to reduce residual stresses (see section 3.2.2). Additionally, warpage was detected at the VS-structures, especially on the compression plates. While developing the annealing procedure, it was decided that annealing of the VS-structures is not feasible due to the risk of deforming the lattice structure. Therefore, only the compression plates were milled flat on a milling machine before testing (see section 3.2.2.2). Due to these different approaches (annealing for specimens, milling for structures) DSC measurements were performed to investigate the influence of annealing onto the morphology of PP. The measurements showed that no change in the morphology could be detected and therefore

the experimental approach with no temperature treatment for the VS-structure was feasible.

The DMA measurements (see section 4.1.1 and 4.2.1) showed a T_g of 55 °C and 5.3 °C for PA12 and PP, respectively. The measurement for PA12 proves that the glass transition range for the teste material is above the tested conditions within this study. Although, the data for PP showed that the T_g is within the tested temperature range. This results in the fact that additional polymer transitioning effects had to be considered when discussing the results for PP.

The mean Charpy impact test results for PA12 (see section 4.1.2.1) showed a decreasing impact strength for increasing temperature which shows a contrary trend than it is described in the literature [26, 28, 59, 60]. Moisture absorption at low temperatures inside the chamber is a possible explanation for this behavior. However, due to overlapping deviation margins no significant trend can be proven with this data. The mean Charpy impact strength for PP (see section 4.2.2.1) showed the expected trend with an increasing impact strength for increasing temperature. Besides that, the impact strength for vertical oriented specimens is significantly lower than for horizontal oriented specimens.

The mean tensile test results for PA12 (see section 4.1.2.2) and PP (see section 4.2.2.2) showed a similar trend for both materials. The characteristic test data showed a decreasing tensile strength and Young's modulus for increasing temperature. On the opposite side the tensile strain at break increased for increasing temperature. In addition, a reduction of the characteristic parameters for vertical printed specimens is observed compared to the horizontal printed specimens. Beyond that, a higher decrease of the Young's modulus and the tensile strength between -30 °C and 0 °C compared to 0 °C and 23 °C was detected.

The 3PB tests for PA12 (see section 4.1.2.3) and PP (see section 4.2.2.3) showed the same temperature dependency as the tensile tests. The mean flexural strength and the flexural modulus is decreasing and the flexural strain at break is increasing for increasing temperature. Although for the strain at break this clear trend was not that pronounced for the vertical printed PA12 due to overlapping deviation margins. Besides that, the comparison of horizontal and vertical print orientation showed the already observed trend that vertical print orientation leads to a reduction of the mechanical properties. Comparing

the strength and modulus values of the tensile tests for PP the 3PB measurements showed the same strong decrease for the flexural strength and modulus between -30 °C and 0 °C.

The full-scale compression tests of the VS-structures for PA12 (see section 4.1.2.4) and PP (see section 4.2.2.4) showed that structure A had the lowest and structure C the highest compressive modulus with structure B being in between the two. Comparing the temperature dependence for the measurements for structure B showed the same trend as for the standard measurements. The compressive strength and the compressive modulus were decreasing and the compressive strain at break was increasing for increasing temperature. Noticeable was the huge deviation for each parameter for both materials. The deviation leads to the assumption that due to the high complexity of the VS-structures the limitation of the print quality and reproducibility of the SLS process was reached.

Material modeling for the FEM simulations was based on the tensile and 3PB test data. To increase the simulation quality, elastic-plastic material models were generated. The tensile based elastic-plastic material model consists of the Young's modulus, Poisson's ratio, and yield stress – plastic strain data. Based on the equations shown in section 2.4.1.1 the materials models for PA12 (see section 4.1.3.1) and PP (see section 4.2.3.1) were generated for each temperature and print direction (see Table 3.12). Due to the non-linearity of the 3PB test, a reverse engineering approach was required to generate the plastic part of the material model. Therefore, an iterative parameter optimization processes was set up using a 3PB simulation model in Abaqus and the parameter optimization software LS-OPT. The material model in the bending simulation was based on the Johnson-Cook strain hardening model shown in section 2.4.1.2 with its simplification shown in Eq. 3.1. The elastic-plastic model based on the 3PB test data consists of the flexural modulus, Poisson's ratio, and the optimized Johnson-Cook parameters. The results of the optimization process for PA12 (see section 4.1.3.2) and PP (see section 4.2.3.2) showed that especially the Johnson-Cook parameter A was set by the optimization algorithm to $A = 1$. The parameter A describes the offset of the yield curve and therefore the onset of the plastic behavior. Due to numerical effects of deviations of the model regarding process details (friction, preload, etc.) a mismatch in the overall system stiffness might have been created. This then could have caused the optimization algorithm to compensate this by minimalizing the parameter A .

In general, the simulation quality can be significantly improved by using an elastic-plastic material model instead of a simple linear-elastic model. Besides that, the comparison of the compressive modulus showed that the simulation response was stiffer than the real compression tests for all measurements except the $-30\text{ }^{\circ}\text{C}$ of PP. Although for this measurement the simulated stiffness was lower than measured stiffness the result was within the deviation margin of the test results. In addition, the models based on vertical oriented tests (tensile and 3PB) showed a lower stiffness as the horizontal based models. Comparing the different material modeling approaches for PA12 showed that the 3PB based material models led to better results than the tensile based approaches.

Overall, the material model based on 3PB data with vertically oriented specimens showed the best results. Due to the bending deformation of the struts in the VS-structures, 3PB was already expected to be the most favorable test and material modeling method for this study. It is assumed that the built direction was along the z-axis of the SLS printer (see Figure 3.5). This would lead to layer boundaries under a specific angle (based on the geometric parameters of the unit cell) compared to the load direction of the bending struts of the structure. Comparing the strict distinction in horizontal and vertical for material modeling this would lead to a mix directional orientation of the bending struts in the VS-structures. Based on that assumption, the study showed that this mix directional orientation can be better described by the vertical oriented material models.

To allow for more materials to be compared as VS-structures, a simpler VS-structure with bigger dimensions, especially the distance between the cubes D and the thickness of the struts T (see section 3.1.2) could be designed. This coarser structure might improve the unpacking during the processing of TPP, resulting in the possibility of comparing a 3D printable thermoset with standard SLS thermoplastic materials. Additionally, instrumented Charpy tests could be performed, to gain a deeper insight into the impact behavior of SLS printed materials. Within this study no local stresses and especially stress concentrations were evaluated during the FEM simulations of the VS-structures. Based on the chosen mesh with different element types (for bending struts and cubes) a detailed discussion on the resulting stresses was not possible. A uniform mesh would have led to a significant increase of the simulation time and was omitted due to the high number of required simulations.

Besides that, the evaluation of stresses might be required for optimizing the VS-structures for real device applications.

6 LITERATURE

- [1] Kshetrimayum, R.S.: A brief intro to metamaterials, *IEEE Potentials* 23 (5), 2005, pp. 44–46
- [2] Fleisch, M.; Thalhamer, A.; Meier, G.; Fuchs, P.F.; Pinter, G.; Schlögl, S.; Berer, M.: Asymmetric chiral and antichiral mechanical metamaterials with tunable Poisson's ratio, *APL Materials* 10 (6), 2022, pp. 61105
- [3] Yu, X.; Zhou, J.; Liang, H.; Jiang, Z.; Wu, L.: Mechanical metamaterials associated with stiffness, rigidity and compressibility: A brief review, *Progress in Materials Science* 94, 2018, pp. 114–173
- [4] Evans, K.E.; Alderson, A.: Auxetic Materials: Functional Materials and Structures from Lateral Thinking!, *Advanced Materials* 12 (9), 2000, pp. 617–628
- [5] Schaedler, T.A.; Jacobsen, A.J.; Torrents, A.; Sorensen, A.E.; Lian, J.; Greer, J.R.; Valdevit, L.; Carter, W.B.: Ultralight metallic microlattices, *Science (New York, N.Y.)* 334 (6058), 2011, pp. 962–965
- [6] Jeong, H.Y.; An, S.-C.; Seo, I.C.; Lee, E.; Ha, S.; Kim, N.; Jun, Y.C.: 3D printing of twisting and rotational bistable structures with tuning elements, *Scientific reports* 9 (1), 2019, pp. 324
- [7] Fleisch, M.; Thalhamer, A.; Meier, G.; Raguž, I.; Fuchs, P.F.; Pinter, G.; Schlögl, S.; Berer, M.: Functional mechanical metamaterial with independently tunable stiffness in the three spatial directions, *Materials Today Advances* 11, 2021, pp. 100155
- [8] Lu, C.; Hsieh, M.; Huang, Z.; Zhang, C.; Lin, Y.; Shen, Q.; Chen, F.; Zhang, L.: Architectural Design and Additive Manufacturing of Mechanical Metamaterials: A Review, *Engineering* 17, 2022, pp. 44–63
- [9] Godec, D.: A Guide to Additive Manufacturing, *Springer Tracts in Additive Manufacturing Ser*, Springer International Publishing AG, Cham, 2022
- [10] Surjadi, J.U.; Gao, L.; Du, H.; Li, X.; Xiong, X.; Fang, N.X.; Lu, Y.: Mechanical Metamaterials and Their Engineering Applications, *Advanced Engineering Materials* 21 (3), 2019, pp. 1800864

-
- [11] Ozbay, E.: The Magical World of Photonic Metamaterials, *Optics and Photonics News* 19 (11), 2008, pp. 22
- [12] Cummer, S.A.; Christensen, J.; Alù, A.: Controlling sound with acoustic metamaterials, *Nature Reviews Materials* 1 (3), 2016, pp. 2059
- [13] Grimberg, R.: Electromagnetic metamaterials, *Materials Science and Engineering: B* 178 (19), 2013, pp. 1285–1295
- [14] Wang, J.; Dai, G.; Huang, J.: Thermal Metamaterial: Fundamental, Application, and Outlook, *iScience* 23 (10), 2020, pp. 101637
- [15] Kuder, I.K.; Arrieta, A.F.; Raither, W.E.; Ermanni, P.: Variable stiffness material and structural concepts for morphing applications, *Progress in Aerospace Sciences* 63, 2013, pp. 33–55
- [16] Gebhardt, A.; Kessler, J.; Thurn, L.: 3D-Drucken, Grundlagen und Anwendungen des Additive Manufacturing (AM), 2. Ed., Hanser, München, 2016
- [17] ISO/ASTM 52900:2021: Additive Fertigung - Grundlagen - Terminologie
- [18] Deckard, C.R.: Method and apparatus for producing parts by selective sintering, US4863538A, 1986
- [19] Gebhardt, A.: Additive Fertigungsverfahren, CARL HANSER Verlag GMBH &, [Place of publication not identified], 2016
- [20] Kruth, J.-P.; Mercelis, P.; van Vaerenbergh, J.; Froyen, L.; Rombouts, M.: Binding mechanisms in selective laser sintering and selective laser melting, *Rapid Prototyping Journal* 11 (1), 2005, pp. 26–36
- [21] Bonten, C.: Kunststofftechnik, Einführung und Grundlagen, 2. Ed., Hanser, München, 2016
- [22] Grellmann, W.; Seidler, S.: Polymer testing, 3. Ed., Hanser, München, 2011
- [23] EN ISO 179-1:2010: Plastics - Determination of Charpy impact properties, Part 1: Non-instrumented impact test
- [24] Saechtling, H.; Baur, E.: Saechtling-Kunststoff-Taschenbuch, Neu: mit eBook zum Download und Glossary in 6 Sprachen auf CD, 30. Ed., Hanser, München, 2007

- [25] Argon, A.S.: The physics of deformation and fracture of polymers, Cambridge Solid State Science Series, Cambridge University Press, Cambridge, 2013
- [26] Hellerich, W.; Harsch, G.; Haenle, S.: Werkstoff-Führer Kunststoffe, Eigenschaften, Prüfungen, Kennwerte, 10. Ed., Carl Hanser Fachbuchverlag, s.l., 2010
- [27] EN ISO 527-2:1996: Plastics - Determination of tensile properties, Part 2: Test conditions for moulding and extrusion plastics
- [28] Ehrenstein, G.W.: Polymer-Werkstoffe, Struktur - Eigenschaften - Anwendung, 3. Ed., Hanser, München, 2011
- [29] Meyers, M.A.; Chawla, K.K.: Mechanical behavior of materials, 2. Ed., Cambridge University Press, Cambridge, 2010
- [30] Elsner, P.; Eyerer, P.; Hirth, T.: DOMININGHAUS - Kunststoffe, Eigenschaften und Anwendungen, VDI-Buch, 8. Ed., Springer, Dordrecht, 2011
- [31] EN ISO 178:2010: Plastics - Determination of flexural properties
- [32] Heine, B.: Werkstoffprüfung, Ermittlung von Werkstoffeigenschaften, 2. Ed., Hanser Verlag, München, 2011
- [33] EN ISO 604:2003: Plastics - Determination of compressive properties
- [34] Steinke, P.: Finite-Elemente-Methode, Rechnergestützte Einführung, 4. Ed., Springer Berlin Heidelberg, Berlin, Heidelberg, 2012
- [35] Bathe, K.-J.: Finite element procedures, Prentice Hall, Englewood Cliffs, NJ, 1996
- [36] Klein, B.: FEM, Grundlagen und Anwendungen der Finite-Element-Methode im Maschinen- und Fahrzeugbau, SpringerLink Bücher, 9. Ed., Vieweg+Teubner Verlag, Wiesbaden, 2012
- [37] KORTE, S.: FEM, Zur Berechnung von Kunststoff- und Elastomerbauteilen, CARL HANSER Verlag GMBH &, [Place of publication not identified], 2011
- [38] Bergstrom, J.: Mechanics of solid polymers, Theory and computational modeling, William Andrew is an imprint of Elsevier, Amsterdam, 2015

- [39] ABAQUS Inc.: ABAQUS Online Documentation Version 6.6-1, 4.2.1 Plasticity models: general discussion, 2006, <https://classes.engineering.wustl.edu/2009/spring/mase5513/abaqus/docs/v6.6/books/stm/default.htm?startat=ch04s02ath101.html> (retrieved on: 22.07.2023)
- [40] ABAQUS Inc.: ABAQUS Online Documentation Version 6.6-1, 17.2.1 Linear elastic behavior, 2006, <https://classes.engineering.wustl.edu/2009/spring/mase5513/abaqus/docs/v6.6/books/usb/default.htm?startat=pt05ch18s02abm21.html> (retrieved on: 22.07.2023)
- [41] ABAQUS Inc.: ABAQUS Online Documentation Version 6.6-1, 18.2.1 Classical metal plasticity, 2006, <https://classes.engineering.wustl.edu/2009/spring/mase5513/abaqus/docs/v6.6/books/usb/default.htm?startat=pt05ch18s02abm21.html> (retrieved on: 22.07.2023)
- [42] ABAQUS Inc.: ABAQUS Online Documentation Version 6.6-1, 18.2.7 Johnson-Cook plasticity, Johnson-Cook hardening, 2006, <https://classes.engineering.wustl.edu/2009/spring/mase5513/abaqus/docs/v6.6/books/usb/default.htm?startat=pt05ch18s02abm21.html> (retrieved on: 08.06.2023)
- [43] Pletz, M.: Material Modeling of Polymer and Composite Materials, General principles, elastic-plastic and viscoelastic material models, Lecture notes, SS2022
- [44] Ward, I.M.: Mechanical properties of solid polymers, Wiley-Interscience, London, 1971
- [45] ABAQUS Inc.: ABAQUS Online Documentation Version 6.6-1, 21.1.1 Element library: overview, 2006, <https://classes.engineering.wustl.edu/2009/spring/mase5513/abaqus/docs/v6.6/books/usb/default.htm?startat=pt06ch21s01abo21.html> (retrieved on: 20.07.2023)
- [46] ABAQUS Inc.: ABAQUS Online Documentation Version 6.6-1, 22.1.1 Solid (continuum) elements, 2006, <https://classes.engineering.wustl.edu/2009/spring/mase5513/abaqus/docs/v6.6/books/usb/default.htm?startat=pt06ch22s01ael02.html> (retrieved on: 20.07.2023)
- [47] ALM - Advanced Laser Materials: PA 650, Material datasheet, 2023

- [48] Lehmann&Voss&Co. KG: LUVOSINT PP 9703, Product datasheets, 2023
- [49] TIGER Coatings GmbH & Co KG: TIGITAL® 3D-Set TPP, Product datasheets, 2023
- [50] Chaichanawong, J.; Thongchuea, C.; Areerat, S.: Effect of moisture on the mechanical properties of glass fiber reinforced polyamide composites, *Advanced Powder Technology* 27 (3), 2016, pp. 898–902
- [51] van Rossum, G.; Drake, F.L., JR.: Python reference manual, 1995
- [52] Ferry, J.D.; Landel, R.F.: Molecular friction coefficients in polymers and their temperature dependence, *Kolloid-Zeitschrift* 148 (1-2), 1956, pp. 1–6
- [53] Fox, M.: Polymer Tribology, *Lube-tech* (106), 2016, pp. 2–4
- [54] Muhammad, D.; Asaduzzaman, M.: Friction and Wear of Polymer and Composites, In: Hu N. (Ed.): *Composites and Their Properties*, IntechOpen, Erscheinungsort nicht ermittelbar, 2012
- [55] Nar, K.; Majewski, C.; Lewis, R.: Evaluating the effect of solid lubricant inclusion on the friction and wear properties of Laser Sintered Polyamide-12 components, *Wear* 522, 2023, pp. 204873
- [56] Sinha, S.K.; Briscoe, B.J.: *Polymer tribology*, Imperial College Press, London, Singapore, 2009
- [57] ABAQUS Inc.: ABAQUS Online Documentation Version 6.6-1, 22.1.3 Two-dimensional solid element library, Element types - Plane strain elements, 2006, <https://classes.engineering.wustl.edu/2009/spring/mase5513/abaqus/docs/v6.6/books/usb/default.htm?startat=pt06ch22s01ael02.html> (retrieved on: 07.06.2023)
- [58] ABAQUS Inc.: ABAQUS Online Documentation Version 6.6-1, 22.1.4 Three-dimensional solid element library, Element types - Stress/displacement elements, 2006, <https://classes.engineering.wustl.edu/2009/spring/mase5513/abaqus/docs/v6.6/books/usb/default.htm?startat=pt06ch22s01ael03.html> (retrieved on: 09.06.2023)
- [59] Han, Y.; Lach, R.; Grellmann, W.: The Charpy impact fracture behaviour in ABS materials, *Die Angewandte Makromolekulare Chemie* 270 (1), 1999, pp. 13–21

- [60] Böhning, M.; Niebergall, U.; Adam, A.; Stark, W.: Influence of biodiesel sorption on temperature-dependent impact properties of polyethylene, *Polymer Testing* 40, 2014, pp. 133–142
- [61] Gibson, I.; Shi, D.: Material properties and fabrication parameters in selective laser sintering process, *Rapid Prototyping Journal* 3 (4), 1997, pp. 129–136
- [62] Calignano, F.; Giuffrida, F.; Galati, M.: Effect of the build orientation on the mechanical performance of polymeric parts produced by multi jet fusion and selective laser sintering, *Journal of Manufacturing Processes* 65, 2021, pp. 271–282
- [63] Caulfield, B.; McHugh, P.E.; Lohfeld, S.: Dependence of mechanical properties of polyamide components on build parameters in the SLS process, *Journal of Materials Processing Technology* 182 (1-3), 2007, pp. 477–488
- [64] Menges, G.: *Werkstoffkunde Kunststoffe, Studentexte Kunststofftechnik*, 5. Ed., Hanser, München, 2005
- [65] Kono, R.; Yoshizaki, H.: Viscoelastic Properties of Polyvinyl-i-Butyl Ethers at High Frequencies, *Japanese Journal of Applied Physics* 12 (3), 1973, pp. 445–457
- [66] Robertson, C.G.; Bogoslovov, R.; Roland, C.M.: Effect of structural arrest on Poisson's ratio in nanoreinforced elastomers, *Physical review. E, Statistical, nonlinear, and soft matter physics* 75 (5 Pt 1), 2007, pp. 51403
- [67] Yang, L.; Yang, L.; Lowe, R.L.: A viscoelasticity model for polymers: Time, temperature, and hydrostatic pressure dependent Young's modulus and Poisson's ratio across transition temperatures and pressures, *Mechanics of Materials* 157, 2021, pp. 103839
- [68] Marsavina, L.; Stoia, D.I.; Linul, E.: Mixed modes crack paths in SCB specimens obtained via SLS, *Procedia Structural Integrity* 39, 2022, pp. 801–807

7 APPENDIX

7.1 Yield stress – plastic strain data PA12

Table 7.1: Tensile based yield stress – plastic strain data for PA12 with horizontal print orientation.

-30 °C		0 °C		23 °C	
Plastic strain	Yield stress in MPa	Plastic strain	Yield stress in MPa	Plastic strain	Yield stress in MPa
0	15.06729	0	6.54615	0	5.82581
6.06946E-6	15.06729	8.20433E-7	6.54615	3.21112E-7	5.82581
7.11461E-6	15.07297	1.00125E-6	6.54615	4.10831E-7	5.82581
8.33974E-6	15.07832	1.22191E-6	6.54615	5.25617E-7	5.82581
9.77582E-6	15.0834	1.49121E-6	6.54615	6.72474E-7	5.82581
1.14592E-5	15.08936	1.81985E-6	6.54615	8.60364E-7	5.82581
1.34325E-5	15.09634	2.22093E-6	6.54615	1.10075E-6	5.82581
1.57455E-5	15.10452	2.7104E-6	6.54615	1.4083E-6	5.82581
1.84568E-5	15.11411	3.30774E-6	6.54615	1.80178E-6	5.82581
2.16351E-5	15.12536	4.03673E-6	6.54615	2.3052E-6	5.82581
2.53606E-5	15.13854	4.92638E-6	6.54648	2.94927E-6	5.82581
2.97276E-5	15.15399	6.0121E-6	6.54746	3.77329E-6	5.82581
3.48467E-5	15.1721	7.33711E-6	6.54865	4.82755E-6	5.82581
4.08472E-5	15.54971	8.95412E-6	6.5501	6.17637E-6	5.82581
4.7881E-5	15.60604	1.09275E-5	6.80762	7.90205E-6	5.82581
5.61261E-5	16.73029	1.33358E-5	6.85504	1.01099E-5	6.27859
6.57909E-5	16.75962	1.62749E-5	6.86751	1.29346E-5	6.56537
7.71199E-5	16.79401	1.98617E-5	6.88272	1.65485E-5	6.72689
9.03998E-5	16.83431	2.4239E-5	6.90129	2.11722E-5	6.74999
1.05967E-4	16.92097	2.9581E-5	6.92395	2.70877E-5	6.87356
1.24214E-4	17.75144	3.61004E-5	7.87129	3.4656E-5	6.96886
1.45603E-4	18.0717	4.40565E-5	7.94903	4.43389E-5	7.18597
1.70676E-4	18.31609	5.37661E-5	8.78433	5.67272E-5	7.46614
2.00066E-4	18.90288	6.56155E-5	8.95728	7.25768E-5	7.79899
2.34517E-4	19.58167	8.00765E-5	9.3712	9.28547E-5	8.16676
2.749E-4	20.28712	9.77245E-5	10.07067	1.18798E-4	8.7974
3.22237E-4	20.71002	1.19262E-4	11.0602	1.51991E-4	9.29595
3.77726E-4	21.86502	1.45546E-4	11.50346	1.94457E-4	10.29341
4.4277E-4	22.40295	1.77623E-4	12.25423	2.48788E-4	11.11933
5.19014E-4	23.27241	2.16769E-4	13.70737	3.183E-4	11.95859
6.08387E-4	24.35846	2.64542E-4	14.35278	4.07233E-4	13.24242
7.1315E-4	25.50394	3.22844E-4	15.6712	5.21013E-4	14.29908
8.35953E-4	27.2043	3.93996E-4	17.15522	6.66585E-4	15.88773
9.79903E-4	28.46656	4.80828E-4	19.02761	8.52829E-4	17.42292
0.00115	29.78725	5.86798E-4	20.37079	0.00109	19.151
0.00135	31.75386	7.16122E-4	22.2721	0.0014	21.01258
0.00158	33.61339	8.73947E-4	24.25065	0.00179	22.96128
0.00185	35.60227	0.00107	26.39444	0.00229	24.91304
0.00217	37.36376	0.0013	28.61453	0.00292	26.83398
0.00254	39.37966	0.00159	31.05005	0.00374	28.79976
0.00298	41.0281	0.00194	33.29394	0.00479	30.6093
0.00349	42.94744	0.00237	35.51602	0.00612	32.32908
0.00409	44.66429	0.00289	37.82157	0.00783	33.93741
0.0048	46.28802	0.00352	40.0227	0.01002	35.42258
0.00563	47.81089	0.0043	42.12769	0.01282	36.86379
0.00659	49.35903	0.00525	44.0035	0.0164	38.29969
0.00773	50.73486	0.0064	45.72692	0.02099	39.75222
0.00906	51.92846	0.00782	47.26572	0.02685	41.25952
0.01062	53.06328	0.00954	48.60506	0.03435	42.80119
0.01245	54.13526	0.01164	49.74128	0.04395	44.31116
0.01459	54.99978	0.01421	50.73367	0.05623	45.63136

Table 7.2: Tensile based yield stress – plastic strain data for PA12 with vertical print orientation.

-30 °C		0 °C		23 °C	
Plastic strain	Yield stress in MPa	Plastic strain	Yield stress in MPa	Plastic strain	Yield stress in MPa
0	10.52395	0	6.66129	0	5.6258
6.72689E-6	10.52395	9.37422E-6	6.66129	5.33869E-7	5.6258
7.62789E-6	10.52395	1.05119E-5	6.66129	6.44759E-7	5.62788
8.64956E-6	10.52395	1.17876E-5	6.66129	7.78681E-7	5.63039
9.80808E-6	10.52395	1.32182E-5	6.66129	9.4042E-7	5.63342
1.11218E-5	10.52395	1.48223E-5	6.66129	1.13575E-6	5.63708
1.26114E-5	10.52395	1.66212E-5	6.66129	1.37166E-6	5.6415
1.43006E-5	10.52395	1.86383E-5	6.66129	1.65657E-6	5.64683
1.6216E-5	10.52395	2.09002E-5	6.95165	2.00065E-6	5.65328
1.83879E-5	10.52395	2.34367E-5	6.96018	2.41621E-6	5.66106
2.08508E-5	10.52395	2.6281E-5	6.96974	2.91808E-6	5.67047
2.36435E-5	10.52395	2.94705E-5	6.98046	3.52419E-6	5.68182
2.68103E-5	10.52395	3.3047E-5	6.99248	4.2562E-6	5.69553
3.04013E-5	10.52395	3.70576E-5	7.87886	5.14025E-6	5.71209
3.44732E-5	10.52395	4.15549E-5	7.91386	6.20793E-6	5.73209
3.90905E-5	10.52395	4.6598E-5	7.95088	7.49737E-6	5.96477
4.43263E-5	10.52395	5.22532E-5	7.98927	9.05465E-6	5.98824
5.02633E-5	10.52395	5.85947E-5	8.33583	1.09354E-5	6.01658
5.69955E-5	10.52395	6.57057E-5	8.8218	1.32068E-5	6.05082
6.46294E-5	10.52395	7.36798E-5	8.84517	1.59499E-5	6.10362
7.32859E-5	10.69304	8.26216E-5	9.09356	1.92629E-5	6.46433
8.31017E-5	15.23767	9.26486E-5	9.25589	2.3264E-5	6.47575
9.42323E-5	17.3292	1.03892E-4	9.27795	2.80961E-5	6.48954
1.06854E-4	17.33853	1.16501E-4	10.15823	3.39319E-5	6.5062
1.21166E-4	17.34912	1.30639E-4	10.38779	4.09799E-5	6.52632
1.37394E-4	17.36111	1.46494E-4	10.75721	4.94918E-5	6.84353
1.55797E-4	17.37472	1.64272E-4	11.07188	5.97718E-5	7.00635
1.76664E-4	17.39015	1.84209E-4	11.12139	7.21869E-5	7.37626
2.00326E-4	17.68865	2.06564E-4	12.22016	8.71808E-5	7.6538
2.27158E-4	19.80634	2.31633E-4	12.49161	1.05289E-4	7.73402
2.57583E-4	21.10722	2.59744E-4	12.96066	1.27159E-4	8.20941
2.92084E-4	21.15922	2.91267E-4	13.71668	1.53571E-4	8.72153
3.31205E-4	21.73789	3.26615E-4	14.40818	1.85469E-4	9.12613
3.75567E-4	22.72408	3.66253E-4	15.07058	2.23992E-4	9.64263
4.2587E-4	23.3799	4.10701E-4	15.68528	2.70518E-4	10.28182
4.82911E-4	24.36871	4.60544E-4	16.50856	3.26707E-4	10.80885
5.47591E-4	24.95477	5.16436E-4	17.27838	3.94567E-4	11.65411
6.20935E-4	25.64315	5.79111E-4	18.02551	4.76522E-4	12.47917
7.04103E-4	26.58632	6.49392E-4	19.20036	5.755E-4	13.34903
7.9841E-4	27.48216	7.28202E-4	20.05014	6.95037E-4	14.39323
9.05348E-4	29.00331	8.16577E-4	20.99881	8.39403E-4	15.45027
0.00103	29.76818	9.15677E-4	21.86499	0.00101	16.66751
0.00116	30.95759	0.00103	22.98088	0.00122	17.96959
0.00132	32.13322	0.00115	24.02898	0.00148	19.18914
0.0015	33.2672	0.00129	25.14354	0.00179	20.61427
0.0017	34.53689	0.00145	26.35412	0.00216	21.98574
0.00192	35.70925	0.00162	27.74826	0.0026	23.42297
0.00218	37.23086	0.00182	28.88156	0.00315	24.82782
0.00247	38.5087	0.00204	29.98755	0.0038	26.19382
0.00281	40.03157	0.00229	31.21213	0.00459	27.53748
0.00318	41.49932	0.00257	32.35996	0.00554	28.84431

7.2 Yield stress – plastic strain data PP

Table 7.3: Tensile based yield stress – plastic strain data for PP with horizontal print orientation.

-30 °C		0 °C		23 °C	
Plastic strain	Yield stress in MPa	Plastic strain	Yield stress in MPa	Plastic strain	Yield stress in MPa
0	10.3608	0	4.84768	0	2.79781
6.23127E-6	10.3608	7.7078E-7	4.84768	4.15263E-6	2.79781
7.22225E-6	10.36583	9.59036E-7	4.84768	5.07126E-6	2.79781
8.37082E-6	10.37164	1.19327E-6	4.84768	6.1931E-6	2.79781
9.70205E-6	10.37839	1.48471E-6	4.84768	7.56312E-6	2.79781
1.1245E-5	10.38621	1.84734E-6	4.84768	9.2362E-6	2.86269
1.30333E-5	10.39527	2.29854E-6	4.84768	1.12794E-5	2.86994
1.5106E-5	10.40577	2.85993E-6	4.84768	1.37746E-5	2.8788
1.75084E-5	10.41794	3.55844E-6	4.84768	1.68218E-5	2.88961
2.02928E-5	10.43205	4.42755E-6	4.84768	2.0543E-5	2.90282
2.352E-5	10.4484	5.50894E-6	4.84768	2.50875E-5	2.92504
2.72604E-5	10.46735	6.85444E-6	4.84768	3.06372E-5	2.95646
3.15957E-5	10.48932	8.52856E-6	4.84768	3.74147E-5	3.01933
3.66204E-5	10.50575	1.06116E-5	4.93515	4.56914E-5	3.0373
4.24442E-5	10.52193	1.32034E-5	4.94011	5.57991E-5	3.05926
4.91942E-5	10.54068	1.64281E-5	4.94629	6.81428E-5	3.10507
5.70177E-5	10.56242	2.04405E-5	4.95397	8.32171E-5	3.16773
6.60853E-5	10.58761	2.54329E-5	4.96352	1.01626E-4	3.23115
7.6595E-5	10.6168	3.16447E-5	5.10691	1.24107E-4	3.34715
8.87761E-5	11.73076	3.93736E-5	5.12528	1.51562E-4	3.39825
1.02894E-4	11.77634	4.89902E-5	5.14813	1.8509E-4	3.46798
1.19258E-4	11.82917	6.09555E-5	5.18791	2.26035E-4	3.65148
1.38224E-4	12.94384	7.58433E-5	5.42639	2.76038E-4	3.74425
1.60206E-4	13.01815	9.43672E-5	5.56467	3.37102E-4	3.91414
1.85684E-4	13.49495	1.17415E-4	5.69008	4.11674E-4	4.07011
2.15213E-4	14.12022	1.46093E-4	5.87046	5.02744E-4	4.26681
2.49439E-4	14.32365	1.81775E-4	6.0739	6.13959E-4	4.47592
2.89108E-4	14.72291	2.26171E-4	6.35316	7.49777E-4	4.69894
3.35085E-4	15.74794	2.81411E-4	6.56002	9.1564E-4	4.96513
3.88375E-4	16.52971	3.50143E-4	6.91911	0.00112	5.2393
4.50139E-4	17.68055	4.35662E-4	7.2365	0.00137	5.5482
5.21725E-4	18.13108	5.42068E-4	7.58071	0.00167	5.85971
6.04697E-4	19.88529	6.74463E-4	8.03956	0.00204	6.2288
7.00863E-4	20.41875	8.39194E-4	8.5349	0.00249	6.61428
8.12323E-4	21.70947	0.00104	8.96596	0.00304	7.00629
9.41508E-4	23.05261	0.0013	9.52804	0.00371	7.44896
0.00109	25.14498	0.00162	10.09063	0.00453	7.90841
0.00126	26.59168	0.00201	10.68638	0.00553	8.41495
0.00147	27.9365	0.0025	11.28908	0.00676	8.96928
0.0017	29.0923	0.00311	11.96956	0.00825	9.54803
0.00197	30.10168	0.00387	12.65696	0.01007	10.18459
0.00228	31.00419	0.00482	13.39872	0.0123	10.85224
0.00265	31.74068	0.006	14.15943	0.01503	11.57788
0.00307	32.28956	0.00746	14.96665	0.01835	12.30748
0.00355	32.73122	0.00929	15.80757	0.02241	12.98951
0.00412	32.99199	0.01155	16.66064	0.02737	13.56692
0.00477	33.14444	0.01438	17.49379	0.03342	13.99344
0.00553	33.2093	0.01789	18.26441	0.04081	14.24977
0.00641	33.17104	0.02225	18.88547	0.04984	14.37065
0.00743	33.085	0.02769	19.35788	0.06087	14.39967
0.00862	32.91912	0.03445	19.67623	0.07433	14.37853

Table 7.4: Tensile based yield stress – plastic strain data for PP with vertical print orientation.

-30 °C		0 °C		23 °C	
Plastic strain	Yield stress in MPa	Plastic strain	Yield stress in MPa	Plastic strain	Yield stress in MPa
0	9.16061	0	4.63539	0	2.7435
1.72966E-7	9.16061	3.56208E-6	4.63539	2.08073E-6	2.7435
2.16909E-7	9.16061	4.30562E-6	4.65192	2.57133E-6	2.74433
2.72016E-7	9.16061	5.20437E-6	4.6719	3.17759E-6	2.74535
3.41123E-7	9.16061	6.29072E-6	4.68902	3.9268E-6	2.74661
4.27787E-7	9.16061	7.60384E-6	4.69754	4.85265E-6	2.74818
5.36469E-7	9.16061	9.19105E-6	4.70783	5.9968E-6	2.75011
6.72761E-7	9.16061	1.11096E-5	4.72028	7.41072E-6	2.75249
8.4368E-7	9.16061	1.34286E-5	4.73505	9.15801E-6	2.75544
1.05802E-6	9.16061	1.62316E-5	4.75139	1.13173E-5	2.75909
1.32682E-6	9.16061	1.96198E-5	4.77115	1.39856E-5	2.76359
1.6639E-6	9.16061	2.37152E-5	4.79503	1.72832E-5	2.76942
2.08663E-6	9.16061	2.86654E-5	4.86149	2.13582E-5	2.78085
2.61674E-6	9.16061	3.4649E-5	4.90396	2.63939E-5	2.79498
3.28154E-6	9.67789	4.18816E-5	4.94596	3.26171E-5	2.81243
4.11524E-6	9.68068	5.06239E-5	4.9957	4.03075E-5	2.93673
5.16073E-6	9.68418	6.1191E-5	5.05025	4.98111E-5	2.94086
6.47185E-6	9.68857	7.39639E-5	5.10803	6.15555E-5	2.94597
8.11605E-6	9.69408	8.9403E-5	5.28725	7.6069E-5	2.95228
1.0178E-5	9.70098	1.08065E-4	5.40479	9.40044E-5	3.10192
1.27638E-5	9.70964	1.30622E-4	5.49527	1.16169E-4	3.1865
1.60065E-5	9.72049	1.57888E-4	5.66307	1.43559E-4	3.23885
2.0073E-5	9.7341	1.90845E-4	5.86957	1.77407E-4	3.34131
2.51726E-5	9.75118	2.30682E-4	6.0568	2.19236E-4	3.42642
3.15679E-5	9.77259	2.78834E-4	6.27503	2.70927E-4	3.57827
3.95879E-5	9.79943	3.37037E-4	6.49182	3.34805E-4	3.73815
4.96454E-5	10.70771	4.0739E-4	6.78025	4.13745E-4	3.92768
6.2258E-5	10.77854	4.92428E-4	7.08346	5.11298E-4	4.13669
7.8075E-5	10.90558	5.95216E-4	7.38827	6.31851E-4	4.28452
9.79104E-5	11.58809	7.1946E-4	7.72805	7.80827E-4	4.5663
1.22785E-4	11.74248	8.69639E-4	8.13038	9.6493E-4	4.8209
1.53979E-4	11.90672	0.00105	8.51466	0.00119	5.12281
1.93099E-4	13.65793	0.00127	8.98256	0.00147	5.43033
2.42156E-4	14.33554	0.00154	9.42527	0.00182	5.82372
3.03677E-4	15.51546	0.00186	9.89805	0.00225	6.12976
3.80828E-4	15.94311	0.00224	10.39471	0.00278	6.51526
4.7758E-4	17.89419	0.00271	10.89548	0.00344	6.93661
5.98912E-4	19.70353	0.00328	11.42247	0.00425	7.38762
7.51068E-4	21.51981	0.00396	11.95244	0.00525	7.8774
9.41881E-4	23.30615	0.00479	12.50051	0.00649	8.40334
0.00118	24.5732	0.00579	13.05796	0.00801	8.96386
0.00148	25.67445	0.007	13.65734	0.0099	9.53956
0.00186	26.53806	0.00846	14.26129	0.01224	10.14344
0.00233	27.18362	0.01022	14.88441	0.01513	10.73738
0.00292	27.75763	0.01236	15.48611	0.01869	11.28389
0.00366	28.07221	0.01494	16.04704	0.0231	11.70414
0.00459	28.24013	0.01806	16.57402	0.02855	12.02696
0.00576	28.24614	0.02183	17.0384	0.03528	12.21869
0.00723	28.11873	0.02638	17.39111	0.04359	12.36128
0.00906	27.90007	0.03189	17.66459	0.05387	12.43093
0.01136	27.64919	0.03855	17.8562	0.06657	12.45864